Deciphering the Late Cretaceous-Cenozoic structural evolution of the North Peruvian forearc system

N. Espurt, S. Brusset, P. Baby, P Henry, M. Vega, Y. Calderon, L. Ramirez, M. Saillard

Deciphering the Late Cretaceous-Cenozoic structural evolution of the North Peruvian forearc system

N. Espurt[1], S. Brusset[2], P. Baby[2], P. Henry[1], M. Vega[3], Y. Calderon[4], L. Ramirez[4] and M. Saillard[5]

[1]Aix-Marseille Univ, CNRS, IRD, Coll de France, CEREGE, Aix en Provence, France

[2]Géosciences Environnement Toulouse (GET), Université de Toulouse, CNRS UMR 5563 / UR 234 IRD / UPS Toulouse / CNES, 14 Avenue Edouard Belin, 31400 Toulouse, France

[3]Universidad Nacional de San Antonio Abad del Cusco, Cusco, Peru

[4]PERUPETRO S.A., Avenida Luis Aldana, 320 San Borja, Lima 41, Peru

[5]Université Côte d'Azur, IRD, CNRS, Observatoire de la Côte d'Azur, Géoazur, Valbonne, France

Corresponding author: Nicolas Espurt (espurt@cerege.fr)

Key Points:

- The North Peruvian forearc system structure is driven by buried imbricate thrust systems bounding thrust-top sedimentary depocenters
- The Late Cretaceous-Cenozoic accretion and uplift of the forearc system was punctuated by zones of crustal normal to strike-slip faulting
- The forearc system evolution was controlled by subduction dynamics, thick sediment accumulation, and bathymetric asperities

Abstract

The link between plate tectonics and the evolution of active margins is still an ongoing task to challenge since the acceptance of plate tectonic paradigm. This paper aims at deciphering the structural architecture and uplift history of the North Peruvian forearc system to better understand the evolution and the mechanics that govern the Late Cretaceous-Cenozoic building of this active margin. In this study, we report surface structural geology data, interpretation of seismic reflection profiles, apatite fission-track data, and the construction of two offshore-onshore crustal-scale balanced cross sections. The structure of the North Peruvian forearc system is dominated by an accretionary style with northwestward propagation of thrust-related structural highs involving continental/oceanic basement rocks, and off-scrapped sediments. The thrust systems bound thick thrust-top forearc depocenters mainly deformed by crustal normal to strike-slip faults and thin-skinned gravitational instabilities. The sequential restoration of the margin calibrated with apatite fission-track data suggests a correlation between uplift, shortening and plate convergence velocity during Late Cretaceous and Miocene. Pliocene-Quaternary shortening and uplift of the coastal zone is rather related to the subduction of asperities during convergence rate decrease. The development of crustal normal to strike-slip faulting and subsidence zones might be the consequence of slab flexure, local basal erosion along subduction fault, and/or oblique subduction associated with sediment loading control. We conclude that the evolution of the North Peruvian forearc system was controlled by subduction dynamics, strong sediment accumulation and recent ridge subduction, and it recorded the orogenic loading evolution of the Andes over the Cenozoic.

1 Introduction

Forearc systems develop on the subducting oceanic lithosphere ahead of the overriding orogenic wedge/magmatic arc [*Dickinson and Seely*, 1979; *Dickinson*, 1995]. From sea to land, these systems are classically composed of: a distal trench basin, an outer subduction wedge, including a frontal accretionary prism and a middle prism (structural high) overlapped by trench-slope basins, and an inner crustal wedge corresponding to the orogenic wedge/magmatic arc overlapped by a forearc depocenter [*Bailleul et al*., 2007; *Noda*, 2016]. Modern forearc systems are tectonically active and associated with faulting, vertical motions and volcanism, and they are the site of largest and most destructive earthquakes and tsunamis [*e.g., Bilek*, 2010; *Schurr et al.*, 2012; *Hall et al*., 2012; *Villegas-Lanza et al.*, 2016; *Saillard et al.*, 2017; *Benavente et al.*, 2017]. Although it is widely accepted that forearc deformation is the product of both compressional and extensional tectonics [*Noda*, 2016], the temporal and spatial variations as well as the origin of these tectonics mechanisms are still poorly understood. As well as, the deep large-scale structural architecture of these systems remains poorly defined [*e.g., Shiki and Misawa*, 1982*; Chanier et al*., 1999; *Barnes et al*., 2002; *Laursen et al*., 2002; *Melnick et al*., 2006; *López et al*., 2008; *Saura et al*., 2008; *Mukti et al*., 2012; *Moore et al*., 2015; *Mora-Bohórquez et al.*, 2017]. Several studies pointed out that the dynamics of the subduction (direction, velocity, flexure), subducting plate relief (roughness, seamount, ridge), degrees of sediment influx at the trench, plate contact conditions, overriding plate tectonics and magmatic arc history might exert a strong control on the structural style (accretion or erosion), and development of many forearc systems on Earth [*e.g., Royden*, 1993; *Le Pichon et al*., 1993; *Lallemand et al*., 1994; *Dickinson*, 1995; *Von Huene and Lallemand*, 1990; *Clift and Vannucchi*, 2004; *Fuller et al*., 2006; *Regalla et al*., 2013; *Takano et al*., 2013; *Carminati et al*., 2014; *Tsuji et al*., 2015; *Martinod et al*., 2016; *Noda*, 2016; *Collot et al*., 2017].

Forearc regions have been generally discarded by petroleum industry mostly because of their high structural and stratigraphic complexities, polyphase tectonic histories, active tectonics and their inferred low petroleum potential. The giant Talara petroleum province of the North Peruvian forearc system (~4°S) is one of the striking exceptions to this generally held idea [*Moberly et al*., 1982; *Carozzi and Palomino*, 1993; *Higley*, 2004; *Fildani et al*., 2005] (Figure 1). This frontier zone represents a challenge for future georesource explorations and strategies in forearc areas. Apart from stratigraphic and provenance data [*Fildani et al*., 2008; *Hessler and Fildani*, 2015; *Witt et al.*, 2017], the Cenozoic tectonic evolution of this forearc system has never been documented in terms of structural reconstruction of different episodes of its deformation.

The active Andean margin of Ecuador, Peru and northern Chile (1°N-33°S) is described as a type example of modern erosion margin [*e.g., Von Huene and Lallemand*, 1990; *Collot et al*., 2002; *Clift et al*., 2003; *Hoffmann-Rothe et al.*, 2006]. However, the results presented here show that the tectonic style of the northern Peruvian margin is mostly dominated by accretion of crustal and sedimentary rocks during the Cenozoic. Contrary to other forearc basins of the Peruvian Andes, the North Peruvian margin is characterized by a thick Cretaceous to Quaternary siliciclastic succession up to ~11 km-thick that extends onshore and offshore [*Gutscher et al*., 1999a; *Collot et al*., 2002; *Fernández et al*., 2005]. The modern margin receives large clastic sedimentary influx from the Guayas River in Ecuador, and Tumbes and Chira Rivers in Peru [*Salomons et al*., 2005]. Numerous and high quality 2D-3D onshore-offshore seismic reflection data indicate that the structure of the basin is complex with extensional tectonic regime and gravitational sliding at surface [*Shepherd and Moberly*, 1981; *Moberly et al*., 1982; *Deniaud et al*., 1999; *Witt et al*., 2006; *Witt and Bourgois*, 2010; *Bourgois*, 2013], probably controlled by strong sediment accumulation, together with offshore strike-slip systems, and prominent structural imbricates of continental and/or oceanic material [*Séranne*, 1987]. This study integrates a multi-disciplinary approach, including structural geology, interpretation of seismic reflection profiles, cross section balancing and apatite fission-track data in order to decipher the structure of the North Peruvian forearc system, and provide a complete subduction-scale evolutionary scenario during the Late Cretaceous and Cenozoic. We provide new insights into the comprehension and quantification of the tectonics and geodynamics processes of the subduction zone and associated forearc system.

2 Geological background

2.1 Tectonic context

The Nazca (Farallon)-South American plate convergence system is characterized by a rapid westward displacement of the continental South American plate above the oceanic Nazca (Farallon) plate since the Upper Cretaceous [*Frutos*, 1981; *Marrett and Strecker*, 2000]. In northern Peru, the subduction of the Nazca plate beneath the South American plate is N83°E trending, oblique to the N30-40°E trend of the Northern Andes [*Villegas-Lanza et al*., 2016]. The Nazca and South American plates move at an absolute rate of 22 mm/yr and 47 mm/yr, respectively [*Gripp and Gordon*, 2002]. *Somoza and Ghidella* [2012] showed that the westward motion of the South American plate may have been constant (between ~30 and ~40 mm/yr) during the last 40 Ma whereas the eastward motion of the Nazca (Farallon) plate has changed over this period. Plate reconstructions of *Somoza and Ghidella* [2012] suggest that the Late Cretaceous-Cenozoic convergence history between the Nazca and South American plate is characterized by an increase of the convergence rate between Paleocene to Late Oligocene (from 4 to 14 cm/yr) including two accelerations at ~56-43 Ma and ~32-24 Ma, followed by a global decrease between Miocene to present day. The Late Oligocene-

Early Miocene convergence peak coincides approximately with the breakup of the Farallon plate and creation of Cocos and Nazca plates [*Londsale*, 2005; *Somoza and Ghidella*, 2012]. In northern Peru and Ecuador the variations in the convergence rate are more or less correlated with deformational stages in the forearc zones [e.g., *Daly*, 1989; *Jaillard and Soler*, 1996; *Jaillard et al*., 1997] and pronounced arc magmatic productivity [*Schütte et al*., 2010]. The Ecuadorian margin suffers the collision of Cretaceous oceanic terranes during the Late Paleocene-Early Eocene [*Jaillard et al*., 1997]. There is no evidence for oceanic terranes along the northern Peruvian margin, except in the Paita area (Figure 1a), where oceanic boulders are found in the Early Eocene conglomerates of the Mogollon Formation [*Pecora et al*., 1999]. In addition, plate model reconstructions [e.g., *Sdrolias and Müller*, 2006] show that the age of the subducting oceanic lithosphere under the northern Peruvian margin varied through the Cenozoic from ~60-70 Ma (Paleocene) to ~20-30 Ma (present).

Nazca (Farallon)-South America plate convergence system has been associated with subduction of numerous topographic asperities during the Cenozoic times [*e.g. Gutscher et al*., 2002; *Espurt et al*., 2008]. For instance, in Ecuador, the subduction of the broad Carnegie ridge began ~8-15 Ma ago [*Daly*, 1989; *Gutscher et al*., 1999a; *Schütte et al*., 2010], ~3-5 Ma ago [*Michaud et al*., 2009; *Collot et al*., 2009], or ~1-2 Ma ago [*Lonsdale and Klitgord*, 1978] and is uplifting the Ecuadorian forearc zone [*Pedoja et al*., 2006]. In northern Peru, the enigmatic Inca Plateau subducted in the Middle Miocene [*Gutscher et al*., 1999b] or somewhat earlier [*Skinner and Clayton*, 2013] and would be responsible for slab flattening (northern edge of the Peruvian flat slab segment). Currently, N50–55°E trending aseismic ridges/scaps (Sarmiento, Alvarado and Grijalva) are being subducted obliquely beneath the northern Peruvian margin and southern Ecuadorian margin (Figure 1). These 1-2 km-high and 20-40 km-wide asperities migrate southward along the margin [*Lonsdale*, 2005].

The study area belongs in the Huancabamba deflection zone where the structural strike of the Andes shows a significant rotation (Figure 1a). North of the Huancabamba deflection, the North Peruvian forearc system is part of the NNE-trending Northern Andes, overprinting a Triassic-Jurassic rift well defined in Ecuador [*Spikings et al*., 2016]. The post-Oligocene rotations are ~25° clockwise north of the deflection, in the Lanconces basin [*Mitouard et al*., 1990] (Figure 1b). Recent large-scale analyses of GPS data in Peru and Ecuador [*Nocquet et al*., 2014; *Chlieh et al*., 2014; *Villegas-Lanza et al*., 2016] suggest that the North Peruvian forearc system currently belongs to the rigid forearc Inca Sliver that encompasses the southernmost Ecuador and Peru. This sliver moves at 4-5 mm/yr southeastwards (Figure 1a).

The North Peruvian forearc system extends 200-km-wide onshore and offshore between the Peru trench and the Western Cordillera volcanic arc (Figure 1a). It is a tectonically active system related to the post-Jurassic geodynamics of the Nazca (Farallon) and South American convergence plate system [*Jaillard et al*., 1990]. The North Peruvian forearc system displays a complex structural architecture with a southeastern onshore domain including basement highs, such as the Amotape High and subsurface Carpitas-Zorritos High, and a northwestern offshore domain characterized by a shallow-water (120 mbsl) flat-topped high so-called Banco Peru [*Fernández et al*., 2005; *Auguy et al*., 2017; Calvès et al., 2017], located ~50 km seaward from the coastline (Figure 1b). These NE-trending structural highs delimit four major depocenters of Cretaceous and Cenozoic siliciclatic strata (Lancones, Talara, Tumbes and Trench-Slope forearc depocenters) reaching locally more than 9 km in thickness (Figure 1b). These depocenters are deformed by numerous normal growth faults and gravitational instabilities, and strike-slip faults in the offshore Tumbes depocenter [*Séranne*, 1987; *Witt and Bourgois*, 2010]. The offshore Tumbes depocenter connects northward with the Guayaquil basin, which is described as a pull-apart basin [*Travis et al*., 1974; *Shepherd and Moberly*, 1981; *Deniaud et al*., 1999; *Witt and Bourgois*, 2010] (Figure 1a).

Exhumation history of the North Peruvian margin is poorly constrained by geochronological and thermochronological data. Some apatite and zircon fission-track, and apatite (U-Th)/He studies in the Ecuadorian and North Peruvian forearc zones suggest that the exhumation may have started in Late Cretaceous-Paleogene (65-45 Ma) and Eocene (45-39 Ma) [*Spikings et al*., 2005; *Wipf*, 2006; *Spikings et al*., 2010]. Stratigraphic and provenance data of *Fildani et al.* [2008] and *Hessler and Fildani* [2015] in the Talara depocenter suggest that the relief of the Amotape High was in place since the Early Eocene with transverse and longitudinal drainage systems.

2.2 Stratigraphy

The tectono-stratigraphy of the North Peruvian forearc system is summarized in Figure 2 and described hereafter.

2.2.1 Paleozoic-Triassic Amotape continental basement

Continental basement rocks (named the Amotape basement) form the large Paleozoic outcrops of the Amotape High and La Brea (Figures 1b and 3). They are composed of highly deformed Mississippian, Devonian and older (Ordovician?) metasediments, schists and gneisses (Figure 4a) [e.g., *Witt et al*., 2017]. Metamorphic rocks are locally covered by Pennsylvanian turbidites of the Chaleco de Paño Formation and Permian limestones (Figure 4b). Paleozoic rocks are intruded by Triassic granite with ages ranging from 230 Ma to 220 Ma [*Sánchez et al*., 2006; *Witt et al*., 2017]. Subsurface and field data provide evidence for metamorphic and granitic basement below the Talara depocenter and the Carpitas-Zorritos High [*Fernández et al*., 2005] (Figures 1b and 3).

The Amotape basement corresponds to the southward prolongation of the Ecuadorian Eastern Cordillera (so-called Cordillera Real), and it connects southward with the Coastal Cordillera of Peru (Paita and Illescas Highs; Figure 1a). To the south, the Amotape basement connects to the outer shelf high of Trujillo and Salaverry basins [*Romero et al*., 2013; *Witt et al*., 2017]. The Amotape basement is interpreted to form a continental block accreted onto the South American margin in the Early Permian [*Ramos*, 2009] or Early Cretaceous [*Mourier et al*., 1988; *Winter et al*., 2010]. It is also interpreted as a rifted fragment of South America (western Pangaea) within a back-arc setting in the Triassic [*Riel et al*., 2014; *Spikings et al.*, 2015*; Witt et al.*, 2017].

2.2.2 Cretaceous series of the Lancones depocenter

The Lancones depocenter exhibits a ~4 km-thick Albian to Campanian sedimentary succession deposited in forearc basin settings associated with small intrusive bodies [*Jaillard et al*., 1999; *Valencia and Uyen*, 2002; *Winter et al*., 2010] (Figures 2 and 3). The series are connected eastward with the Celica continental arc [*Lebras et al*., 1987; *Jaillard et al*., 1999], and pinchout northwestward onto the Amotape High.

The basal Albian series consist of massive conglomerates of the Gigantal Formation and conglomerate channels, grainstones and shales of the Pananga Formation. These series are mainly exposed along the southeastern flank of the Amotape High. The conglomerates contain clasts exclusively sourced from the Amotape basement and the Celica arc. The upper Albian Muerto Formation consists of oil-bearing limestones and black shales. Southeastward, the Muerto Formation shows volcanoclastics and breccias intercalations corresponding to the Lancones Formation. The overlying Cenomanian and Turonian rocks consists of turbidites, shallow marine volcanoclastic sandstones and grey to black shales of the Huasimal, Jahuay Negra and Encuentros Formations. This package is unconformably overlain by Campanian

coarse-grained sandstones of the Tablones Formation. The Cretaceous succession is topped by shallow marine black shales and sandstones of the Pazul/Redondo Formation.

South of the Huaypirá fault, Cretaceous series are unconformably overlain by Eocene strata of Chocan, Verdun and Chira Formations, and Late Eocene or Oligocene Mirador Formation particularly developed in the Sechura basin [*Valencia and Uyen*, 2002] (Figures 1 and 2). No evidence of Cretaceous strata has been described in the northern part of the Talara depocenter. However, Cretaceous series are known in subsurface from exploration wells south of Mancora city [*Fernández et al*., 2005] (Figure 1b).

2.2.3 Cenozoic series of the Talara and Tumbes depocenters

Detrital U-Pb zircon ages suggest that Cenozoic sediments of the onshore Talara depocenter are mainly sourced from the Paleozoic basement of the Western Cordillera of Peru and Amotape High [*Hessler and Fildani*, 2015; *Witt et al*., 2017] (Figure 1). Paleocene-Eocene series correspond to fluvial to deep-marine strata, reaching up to 3.5 km-thick in the northern Talara depocenter, and more than 9 km-thick to the south [*Séranne*, 1987; *Higley*, 2004; *Fernández et al*., 2005]. Paleocene series are only known in exploration wells south of the study area. In the study area, the Amotape basement is unconformably covered by Early Eocene alluvial–fluvial series simplified as Mogollon-Salinas Formation (Figures 4a,b) [*Higley*, 2004; *Fernández et al*., 2005; *Fildani et al*., 2008]. It is composed of massive conglomerates, grainstones including wood and vertebrate remains, and upper grey to red shales [*Fildani et al*., 2008; *Antoine et al*., 2015]. Locally, the basal part of the Mogollon Formation is formed by quartz conglomerate and grey shales of the San Cristobal Formation. The Middle Eocene series are simplified as basal Talara Formation and upper Verdun Formation deposited in deepwater environment [see details in *Fildani et al*., 2008]. The Talara Formation consists of dark brown shales and grainstones intercalated with turbiditic channels, breccias, mudstones and tuff layers. The Verdun Formation is interpreted as a turbiditic system of thick conglomerate and sandstone intervals interbedded with thin-bedded sandstone and mudstone. The Late Eocene Chira Formation consists of marine mudstone deposited in a shallow marine environment. Subsurface data suggest that thinner Paleocene(?)-Eocene series are also present at the base of the onshore Tumbes depocenter [*Fernández et al*., 2005].

Latest Eocene(?)-Oligocene sequences are characterized in the field and subsurface by the appearance of coarse-grained fluviodeltaic sequences above a subaerial erosional surface [*Fernández et al*., 2005]. The sequences consist of the massive Gilbert delta sytem of the Latest Eocene or Oligocene Mirador Formation (Figure 4c) followed by prograding fluviodeltaic sequences of the Oligocene Mancora Formation intercalated with white to pink akosic and quartzitic sandstone, tuff, and conglomerate sequences of the Plateritos Formation (Figure 4d) [*Pozo*, 2002; *Vega*, 2009]. Although Oligocene strata are cut by normal faults, subtle (compressional?) growth strata geometries are locally recognized in the Plateritos and Mancora sequences along the Bocapan River (Figure 4e). The Late Oligocene-Early Miocene Heath formation consists of organic-rich dark brown to light grey lutites, siltstones and some limestones and marls deposited in deepwater environment (more than 1 km depth). The Early Miocene Zorritos Formation consists of aggradational to prograding marine-terrigenous and subordinated varicolored shales sequences deposited within a flood to marine influenced coastal plain setting. The Middle Miocene begins with a regional unconformity produced by the erosion of the former platform and generation of valleys filled and covered by the marginal marine and deltaic Middle Miocene Cardalitos and Late Miocene Tumbes Formations and Latest Miocene-Pliocene Mal Pelo Formation [*Fernández et al*., 2005]. The uppermost Late Pliocene-Pleistocene La Cruz Formation and more recent sequences

unconformably overlay the underlying Mal Pelo sequences. Deposits consist of regional grey-green claystone, some sandy interbeds with common shell fragments and dolomitized limestones.

Onshore, Pliocene-Pleistocene deposits correspond to marine terraces (including so-called Tablazos) along the coastline of the Talara depocenter [*Bosworth*, 1922; *DeVries*, 1988; *Macharé and Ortlieb*, 1994; *Pedoja et al*., 2006; *Darrioulat*, 2011] and alluvial terraces including well-rounded blocks of granite close to the Amotape High.

3 Surface and subsurface structural architecture

The northern Peruvian margin is characterized by a coastal desert [*Garreaud*, 2009] providing an extremely good cross-sectional exposure of sedimentary units and geological structures (Figures 4 and 5). To constrain the structural architecture of the North Peruvian forearc system, we used new field structural data, ten seismic reflection profiles (RIB93-01, VMX09-01, VMX09-23, AIP92-15, PC99-11, BPZ23-16, PXII99-02, and L1, L2 and L3 extracted from 3D seismic cubes), and wells provided by PERUPETRO S.A. (see Figures 1b and 3 for location). New onshore geological mapping (Figure 3) was performed using preexisting 1:100.000 INGEMMET (Instituto Nacional Geológico, Minero y Metalúrgico del Perú) geological maps, field data and satellite images. Seismic profiles were depth-converted using the Move software and seismic velocities of sedimentary intervals (e.g., *Etrys et al*., 2002; *Totake et al*., 2017) from exploration wells (supporting information Table S1).

The morphostructure of the North Peruvian forearc system includes seven structural units according to the geological map, field and subsurface data, and the cross sections which are presented in this study. From arc to sea, these units are: the Lancones forearc depocenters, the Amotape High, the Talara forearc depocenter, the Carpitas-Zorritos High, the Tumbes forearc depocenter, the Banco Peru and frontal prism, and the subducting Nazca plate (Figure 1b). In the following, the structural architecture and kinematics of the North Peruvian forearc system is presented along two N137°E- to N93°E-trending cross sections: a northeastern transect A and a southwestern transect B (Figures 1b, 3 and 5).

3.1 The Lancones forearc depocenter

The southeastern edge of the North Peruvian forearc system is formed by the Lancones forearc depocenter involving Cretaceous strata. Cretaceous strata are deformed by NW-verging thrust-related anticlines (e.g., Totoras, Gallinazos, Jabonillos and Jahuaycito anticline) locally reactivating the onlap surface of the Cretaceous strata against the Amotapes basement (Figures 5 and 6). Field data and interpretation of seismic line PXII99-02 indicate that thrust faults may correspond to reactivated basement normal faults inherited from an Early Cretaceous extensional period (Figures 7a and 8) as suggested by *Jaillard et al*. [1999] and *Winter et al.* [2010]. Inversion and thrusting was recorded by Late Cretaceous growth strata in the Encuentros Formation [*Jaillard et al*., 1999; *Andamayo*, 2008].

The Lancones depocenter shows NE- to E-trending Cenozoic normal faults that cut the pre-structured folds and thrusts (Figures 1b, 3 and 5). A major N35°E-trending 40-50°SE-dipping fault corresponds to the Cuzco-Angolo normal fault which separates the Amotape High from the Lancones depocenter. South of the study area, E-trending S-dipping La Encanada and Huaypirá normal fault zones cut obliquely across compressional structures and Amotape High [*Valencia and Uyen*, 2002; *Andamayo*, 2008].

3.2 The Amotape High

The Amotape High represents a prominent range located between the Lancones and Talara depocenters, reaching elevations of ~1500 masl and exposing Paleozoic rocks and Triassic intrusions (Figures 1b, 3 and 5). It forms a ~140-km-long with a maximum width of ~20 km bulge onlapped by tilted Cretaceous and Cenozoic strata. The backlimb of this anticline is formed by 10°SE-dipping Early Cretaceous strata while the forelimb is formed by 12°NW-dipping Early Eocene (Figures 4a and 5). Paleozoic strata of the forelimb are strongly deformed by a NNE-trending SE-dipping fault zone (Figure 3). South of cross section A, metamorphic and igneous rocks are thrust onto Paleozoic metasediments. Northward, the mapping suggests that the thrust zone is unconformably overlain by Early Eocene strata (Figure 3). This thrust fault may explain the high structural relief of the Amotape High in comparison to the lower topography (~250 masl) of the Talara depocenter (Figure 5).

3.3 The Talara forearc depocenter

The Talara forearc depocenter develops between the Amotape and subsurface Carpitas-Zorritos High (Figures 3 and 5). Its structure consists of a ~5-10°W-dipping homocline of Eocene to Miocene strata bounded northwestward by a major NE-trending SE-dipping listric normal faults system, the Carpitas-Trigal fault system, associated with antithetic normal faults (e.g., Cabeza de Vaca fault; Figures 5 and 9) [*Séranne*, 1987]. Surface data indicate that Early-Middle Eocene strata are in unconformable or in normal fault contact with the Amotape basement rocks at the southeastern edge of the Talara depocenter (Figures 3, 4a,b and 5).

The interpretation of seismic profile BPZ23-16 shows the overall unconformity of the Early Eocene series on the Amotape basement (Figure 10). No Cretaceous-Paleocene strata in this part of the Talara depocenter are found. Field and subsurface data show evidence for rapid change in thickness in Eocene sediments associated with growth normal faulting. No major thrusts emerge into the Talara depocenter [*Quispe Alcalá*, 2010]. However, we found numerous kinematic indicators for thrusting occurring before and after normal faulting in the Early-Middle Eocene series (Figures 7b,c).

At depth, the interpretation of the seismic profile BPZ23-16 suggests that basement normal faults are associated with low-angle SE-dipping décollements (Figure 10). We interpret these décollements as NW-verging thrust slices that extend below the Amotape High. This suggests that the structure and uplift of the Amotape High and inner Talara depocenter could be controlled by basement thrust imbrications at depth. Erosional surface and suspected growth strata geometry (see 2.2.3) observed in western flank of the Amotape High may provide an Early Eocene-Oligocene record for basement shortening.

3.4 The Carpitas-Zorritos High

The coastal Carpitas-Zorritos High separates the Talara and Tumbes forearc depocenters (Figure 1b). This structural high constitutes a major petroleum play where numerous exploration wells reached metamorphic/granitic rocks of the Amotape basement (Figures 3 and 5). Subsurface data indicate that this structural feature forms a relay system of two basement culminations at shallow-depth level beneath relatively thinner Eocene-Miocene sedimentary cover (~500 m) in comparison to the forearc depocenters [*Fernández et al.*, 2005]. The southeastern Carpitas High is separated from the northwestern Zorritos High by the Tronco Mocho SE-dipping normal fault system (Figure 5; section A). Landward, the Carpitas High is bounded by the Carpitas-Trigal fault system. Along section A, the northwestern flank of the Carpitas High shows spectacular detachments, roll-overs and raft structures in the Heath Formation [*Vega*, 2009] (Figure 11). These structures are interpreted as gravitational instabilities on the seaward-dipping paleo-slope of the Carpitas High.

Whereas the Carpitas High basement is unconformably overlain by Early Eocene strata of the Mogollon-Salinas Formation, the interpretation of seismic profile L1 (Figure 12) and well data show that the Zorritos High basement (granite) is unconformably overlain by Oligocene fluvial-deltaic sequences of the Plateritos and Mancora Formations. Subsurface data also suggest that the Tronco Mocho normal faults are connected with the Amotape basement. This fault system was probably active during the sedimentation of the Late Oligocene-Early Miocene Heath Formation and somewhat sealed by the Early Miocene Zorritos Formation (Figure 12). At depth, the interpretation of the seismic profile L1 also shows evidence for small compressional reactivation of the Tronco Mocho fault system. Here, we suspect that the footwalls of the normal faults are deformed by small NW-verging thrusts propagating with short-cut trajectories and intercutaneous prism (Figure 12). Numerous Plio-Pleistocene perched marine terrace sequences (Tablazos) along the coastal area at more than 300 masl indicate recent uplift of the Carpitas-Zorritos High [*DeVries*, 1988; *Séranne*, 1987; *Pedoja et al*., 2006; *Darrioulat*, 2011].

3.5 The Tumbes Forearc depocenter

The offshore Tumbes depocenter develops ~50 km ahead of the coastline between the Carpitas-Zorritos High and Banco Peru (Figure 1b). The synthetic seismic profiles of Figures 13 and 14 show that this depocenter depicts two stacked progradational sedimentary wedge systems of Eocene to Holocene series up to 11 km-thick along section B. The lower wedge consists of a seaward prograding wedge of Eocene-Early Oligocene series. In the western side of the Carpitas and Zorritos highs, the subsurface data show the pinchout of the inferred Early Eocene series onto a steep dip basement paleo-slope. Eocene series depict deep thrust-related anticline structures unconformably overlain by Early Oligocene series of the Mancora Formation (at the distance of ~60 km in Figure 13 and ~37 km in Figure 14). The upper wedge is formed by Late Oligocene to Holocene series deformed by numerous Miocene to present syn-depositional growth faults and rollovers. The upper wedge is gravitationally detached seaward from the underlying wedge above Late Oligocene-Early Miocene ductile shales of the Heath Formation as regionally observed in the field (Figure 11). The décollement has a dip of about 12°. In the seaward side of the basin, the sliding of the upper wedge is linked to compressional structures and mud diapirism related to the Heath Formation [*Fernández et al*., 2005; *Vega*, 2009]. More seaward, the series of the Tumbes depocenter pinch out onto the Banco Peru and are cut by the NNE-trending Banco Peru fault zone.

The Tumbes depocenter also shows NE-trending extension including NE- and SW-dipping listric normal faults [*Fernández et al*., 2005; *Auguy et al*., 2017] (Figure 1b). Strike-slip behavior may have also occurred along the Banco Peru fault zone. This geodynamic change is interpreted as the Neogene(?) to present pull-apart basin evolution of the Tumbes depocenter as a result of the northern escape of the North Andean block [*Witt and Bourgois*, 2010].

3.6 The Banco Peru and frontal structures

The offshore structural architecture is dominated by the broad structural high of the Banco Peru located between the Tumbes depocenter and the trench axis (Figure 1b). Along-strike, this structure extends from the onshore Talara depocenter to the Gulf of Guayaquil [*e.g.*, *Collot et al*., 2002; *Auguy et al*., 2017; *Calvès et al*., 2017] (Figure 1). The structural interpretation of seismic profiles VMX09-23 and RIB93-01 of section B (Figure 13) suggests that this major structure was generated by imbrication of three or more thrust sheets made of off-scrapped sediments (distal equivalents of the Eocene, Oligocene, and Miocene strata observed onshore) including oceanic mafic bodies (intrusives and volcanic) [*Shepherd and*

Moberly, 1981; *Fernández et al*., 2005]. It is covered by Oligocene to Plio-Pleistocene series strongly affected by normal faulting and gravitational sliding. The flat-topped geometry of the Banco Peru could be interpreted as a wave-cut platform [*Calvès et al*., 2017].

The landward side of the Banco Peru imbricate is characterized by SE-dipping normal to strike-slip faults of the Banco Peru fault zone. The faults branch onto a major ~20-25° SE-dipping fault (Figures 13 and 14). The interpretation of the seismic profiles suggests that the fault connects at depth onto the subduction plane rather than in the shallower ductile shales of the Heath Formation. This structural configuration has been previously proposed for strike-slip forearc model [*Noda and Miyakawa*, 2017] and described in the Ecuador forearc [*Collot et al*., 2004], Cascadia forearc [*McNeill et al*., 2000] and Naikai forearc [*Tsuji et al*., 2015], and also suggested in the Central Peruvian forearc [*Azalgara*, 1993; *Romero et al*., 2013]. The seaward side of the imbricate, the Trench-Slope depocenter, is characterized by seaward gravitational instabilities and sediment mass wasting. Subsurface data indicate the top of the oceanic plate and the basal décollement of the Banco Peru imbricate at about 8 kmbsl (Figure 13). Subsurface data also indicate that a large volume of sediment (~3 km-thick) is underplated beneath the Banco Peru imbricate. Near the trench, tectonic slices are maybe related to an active frontal prism of small size. These structural observations are similar to the ones described more southward in the Paita region [*Bourgois et al*., 1989] and along the southern Ecuadorian margin of the Guayaquil basin [*Collot et al*., 2002; *Calahorrano*, 2005; *Collot et al*., 2011] (Figure 1a).

3.7 The subducting oceanic Nazca plate

The good seismic resolution at depth of seismic lines VMX09-23 and RIB93-01 of section B (Figure 13) shows the geometry of subducting oceanic Nazca plate beneath the forearc prism. The subducting plate dips approximately 6° southeastwards from the Trench-Slope depocenter to the Tumbes depocenter. Along-strike bathymetric data of the Nazca plate were used to approximately evaluate the size and the position of the subducting ridges beneath the forearc prism [*Lonsdale*, 2005]. The Alvarado 1 and 2, and Sarmiento ridges are 1-2 km-high and 20-40 km-wide asperities smoothed by oceanic sediments. We propose that these rides extend beneath the Trench-Slope depocenter, Banco Peru and Talara depocenter, respectively (Figures 1b, 13 and 14). The subduction of the Sarmiento ridge might be associated with a Plio-Pleistocene coastal uplift [*Séranne*, 1987; *Pedoja et al*., 2006].

4 Timing of deformation as revealed by apatite fission-track dating

4.1 Methodology and sampling

Apatite fission-track thermochronology allows to constrain the vertical motions of the compressional basins through time and the pre-deformational basin architecture in order to provide a reliable estimation of the eroded relative stratigraphic thicknesses [*e.g., Espurt et al*., 2011; *Parra et al*., 2012; *Sánchez et al*., 2012; *Gautheron et al*., 2013]. Apatite fission-track thermochronology uses the partial stability of defects produced by the fission of ^{238}U, controlled by temperature [*Green et al*., 1989]. Apatite fission-tracks record the cooling of rocks below ~110°C during their exhumation [*e.g., Gallagher et al*., 1998].

Analyses were performed on nine rock samples from the Talara and Lancones depocenters, and Amotape High (eight Cretaceous-Eocene sedimentary rocks and one Triassic igneous rock) (see locations in Figure 15). Samples were analyzed using the laser ablation–inductively coupled plasma–mass spectrometry method at Apatite to Zircon, Inc., laboratory (see details of the method in *Hasebe et al*. [2004] and *Chew and Donelick* [2012]). Because samples are mainly sedimentary rocks with multicompositional apatites (mean maximum

diameters of fission-track etch figures parallel to the c axis, Dpar), we used central ages [*Galbraith and Laslett*, 1993]. To determine the last cooling event, we statistically decomposed sample grain-age distributions into component ages (supporting information Figure S1) using the RadialPlotter software [*Vermeesch*, 2009]. In addition, inverse thermal simulations were conducted using apatite fission-track ages, track lengths and kinetic parameters in the HeFTy software, and geological constraints [*Ketcham*, 2005; see *Parra et al*., 2012 for more details] (Figure 16). Complete results are provided in Table 1. Age errors are reported at 1σ.

4.2 Results

Apatite fission-track central ages range from 15.8 ± 0.6 to 52.5 ± 3.1 Ma, mean track lengths from 12.2 ± 0.1 to 13 ± 0.1 μm, and mean Dpar from 1.9 to 2.4 μm (Table 1). Age statistically decompositions (Figure S1) indicate that samples of the Talara depocenter (samples 1, 2, 3, 4, 5 and 9) have three components in the grain-age distribution: the age of the old component is ~118 Ma, the ages of the middle component range from 63.1 to 50.5 Ma, and the ages of the young component range from 38.8 to 28.8 Ma. Samples of the Amotape High and Lancones depocenter (samples 6, 7 and 8) show younger age component ranging between 22.7 to 14.8 Ma. By comparing the central/young apatite fission-track ages with the respective stratigraphic ages of the analyzed samples, we show that samples of the Talara depocenter have fission-track ages older, close to or younger than their stratigraphic ages (~52-38 Ma). Samples from the Amotape High and Lancones depocenter have younger fission-track ages than their stratigraphic ages (~230-52 Ma).

Additionally, our apatite fission-track ages are younger than the ones (including apatite and zircon fission-track, and apatite (U-Th)/He ages) obtained along-strike in the Ecuadorian segment of the Amotape High and to the south in the Paita High [*Spiking et al*., 2005; *Wipf*, 2006] (Figure 1a). These lateral units may have recorded older cooling onset between ~65 and 45 Ma or experienced a smaller burial (partial reset ages?) under Cenozoic series.

The dispersion in apatite fission-track ages requires thermal modeling to better constrain cooling and onset of exhumation. Samples of the Amotape High and Lancones depocenter (samples 6, 7 and 8) and one sample of the Talara depocenter (sample 2) were modeled using geological constraints, apatite fission-track results (ages, track lengths, Dpar values), and present surface temperature of 20 ± 5°C (Figure 16). For each sample, the thermal simulations suggest a Middle-Late Eocene reheating/burial after Late Cretaceous-Early Eocene deposition, followed by a Late Eocene-Oligocene (36–27 Ma) cooling/exhumation. The thermal simulation of sample 6 (Triassic Amotape granite) indicates an initial Late Cretaceous-Early Eocene (~80-50 Ma) cooling. This initial event might be recorded by the major unconformity of Early Eocene strata of the Mogollon-Salinas Formation on basement in the northwestern side of the Amotape High (Figures 4a,b and 5). The Late Eocene-Oligocene cooling event is attested by major erosion and strong depositional environment changes from marine to terrestrial conditions with sedimentation of the Mirador, Plateritos and Mancora sequences in the Talara and Tumbes depocenters (Figures 4c-e). Finally, we believe that youngest fission-track ages (22.7-14.8 Ma) have recorded the cooling of the samples through the ~110 °C isotherm (Figure 16). This Neogene cooling might be recorded by the erosional surface occurring at the base of the Middle Miocene Cardalitos sequences in the offshore Tumbes depocenter (Figures 2, 13 and 14) [*Fernández et al*., 2005].

5 Crustal-scale geometry and evolution of the North Peruvian forearc system

490 5.1 Crustal-scale cross sections

491 To evaluate and discuss the control of the surface and deep processes on the structural
492 building of the North Peruvian forearc system throughout the Late Cretaceous-Cenozoic
493 period, field, subsurface, and present-day seismicity events data (M_w>5) from the "Instituto
494 Geofísico del Perú" catalog 2005-2013 (http://www.igp.gob.pe) were used to construct and
495 interpret two ~200 km-long crustal-scale balanced cross sections from the Peru trench to the
496 volcanic arc (Figure 17). The frontal structure of cross section A has not been represented
497 because subsurface data are not available in this part of the margin. The section orientations
498 are parallel to the present-day direction of tectonic transport [*Nocquet et al*., 2014; *Chlieh et*
499 *al*., 2014; *Villegas-Lanza et al*., 2016] and perpendicular to the trend of the structures (Figures
500 1b and 3). The cross sections have been constructed using the Move structural modeling
501 software on the basis of thrust/extensional tectonic concepts [*Dahlstrom*, 1969; *Boyer and*
502 *Elliott*, 1982; *Suppe*, 1983; *Suppe and Medwedeff*, 1990; *McClay*, 1990; *Shaw et al*., 2005].
503 The reconstruction of the subducting plate geometry supported by deep seismicity events
504 shows a landward increase in the dip of the subduction thrust fault. This reconstruction
505 provides constrain for the present geometry and crustal area of the overriding upper plate.

506 Crustal-scale cross sections of Figure 17 suggest that the structure of the northern
507 Peruvian margin was dominated by an accretionary prism over the Nazca subducting plate.
508 The deep compressional features have been mostly hidden by thick Cenozoic sedimentary pile
509 and gravitational sliding, and synchronous or later extensional and strike-slip faulting
510 [*Séranne*, 1987; *Witt and Bourgois*, 2010]. North of the Talara city (Figure 1b), field cross
511 sections and well data suggested extensional tectonic and gravitational slidings interfering
512 with SE-verging thrusts [*Séranne*, 1987; *Quispe Alcalá*, 2010]. Our geometrical interpretation
513 based on seismic reflection profiles is, however, more consistent with NW-verging thrust
514 systems and seaward thrust propagation in the study area. Cross section construction suggests
515 that the structural culmination of the inner Amotape High might result in the imbrication of at
516 least three northwest-verging basement thrust sheets. The Lancones depocenter was
517 transported northwestward and uplifted by the Amotape imbricate. Subsurface data and cross
518 section balancing suggest that the Carpitas High may be also interpreted as the imbrication of
519 three northwest-verging thrust sheets involving the basement rocks and inferred off-scrapped
520 sediments (see below). As pointed out in section 3.6, the offshore domains developed by
521 accretion of off-scrapped sediment (including oceanic mafic bodies) constituting the Banco
522 Peru imbricate and the frontal active prism. The present-day seismicity events throughout the
523 study area might suggest active basement faulting beneath the onshore domain (Figure 17).

524 The atypical accretionary style of the North Peruvian forearc system is similar to the
525 ones described in Colombia and southern Chile forearc zones [e.g., *Laursen et al*., 2002;
526 *Melnick et al*., 2006; *Lopéz et al*., 2008; *Encinas et al*., 2012] and might result from major
527 trench sediment infill in the study area [*Collot et al*., 2002]. Strike-slip component interfering
528 with the dominant thrusting style can be associated with oblique subduction of the Nazca
529 plate beneath the Northern Andes [*Villegas-Lanza et al*., 2016; *Alvarado et al*., 2016; *Noda*
530 *and Miyakawa*, 2017].

531 5.2 Sequential restoration

532 Offshore forearc systems are classically composed of a distal trench basin, an outer
533 subduction wedge (frontal accretionary prism and structural high) overlapped by trench-slope
534 sediments, and an inner crustal wedge corresponding to the orogenic wedge/magmatic arc
535 overlapped by forearc sediments [see *Noda*, 2016 and references therein]. If this definition
536 matches with the structural architecture of the onshore Tumbes depocenter, we show that at
537 the scale of the margin, the structure of the North Peruvian forearc system results in the

accretion of successive forearc systems (Figure 17). To understand the temporal and spatial variations and the origin of the tectonics mechanisms that controlled the growth of the prism through the Late Cretaceous to Cenozoic, the regional cross section B across the North Peruvian forearc system was restored at five pre-deformational stages, which are illustrated in Figure 18. The cross section has been sequentially restored using the Move fault parallel flow and flexural slip algorithms according to the aforementioned data and apatite fission-track results (i.e., paleoburial and exhumation history). Bed area and length are conserved during consecutive deformation states. Because the prism shows major lateral and vertical variations in lithology and thickness of the sedimentary series the estimation of decompaction is difficult. Nevertheless, cross section restoration without sediment decompaction shows correct structural interpretation in such complex configuration [*e.g., Nunns,* 1991; *Zhou et al*., 2006]. In addition, we assume that the strike-slip motion along the Banco Peru fault zone is small [*Witt and Bourgois,* 2005] and would not significantly affect the structural geometry but might affect the shortening or extension amounts [e.g., *Wallace,* 2008]. Although the onshore area was affected by post-Oligocene rotation [*Mitouard et al*., 1999] no clear field evidence of strike-slip faulting over the Talara-Lancones area, is found [*Laj et al*., 1989]. Major strike-slip faulting is described in the arc and more to the north [e.g., *Witt et al*., 2006; *Riel et al*., 2014; *Alvarado et al*., 2016]. Finally, the sequential restoration respects paleo-bathymetries of the sedimentary units [*Fernández et al*., 2005; *Vega,* 2009; *Fildani et al*., 2008] and paleo-sea levels [*Haq et al*., 1987].

Hereafter, we describe the successive stages of deformation.

5.2.1 Late Cretaceous-Early Eocene stage (Figure 18a).

At this stage, the margin has been previously deformed during the Late Coniacian-Early Campanian interval and probably until the Eocene as response to initial construction of the Andes [*Jaillard et al*., 1999; *Hessler and Fildani,* 2015]. The Cretaceous series of the Lancones depocenter exhibit a wedge-shaped geometry thinning northwestward onto the Amotape basement. This wedge was deformed by NW-verging thin- and thick-skinned thrusts. The Amotape and Carpitas Highs can be interpreted as an 80 km-wide thrust sheet made of continental basement including second order thrusts and normal faults. The Amotape-Carpitas thrust system and the Lancones depocenter were uplifted and exposed above the sea level in the Early Eocene.

The reconstruction suggests that the Lancones depocenter had been passively transported northwestward as a thrust-top basin on the hanging-wall of the Amotape thrust system during Late Cretaceous and Early Eocene. This result is consistent with thermochronological studies suggesting that the Paita High and western Cordillera (lateral prolongation of the Amotape High) may have experienced a large range of cooling onset between ~65 and 45 Ma [e.g., *Wipf,* 2006]. Our reconstruction is also consistent with several studies which show evidence for major shortening during Late Cretaceous-Early Eocene in northern Peru [*e.g., Noble et al*., 1990; *Naeser et al*., 1991; *Jaillard and Soler,* 1996]. According to our thermochronological and geological data, the crustal stacking and uplift in the Amotape-Carpitas thrusts system has been sealed by Early Eocene strata. To the west, the Carpitas High is subject to extension associated with landward dipping normal faults (reactivation of inherited thrust faults?). Seaward, distal and thin Early Eocene series were deposited along the seaward dipping trench-slope basin and in the trench axis. The restored cross-section and crustal balancing suggest the underplating of a 5 km-high, 120 km-wide tectonic slice under the Amotape-Carpitas continental thrust sheet, responsible for the uplift of the Amotape-Carpitas thrust system and Lancones depocenter. The subduction of this inferred deep tectonic slice might be interpreted as the southern prolongation of broad Cretaceous

586 oceanic terranes accreted to Colombia and Ecuador margins during Late Cretaceous-Eocene
587 period [*Lebras et al*., 1987; *Jaillard et al*., 1995, 1997; *Borrero et al*., 2012].

588 5.2.2 Middle-Late Eocene stage (Figure 18b).

589 The restoration suggests that Middle-Late Eocene transgressive marine deposits of the
590 Talara, Verdun and Chira Formations are associated with major subsidence on the order of 4-
591 5 km located more than 150 km away from the trench. The restoration argues in favor of a
592 geodynamic model where reactivation of existing basement thrusts as normal faults and newly
593 formed normal faults mainly occur southeast of the Carpitas High. The reconstruction of a
594 thick Middle-Late Eocene sedimentary wedge is consistent with apatite fission-track reset
595 ages and paleo-burial data in the inner Talara-Amotape-Lancones zone (see Figure 19 and
596 section 6.1. for discussion). The restoration confirms that the Lancones and Talara
597 depocenters were connected in agreement with the stratigraphic correlations in Late Eocene
598 series infilling these depocenters [*Valencia and Uyen*, 2002]. Northwestward, the basement
599 culmination of the Carpitas High is overlain by a thin (~0.5 km) Eocene succession. We
600 model that the Carpitas High formed a seaward-verging thrust sheet overthrusting distal
601 Eocene sediments previously deposited above the oceanic plate (trench-slope depocenter?).
602 More seaward, we infer that a frontal wedge was maybe active. The restoration suggests that
603 the deep tectonic slice of Cretaceous oceanic terranes was subducted to a mean depth of ~25
604 km without major internal shortening. Comparison of Early and Late Eocene states suggests
605 that ~24 km of slip has been accommodated by the Carpitas thrust sheet. The crustal
606 extension affecting the Carpitas thrust sheet to the southeast is estimated at 4.7 km minimum.
607 The Middle-Late Eocene episode of subsidence contemporaneous with upper plate crustal
608 extension in the inner part of the forearc system has been also described along the southern
609 Ecuadorian forearc zone [*Jaillard et al*., 1997]. Our restoration shows that subsidence and
610 crustal extension could have occurred simultaneously or just after underthrusting of the
611 inferred deep tectonic slice. The total amount of internal shortening is ~22 km.

612 5.2.3 Oligocene stage (Figure 18c).

613 Geological evidence, thermochronological data and thermal modeling suggest that
614 uplift of the Amotape High reactivated between 36 and 27 Ma (Figures 4 and 16). This is
615 correlated with stratigraphic and tectonic studies through the Ecuadorian margin and northern
616 Peruvian Andes, which indicate a strong compressional event in Late Eocene-Oligocene
617 [*Noble et al*., 1990; *Naeser et al*., 1991; *Jaillard et al*., 1995, 1997]. We propose that this
618 cooling episode associated with major paleogeographic modifications (from marine to fluvial-
619 deltaic depositional environment) might result from renewed crustal stacking in the Amotape
620 thrust system. According to stratigraphic observations, the reconstruction includes that the
621 basement of the Carpitas thrust system was located above sea level. The steep dip of the
622 Carpitas paleo-slope suggests seaward tilting related to the growth of the Carpitas thrust
623 system. The restoration suggests that ~29 km of internal shortening were accommodated by
624 crustal slices and sediment underplating in the Amotape and Carpitas thrust systems. The
625 metamorphic and crystalline substratum of Amotape and upper Carpitas thrust sheets were
626 eroded during the Early Oligocene, whence it fed fluvial conglomerates made of pebbles of
627 basement quartzite and granite (i.e., Mirador, Plateritos, and Mancora Formations) into the
628 peripheral Talara and Tumbes depocenters. At this stage, the lower sedimentary sequences of
629 the Tumbes depocenter form a prograding wedge (trench-slope depocenter?) transported
630 seaward above the newly formed Banco Peru thrust system. The restoration suggests that
631 thick (~3 km) Eocene-Oligocene sedimentary sequences that were accumulated onto the
632 oceanic crust are off-scrapped and accreted in the Banco Peru thrust system.

633 5.2.4 Late Oligocene-Early Miocene stage (Figure 18d).

634 In the Late Oligocene-Early Miocene stage, the thrusting decreased (less than ~6 km
635 of internal shortening) and was associated with subsidence and the progradation of thick
636 (more than 8 km-thick) deltaic sequences of the Heath and Zorritos Formations. Continuous
637 crustal thickening of the Amotape High is related to cooling of the deepest samples through
638 the ~110°C isotherm at ca. 15 Ma. The restoration suggests that the Carpitas thrust system
639 was progressively deactivated. Subsidence associated with extension occurred on both side of
640 the Carpitas High, contemporaneous with the sedimentation of Heath Formation shales.
641 Seaward, sedimentary sequences are actively deformed by the Banco Peru thrust system. In
642 the Tumbes depocenter the sedimentary sequences describe a dissymmetric thrust-top
643 syncline on the hanging-wall of the Banco Peru thrust system. This syncline is deformed by
644 numerous gravitational raft tectonic structures and mud diapirism. The reconstruction
645 suggests that the high sedimentation rate during deposition of the Late Oligocene-Early
646 Miocene sequences onto the seaward-dipping inherited paleo-slope of the Carpitas High (and
647 to the north in the Zorritos High; Figure 14) controlled the seaward gravitational sliding in the
648 Tumbes depocenter. Similarly, the Banco Peru imbricate controlled gravitational sliding of
649 the Late Oligocene-Early Miocene series on its seaward flank. The Tumbes depocenter forms
650 an ideal trap for sediments at the rear of the active Banco Peru High. The restoration shows
651 that the formation of the Banco Peru normal fault zone (probably with a strike-slip
652 component) connected at depth onto the subduction fault might be likely due to the inversion
653 of an old thrust of the Banco Peru thrust system. This normal to strike-slip(?) fault zone
654 accommodates high sediment loading in the axis of the Tumbes depocenter. Major
655 sedimentation in the trench axis promotes formation of a new frontal imbricate also associated
656 with gravitational instabilities.

657 5.2.5 Middle-Late Miocene stage (Figure 18e).

658 During the Middle-Late Miocene stage, the structures are onlapped by the
659 transgressive Cardalitos Formation followed by prograding deltaic series of the Tumbes
660 Formation. Onshore, the Cardalitos Formation filled incised valleys [*Vega*, 2009]. Offshore,
661 the series deposited above a submarine unconformity may be associated with turbiditic or
662 ocean currents. This erosional surface also coincides with the last Miocene uplift event (see
663 section 4.2). The restoration suggests that the internal shortening decreases (~2.6 km) while
664 the apparent normal slip (~4 km) in the Banco Peru fault zone and gravitational sliding remain
665 active. Seaward, we infer that the prism overthrusts distal Late Oligocene-Late Miocene
666 sediments accumulated in the trench axis onto the basal detachment of the Banco Peru thrust
667 system.

668 5.2.6 Pliocene-Present day stage (Figure 18f).

669 The Pliocene to present-day period was associated with the offshore sedimentation of
670 the Mal Pelo, La Cruz and recent deltaic sequences. The seaward progradation of these thick
671 deltaic series at the trench axis was subjected to major gravity-driven deformation above
672 Heath Formation shales weak level. Lateral extrusion of the North Andean block may be
673 responsible for strike-slip motion along the Banco Peru fault zone and NE-trending extension
674 in the Tumbes depocenter [*Witt and Bourgois*, 2010]. Although the present seismicity along
675 the margin indicates active crustal deformation, the restoration shows that the inner prism was
676 poorly deformed since the Pliocene. As revealed by offshore subsurface data, a large volume
677 of distal sediment (~3 km-thick) was accreted to the prism and underthrusted (~31 km of
678 displacement) beneath the Banco Peru imbricate during at least the Pliocene. We infer that the
679 recent coastal uplift and moderate active deformation beneath the onshore domain is

controlled by the subduction of the Sarmiento and Alvarado 1-2 ridges [*Macharé and Ortlieb*, 1994; *Pedoja et al*., 2006; *Darrioulat*, 2011; *Villegas-Lanza et al*., 2016]. Current small sediment influx in the trench axis can be explained by the active uplift of the Banco Peru as a result of sediment underplating and ridge subduction as well as by the opening of the Guayaquil basin to the north [*Witt and Bourgois*, 2010]. The sediment trapping behind the Banco Peru in the Tumbes depocenter might be enhanced by the recent NE-trending extension and creation of accommodation space.

5.3 Shortening rate assessment

The minimum amount of horizontal shortening inferred for this sequentially restored section is ~92 km. We are aware of the fact that strike-slip motion in the Tumbes depocenter and internal normal faulting may modify slightly this shortening value. The calculated shortening rates during the Cenozoic are plotted in Figure 20 together with uplift episodes and convergence rates [*Somoza and Ghidella*, 2012]. The sequential restoration shows that major shortening rates occurred between Middle Eocene-Early Oligocene (stages b and c; ~3 mm/yr) then between Pliocene to present (stages e and f; ~5 mm/yr). The Farallon break (~24 Ma) is followed by a major decrease of the shortening. Although we cannot provide a Late Cretaceous restored state, we speculate shortening during the Paleocene-Early Eocene uplift as the Eocene-Oligocene shortening itself coincides with forearc uplift and convergence rate increase (Figure 20). This shortening increase is also more or less synchronous with magmatic pulse in the continental arc [*Schütte et al*., 2010]. Post-Miocene to present shortening is associated with forearc uplift through a convergence rate decrease.

6 Discussion

6.1 Paleo-thickness reconstruction and burial history

Apatite fission-track results indicate that post-Early Eocene sediment accumulation and burial differ in the study area. Figure 19 shows the detailed restoration of the Talara-Amotape-Lancones area along cross section B with projected apatite fission-track samples at the end of Eocene. Assuming that the top of the Late Eocene series (Chira-Verdun Formations) is slightly seaward-dipping (~2°), this pre-deformational basin architecture indicates that the Middle-Late Eocene sedimentary pile reached more than 4.5 km in thickness above the Amotape High and northwestern edge of the Lancones depocenter. This thick paleo-sedimentary pile would have favored reset of apatite fission-track system of the Early Eocene and older rocks (samples 6, 7 and 8) below the ~110°C closure temperature. In the Talara depocenter, the sedimentary fill would have been insufficient to totally reset the apatite fission-track system of samples 1, 2, 3, 4, 5 and 9. These results suggest that the offsets along the normal faults do not influenced apatite fission-track cooling age (i.e., hanging-wall exhumation) and that cooling was more controlled by thrusting. In addition, no evidence of Cenozoic intrusions or volcanism, which could influence the thermal history of the samples, is found in the study area. This reconstruction is consistent with present-day geothermal gradient of ~20-21°C/km observed in onshore exploration wells (*PERUPETRO S.A.* data). In addition, this thick paleo-sedimentary pile is consistent with high vitrinite reflectance values (0.9%-1%) measured in Cretaceous series of the Lancones depocenter [*Valencia and Uyen*, 2002].

In contrast to paleogeographic reconstructions of *Fildani et al*. [2008] and *Hessler and Fildani* [2015], our restoration shows that the Paleozoic basement of the Amotape High was totally covered by Middle-Late Eocene strata and no basement relief existed close to the study area. However, the presence of Amotape basement clasts into Middle and Late Eocene series as indicated by *Fildani et al*. [2008] and *Hessler and Fildani* [2015] may be also explained by

longitudinal drainage from the north [*Carozzi and Palomino*, 1993] where Paleozoic basement was exposed above sea level.

6.2 Forearc kinematics and subduction dynamics

Natural examples and analog models [*e.g., Daly*, 1989; *Heuret et al*., 2007; *Regalla et al*., 2013; *Martinod et al*., 2016] showed that forearc shortening and large-scale subsidence can be influenced by the dynamics of plate convergence. In the northern Peruvian margin, the overall increase in the convergence rate observed between the Nazca (Farallon) and South American plates during Paleocene to Late Oligocene [*Somoza and Ghidella*, 2012] is correlated with shortening rate increase in the forearc system. In detail, the Paleocene to Late Oligocene plate convergence history is marked by two accelerations at ~56-43 Ma and ~32-24 Ma that are approximately correlated with uplift events in the inner forearc system (Figure 20). This suggests that convergence rate acceleration leads to increase the plate coupling along the subduction fault at the scale of the forearc system [*Daly*, 1989]. The Late Cretaceous-Early Eocene event can be also correlated with the collision of oceanic terranes in the Ecuadorian margin [*Jaillard et al*., 1995, 1997] and Colombian margin [*Borrero et al*., 2012]. The Latest Eocene to Oligocene-Miocene cooling event is associated with major activity in the magmatic continental arc of northern Peru and southern Ecuador [*Schütte et al*., 2010]. According to our sequential restoration of the forearc system we believe that the flexure of the slab is modified during convergence rate acceleration (Figures 18a,c and 20). Under this condition, the restoration shows that the upper part of the slab becomes shallower while its deeper part becomes steeper as observed in analogs models of *Heuret et al*. [2007] and *Guillaume et al*. [2009]. We propose that subsequent upper plate thrust stacking and duplexing generate strong loading in the forearc system which in turn induce downward flexure of the subducting oceanic plate. This explains the strong subsidence and sediment trapping in the forearc system during Middle-Late Eocene and post-Oligocene periods following convergence rate accelerations (Figures 18b,d, and 20).

Our proposed kinematic model shows that compressional features (thrust-related structural highs) coexist with thin- and thick-skinned normal to strike-slip faults. The direction of extension is parallels to the transport direction of the thrust system (except NE-trending extensional faults in the Tumbes depocenter related to the extrusion of the North Andean block). Surface and subsurface data, and the restoration of the Tumbes depocenter show that variation of basin slope (related to imbricate growth) associated with high sedimentation rates play an important role for shallow gravity-driven thin-skinned deformations [*Mauduit and Brun*, 1998]. However, other major faults located at the rear of the Amotape, Carpitas-Zorritos, and Banco Peru imbricates (Cuzco-Angolo, Carpitas-Trigal-Tronco Mocho, and Banco Peru fault zones, respectively), connect at depth onto crustal detachments or onto the subduction fault. Downdip variations of frictional properties along the subduction interface may be influenced by the morphology of the subducting plate, lithology, fluid pressure and temperature changes [*e.g., Zhao et al*., 1986; *Hyndman et al*., 1995; *Kastner et al*., 1998; *Ikari et al*. 2009; *Schurr et al*., 2012; *Takahashi et al*. 2013; *Namiki et al*., 2014]. The development of upper plate extensional faults and subsidence zones as observed in the North Peruvian forearc system (Figure 18) may be also the consequence of basal erosion of the upper plate along the subduction interface [*Von Huene and Lallemand*, 1990; *Von Huene et al*., 2004; *Sage et al*., 2006]. In context of high convergence rate as in northern Peru, the trench sediments are less compacted and rapidly underplated under the forearc system [*Le Pichon et al.*, 1993; *Lallemand et al*., 1994]. Thus, the high pore-fluid pressure along the subduction interface may contribute to decrease locally the plate coupling, which in turn may favor the drag of upper plate material into the subduction channel, leading to upper plate normal faulting and subsidence [*Von Huene et al*., 2004].

Onshore post-Oligocene rotations and inferred strike-slip component along the Banco Peru fault zone might be associated with oblique subduction context of the Northern Andes [*Villegas-Lanza et al*., 2016] but also with collision of broad indentors immediately north of the study area along the Ecuadorian margin (oceanic terranes and Carnegie ridge) and northern escape of the North Andean block [*e.g., Daly*, 1989; *Witt and Bourgois*, 2010]. Strike-slip motion in context of oblique subduction may be an alternation to create apparent crustal normal faulting in forearc system [*Takano et al*., 2013; *Bourgois*, 2013; *Noda and Miyakawa*, 2017], which would be consistent with inferred strike-slip motions, at least, in the Banco Peru fault zone.

The sequential restoration presented in this study does not reveal tectonic relationship between age variations of the subducting oceanic lithosphere [*Sdrolias and Müller*, 2006] and the evolution of the North Peruvian forearc system. As well, whatever the subduction age of the Inca Plateau (Early or Middle Miocene; *Gutscher et al*., 1999b; *Skinner and Clayton*, 2013) and its associated eastern Pliocene to present slab flattening beneath the arc [*Espurt et al*., 2008], these processes seem to have no major impact on the structural architecture and evolution of the North Peruvian forearc system. However, the subduction of the trench-oblique, parallel-upper plate structural trend Sarmiento and Alvarado ridges might be associated with recent forearc uplift with perched marine terraces and Tablazos [*Macharé and Ortlieb*, 1994; *Pedoja et al*., 2006; *Darrioulat*, 2011] together with moderate active deformation beneath the onshore domain [*Villegas-Lanza et al*., 2016] as observed in the central Ecuador, central Peru and central Chile margins [e.g., *Laursen et al.*, 2002; *Saillard et al*., 2011; *Collot et al*., 2017].

6.3 Influence of sedimentation and forearc tectonic

Sedimentation may have also strong influence on geometry and fault dynamics of forearc systems [e.g., *Fuller et al*., 2006; *Simpson*, 2010; *Heuret et al*., 2012]. Since the Early Eocene, siliciclastic sediments eroded from the Northern Andes of Ecuador and Peru were transported by longitudinal and transverse drainages and deltas in the forearc zone [*Séranne*, 1987; *Carozzi and Palomino*, 1993; *Higley*, 2004; *Fildani et al*., 2008; *Quispe Alcalá*, 2010]. As described above, our sequential model shows that thick sedimentary piles of the Talara and Tumbes depocenter are associated with deep seated normal to strike-slip faults. We suggest that the high sedimentation amounts (up to 11 km-thick) increases the vertical stress in these depocenters [*Simpson*, 2010]. In the case of the Talara-Lancones depocenter, basal drag may have initiated normal (to strike-slip?) faulting along the Tronco Mocho, Carpitas-Trigal and Cuzco-Angolo fault systems which have been controlled in a second time by large sedimentation rates during Middle-Late Eocene and post-Early Oligocene. In the case of the Tumbes depocenter, we propose that the Late Oligocene to present-day high sediment influx was sufficient to influence the apparent normal slip of the Banco Peru fault. Thus, this sedimentary load played a major role in the deformation of the Banco Peru, in probably controlling its trenchward displacement. This behavior may reflect spatial variations of frictional properties along the subduction with low friction beneath the Banco Peru. This interpretation is consistent with the present-day aseismic slip of the plate interface in northern Peru [*Bourgois*, 2013; *Villegas-Lanza et al*., 2016] and any significant earthquake in this zone [*Bilek*, 2010].

6.4 Forearc/backarc system evolution and growth of the Northern Andes

Foreland systems record the large-scale interactions between tectonics, erosion and sedimentation [*e.g., Jordan*, 1995; *DeCelles and Giles*, 1996; *Horton*, 1999]. Building of the Andean orogenic wedge since the Late Cretaceous led to large-scale orogenic loading control

on adjacent Cenozoic foreland basins [*Iaffaldano et al*., 2006; *Roddaz et al*., 2010]. As suggested by *Jaillard et al*. [1997], we propose that the collision of oceanic terranes in the Northern Andes accounts for additional deformations during Late Paleocene-Early Eocene. The regional unconformity overlain by the Early Eocene Mogollon-Salinas Formation maybe interpreted as an unloading stage of the orogenic wedge and westward distribution of thrusting into the forearc zone. The Middle-Late Eocene inner subsidence and large sediment influx in the North Peruvian forearc system may be also controlled by internal crustal stacking and associated loading of the Andean orogenic wedge as revealed by thrust-induced exhumation at ca. 45 Ma in the Western Cordillera of Ecuador [*Spikings et al*., 2010]. Ongoing Oligocene to Miocene orogenic building and magmatic arc activity [*Schütt et al.*, 2010] are associated with high subsidence rates and thrust-induced exhumation into the forearc system. Middle-Late Miocene final thrust-related exhumation in the northern Peruvian margin coincides with thrust tectonic loading of the Eastern Cordillera, shortening transfer into the Peruvian Subandean zone [*Espurt et al*., 2011; *Eude et al*., 2015], onset of the main phase of Andean Plateau uplift and associated flexural subsidence in the Amazonian foreland basin [*Roddaz et al*., 2010]. Modern relief development and west-directed drainage system provide a major sediment influx and overfill of the North Peruvian forearc system. This induces additional loading in the forearc system, which favors forward thrust propagation (Erdos et al., 2015).

7 Conclusions

The main conclusions of this study are summarized in the following five points.

(1) Surface and subsurface data and the construction of two ~200 km-long crustal-scale balanced cross sections show that the structure of the North Peruvian forearc system is dominated by an accretionary style through the Late Cretaceous to Cenozoic period with northwestward propagation of thrust-related structural highs involving basement, oceanic rocks and off-scrapped sediments. The thrust-related structural highs bound thick thrust-top forearc depocenters deformed by crustal normal to strike-slip faults and thin-skinned gravitational instabilities.

(2) Apatite fission-track data, thermal modeling and geological data from the inner forearc system (Amotape High area) indicate two episodes of cooling/erosion, Late Cretaceous(?)-Early Eocene (~80–50 Ma) and Latest Eocene-Early Oligocene (36–27 Ma) to Middle Miocene, separated by a period of strong subsidence, burial and reheating during Middle-Late Eocene. These two cooling events recorded basement thrust exhumation and occurred approximately during periods of convergence rate acceleration.

(3) This study suggests that convergence rate acceleration leads to increase the plate coupling at the scale of the forearc system. Although the sequential restoration provides forearc shortening rate for only five periods, we show a correlation between uplift, shortening and plate convergence velocity between Late Cretaceous and ~5 Ma. Late Cretaceous-Early Oligocene shortening is accommodated by basement accretion of the Amotape and Carpitas thrust systems underneath the Lancones and Talara forearc depocenters, respectively. The growth of the frontal Banco Peru imbricate occurred during Oligocene-Miocene and structurally contributes to strong sedimentary accumulation in the Tumbes forearc depocenter. Post-Miocene to present-day uplift and frontal shortening in context of relatively lower convergence rate mostly result from the subduction of bathymetric asperities/ridges.

(4) The development of SE-facing crustal normal to strike-slip faults and large-scale subsidence zones during overall forearc system accretion might be the consequence of slab flexure, basal erosion along subduction plate interface, and/or strike-slip component in the

context of oblique subduction of the northern Peruvian margin. Strong sedimentation rate may increase the apparent normal fault displacement and thrust propagation in the prism, particularly in the case of the Tumbes forearc depocenter-Banco Peru system.

(5) The North Peruvian forearc system has recorded the building of the Northern Andes and its associated orogenic loading evolution over the Cenozoic.

Acknowledgments

This work was conducted thanks to the Institut de Recherche pour le Développement (IRD)–PERUPETRO S.A. research agreement. Financial support for field work and analysis came from IRD (UR 234), CEREGE (internal research grant: Characterization and quantification of the deformations in a complex compressional basin: the Tumbes-Talara forearc basin, North Peru), and the Institut Carnot ISIFoR (Research project: Structural modeling and petroleum simulations in complex zones: insight into the giant petroleum field of the Nord Peruvian forearc). Midland Valley Inc. is acknowledged for providing academic license of Move for structural modeling. We acknowledge the associate editor Augusto Rapalini, Agustin Cardona and an anonymous reviewer for the constructive comments which greatly helped us to improve our manuscript. Supporting data are included in supporting information or available by contacting the corresponding author (espurt@cerege.fr).

886

Sample name/ Structural unit	Long. (m)	Lat. (m)	Elev. (masl)	Strat. age	Gr	Ns	ρ(cm^2)	σρ	P	σP	χ2	Q(χ2)	Pooled age (Ma)	Central age (Ma)	CP1 (Ma)	% grains in CP1	CP2 (Ma)	% grains in CP2	CP3 (Ma)	% grains in CP3	MTL (μm)	Stdev (μm)	Dpar (μm)
1/Talara	514 429	9 542 461	175	Middle Eocene	38	835	1.7 10-4	1.2 10-7	1.499	9.8E10-3	157.6	0	40.1(-3.0,3.2)	43.2±3.7	28.8±1.9	38	50.7±2.7	56	120±19	7	12.49±0.14(202)	1.95	2.32
2/Talara	510 910	9 541 031	111	Early Eocene	38	494	9.7 10-5	4.7 10-7	1.463	9.8E10-3	48.8	0.1	42.1(-3.9,4.3)	46.8±3.0	38.8±2.7	47	57.1±6.8	53	-	-	12.31±0.13(200)	1.8	2.44
3/Talara	512 239	9 542 139	135	Middle Eocene	40	553	1.1 10-4	5.3 10-7	1.4866	9.8E10-3	57.1	0	40.6(-3.7,3.9)	45.1±2.7	36.2±2.6	43	54.1±6.1	57	-	-	12.83±0.39(202)	5.46	2.26
4/Talara	5150.32	9 541 539	186	Middle Eocene	40	1142	1.8 10-4	7.4 10-7	1.478	9.8E10-3	118.8	0	52.4(-3.5,3.7)	52.5±3.1	36.7±2.5	35	63.1±2.4	65	-	-	12.45±0.12(201)	1.64	2.22
5/Talara	542 492	9 566 482	129	Early Eocene	34	438	7.2 10-5	3.1 10-7	1.4636	9.8E10-3	60.1	0	49.8(-4.8,5.3)	52.1±3.7	37±18	9	50.5±5.1	83	116±23	8	13.01±0.12(205)	1.66	2.41
6/Amotape	543 166	9 553 245	319	Triassic (granite)	40	1479	7.7 10-4	1,8 10-6	1.5377	9.8E10-3	69.7	0	15.8(-0.9,1.0)	15.8±0.6	-	-	-	-	-	-	12.19±0.15(209)	2.14	1.89
7/Lancones	558 190	9 553 866	230	Late Cretaceous	40	1437	6.8 10-4	1.6 10-6	1.469	9.8E10-3	108	0	17.2(-1.0,1.1)	17.5±0.7	14.8±0.7	67	22.7±1.2	33	-	-	12.86±0.11(181)	1.46	1.88
8/Amotape	526 492	9 542 910	314	Early Eocene	40	334	1.0 10-4	5.3 10-7	1.4799	9.8E10-3	101.2	0	27.1(-2.9,3.3)	29.7±2.9	20.9±2.2	57	45.7±4.5	43	-	-	12.58±0.15(163)	1.94	2.43
9/Talara	519 306	9 539 698	210	Early Eocene	36	161	2.6 10-5	1.5 10-7	1.4621	9.8E10-3	26.8	0.8	51.63(-7.7,9.0)	56.1±4.4	-	-	-	-	-	-	12.47±0.15(128)	1.75	2.44

887 **Table 1.** Apatite fission-track data using laser ablation-inductively coupled plasma-mass spectrometry method. Gr–number of counted grains;
888 Ns–sum of spontaneous tracks; ρ–area of spontaneous track counting with its error (σρ); P–corrected $^{238}U/^{43}Ca$ isotopic ratio (10^{-3}) with its error
889 (σP); ICPMS Zeta factor is 8.2727±0.1407; CP1-3–Component peak ages (1 to 3) from RadialPlotter [*Vermeesch*, 2009] (see supporting
890 information Figure S1); MTL–Mean track length (number of tracks); Dpar–mean maximum diameter of fission-track etch figures parallel to the
891 c-axis; Pooled ages are -+95 % Cl confidence interval; Central and peak ages are ±1σ; Coordinates are in UTM Zone 17S.

892 **Figure 1.** Geodynamic settings. (a): Physiographic map of the northern Peruvian-Ecuadorian
893 Andes. The base map is produced using elevation data from NASA (National Aeronautics and
894 Space Administration) 30 m ASTER (Advanced Spaceborne Thermal Emission and
895 Reflection Radiometer) GDEM (Global Digital Elevation Model). Plate convergence vector
896 and velocities (mm/yr) are from *Gripp and Gordon* [2002]. Mapping, vector and velocities
897 (mm/yr) of the continental slivers are from *Villegas-Lanza et al*. [2016]. GR: Grivalja ridge.
898 AR1-2: Alvarado ridges 1 and 2. SR: Sarmiento ridge. SB: Sechura basin. GB: Guayaquil
899 basin. PH: Paita High. IH: Illescas High. WC: Western Cordillera. HD: Huancabamba
900 deflection (dashed white line). STF: Subandean thrust front. NAFB: Northern Andean
901 foreland basin. (b): Onshore-offshore structural map of the study area showing major forearc
902 depocenters (FD) and structural highs. Locations of cross sections A and B, seismic profiles
903 and onshore wells (CORV40, DEL39, P. RED18) are shown. Red lines show faults. HF:
904 Huaypirá fault. EFZ: La Encanada fault zone. CAF: Cuzco-Angolo fault. CFZ: Carpitas fault
905 zone. TMFZ: Tronco Mocho fault zone. BPFZ: Banco Peru fault zone. Coordinate system is
906 UTM zone 17S.

907 **Figure 2.** Synthetic stratigraphy, lithology and chart of the Cretaceous to Cenozoic series
908 across the North Peruvian forearc system [*Jaillard et al*., 1999; *Pozo*, 2002; *Valencia and*
909 *Uyen*, 2002; *Fernández et al*., 2005; *Fildani et al*., 2008; *Vega*, 2009; *Hessler and Fildani*;
910 2015]. Cretaceous-Cenozoic depocenters are separated by structural highs made of
911 sedimentary, continental and oceanic materials. Major unconformities are shown. U1: Basal
912 Cretaceous unconformity 1. U2: Late Cretaceous unconformity. U3: Early Eocene
913 unconformity. U4: Late Eocene-Oligocene unconformity. U5: Middle Miocene unconformity.

914 **Figure 3.** Geologic map of the onshore study area showing onshore cross sections A and B,
915 seismic reflection profiles and wells. This map is based on new field mapping and published
916 maps of INGEMMET and petroleum companies. FD: Forearc depocenter. CFZ: Carpitas fault
917 zone. TF: Trigal fault. CVF: Cabeza de Vaca fault. TMFZ: Tronco Mocho fault zone. CAF:
918 Cuzco-Angolo fault. EFZ: La Encanada fault zone. Coordinate system is UTM zone 17S.

919 **Figure 4.** Geological field observations illustrating two major unconformities (U3 and U4) in
920 the onshore domain. For locations, see Figures 1b, 3, 5 and 10. (a) Paleozoic metamorphic
921 rocks of the Amotape High unconformably covered by strata of the Early Eocene Mogollon-
922 Salinas Formation. (b) Pennsylvanian turbidites of the Chaleco de Paño Formation
923 unconformably covered by strata of the Early Eocene Mogollon-Salinas Formation
924 (southwestern edge of the Amotape High, High Talara River). (c) and (d) Subaerial erosional
925 surface between basal marine Late Eocene Chira Formation and upper fluvial Latest Eocene-
926 Oligocene series (Mirador, Plateritos and Mancora Formations). (e) Growth strata geometry in
927 the Oligocene Plateritos sequences along the Bocapan River.

928 **Figure 5.** Surface cross sections A and B across the onshore domain of the Talara and
929 Lancones forearc depocenters. For locations, see Figure 3. Locations of seismic profiles (L1,
930 BPZ23-16 and PXII99-02) and wells are shown. Major unconformities (U1-5) are also
931 indicated. ZH: Zorritos High. CH: Carpitas High. FD: Forearc Depocenter. TMFZ: Tronco
932 Mocho fault zone. TF: Trigal fault. CAF: Cuzco-Angolo fault. EFZ: La Encanada fault zone.
933 CFZ: Carpitas fault zone. CVF: Cabeza de Vaca fault.

934 **Figure 6.** Details of the NW-verging Jabonillos thrust fault zone through the Turonian
935 Encuentros Formation in the Lancones depocenter. For location, see Figure 3.

936 **Figure 7.** Geological field observations illustrating the polyphased fault kinematics in the
937 study area. For locations, see Figures 1b, 3 and 5. (a) Inversion and triangle zone in the Albian
938 Pananga Formation in the northwestern Lancones depocenter. (b) Extensional reactivation of
939 a fault-bend fold in the Early Eocene Mogollon-Salinas Formation in the Talara depocenter
940 (northern Bocapan River, cross section A). (c) Thrust propagating with short-cut trajectory
941 through normal fault in Middle Eocene Talara Formation in the Talara depocenter (northern
942 Fernandez River). Numbers refer to fault sequence.

943 **Figure 8.** Structural interpretation of seismic profile PXII99-02 in the center part of the
944 Lancones depocenter across the Gallinazos anticline. For location, see Figure 3. Faults are
945 indicated by thick red lines. Note that some thrust faults connect with the Amotape Paleozoic
946 basement. These faults may correspond to inherited normal fault active during the Early
947 Cretaceous (e.g., Figure 7a). Shales of the Muerto Formation form a shallower thin-skin
948 décollement level. Unconformity U1 is shown. TWT: two-way time.

949 **Figure 9.** Extensional faulting in the Eocene series of the Talara forearc depocenter between
950 the Carpitas and Cabeza de Vaca faults, cross section B. For locations, see Figures 3, 5 and
951 10). U4: Unconformity 4.

952 **Figure 10.** Structural interpretation of depth-converted seismic profile BPZ23-16 calibrated
953 with wells and surface data across the Talara forearc depocenter between the Amotape High
954 to the southeast and the Carpitas High to the northwest (cross section B). For location, see
955 Figure 3. Faults are indicated by thick red lines. Eocene series are deformed by extensional
956 faults. These faults branch at depth onto SE-dipping low-angle thrust faults within the
957 Amotape Paleozoic basement. These thrust faults extend southeastward below the Amotape
958 High. Unconformities U3 and U4 are shown. Locations of exploration wells and oil plays are
959 also shown.

960 **Figure 11.** Geological field observations illustrating the gravitational instabilities in the shales
961 of the Late Oligocene-Early Miocene Heath Formation, cross section A. (a): Bocapan River.
962 (b) Animas River. For location, see Figures 3 and 5.

963 **Figure 12.** Structural interpretation of depth-converted seismic profile L1 across the Zorritos
964 High calibrated with wells and surface data, cross section A. For location, see Figure 3. Faults
965 are indicated by thick red lines. Note the extensional tectonic deforming Eocene-Early
966 Miocene series corresponding to the Tronco Mocho fault zone. The normal faults show small
967 inversion with short-cut geometries. Note also the unconformity U4 of the Oligocene
968 Plateritos/Mancora Formations above the Early Eocene series and Amotape basement.
969 Unconformities U3 and U5 are also shown. See details in the text.

970 **Figure 13.** Structural interpretation of the offshore domain of cross section B using depth-
971 converted seismic profiles AIP92-15, L2, VMX09-23 and RIB93-1 across the Tumbes forearc
972 depocenter (FD), Banco Peru and Trench-Slope Basin calibrated with the projected (pjt.)
973 DEL39 well. For location, see Figure 1b. Small inversions and compressional structures are
974 suspected on the seaward side of the Carpitas High. Onshore structure along seismic line
975 BPZ23-16 of Figure 10 is also shown. Faults are indicated by thick red lines. Unconformities
976 U3-5 are shown. BPFZ: Banco Peru fault zone. See details in the text.

977 **Figure 14.** Structural interpretation of the offshore domain of cross section A using depth-
978 converted seismic profiles PC99-11, L3 and VMX09-01 across the Tumbes forearc
979 depocenter (FD) calibrated with the DEL39 well. Note that the COR18 and P.RED18 wells

have been projected (pjt.). For location, see Figure 1b. Note the major compressional structures on the seaward side of the Zorritos High. Onshore structure along seismic Line 1 of Figure 12 is also shown. Faults are indicated by thick red lines. Unconformities U3-5 are shown. BPFZ: Banco Peru fault zone. See details in the text.

Figure 15. Apatite fission-track data (sample location and number; central and component peak ages in Ma; see Table 1) in the onshore study area (Talara, Amotape and Lancones units). FD: Forearc depocenter. TMFZ: Tronco Mocho fault zone. CFZ: Carpitas fault zone. TF: Trigal fault. CAF: Cuzco-Angolo fault. For legend of the sedimentary units, see Figure 3.

Figure 16. HeFTy inverse thermal modeling for samples 2, 6, 7 and 8 from the Talara, Amotape and Lancones units. The modeling together with geological data show time-temperature histories for two uplift episodes (Late Cretaceous(?)-Early Eocene and Late Eocene-Oligocene) separated by a major subsidence and burial/reheating period during Middle-Late Eocene. Light and dark grey fields represent acceptable and good model fits, respectively. The blue line represents the weighted mean path of the model. FD: Forearc depocenter.

Figure 17. Crustal-scale cross sections across the North Peruvian forearc system. For location, see Figure 1b. FD: Forearc depocenter. Write circles correspond to Mw>5 seismic events from the "Instituto Geofísico del Perú" catalog 2005-2013 (http://www.igp.gob.pe). Seismic events are projected along 100 km-wide corridors centered on the cross sections. Major normal fault systems are shown. Position of the apatite fission-track samples is also shown (small black circles). CAF: Cuzco-Angolo fault. EFZ: La Encanada fault zone. CFZ: Carpitas fault zone. TF: Trigal fault. TMFZ: Tronco Mocho fault zone. BPFZ: Banco Peru fault zone. SR: Sarmiento ridge. AR1-2: Alvarado ridges 1 and 2.

Figure 18. Crustal-scale sequential restoration of the North Peruvian forearc system along cross section B. See Figure 1b for location and Figure 17 for legend of the sedimentary units. Note that major thrust sheets are labelled (1 to 10). Position of the apatite fission-track samples is also shown (small black circles). Vertical black arrows indicate downward flexure of the slab. LD: Lancones depocenter. AH: Amotape High. TD: Talara depocenter. TUD: Tumbes depocenter. BP: Banco Peru. CAF: Cuzco-Angolo fault. EFZ: La Encanada fault zone. CFZ: Carpitas fault zone. BPFZ: Banco Peru fault zone. SR: Sarmiento ridge. AR1-2: Alvarado ridges 1 and 2. AFT: Apatite fission-track. See details in the text.

Figure 19. Restoration of the apatite fission-track samples at the end of the Middle-Late subsidence in the Amotape High (Figures 18b). See details in the text. White bars represent good model fits from the HeFTy inverse modeling of Figure 16. Dashed black line indicates the ~110°C temperature closure of the apatite fission-track system according to a ~20°C/km geothermal gradient and ~20°C surface temperature near the bottom of the sea. The restoration is consistent with apatite fission-track and thermal modeling results: samples 6, 7 and 8 are reset whereas samples 1, 2, 3, 4, 5 and 9 are not or partially reset. Note the vertical exaggeration. FD: Forearc depocenter.

Figure 20. Comparison between convergence rate of the Nazca (Farallon)-South American plate system [*Somoza and Ghidella*, 2012] and shortening rate in the North Peruvian forearc system calculated from the sequentially balanced cross section B in Figure 18. In detail, the increase of convergence rate at ~56-43 Ma and ~32-24 Ma is somewhat correlated with uplift events in the inner forearc system while the following subsidence periods fit with stable or decrease of plate convergence rate. Dashed grey lines shows mean convergence rate. (a-f):

Restoration stages of Figure 18. FB: Farallon breakup. IP: Inca Plateau subduction. CR: Carnegie ridge subduction. SR and AR: Subduction of the Sarmiento and Alvarado ridges. Cooling and reheating periods of the apatite fission-track (AFT) system and major uplift and subsidence (Subs.) periods are shown.

References

Alvarado, A., L. Audin, J. M. Nocquet, E. Jaillard, P. Mothes, P. Jarrín, M. Segovia, F. Rolandone, and D. Cisneros (2016), Partitioning of oblique convergence in the Northern Andes subduction zone: Migration history and the present-day boundary of the North Andean Sliver in Ecuador, Tectonics, 35, 1048–1065,doi:10.1002/2016TC004117.

Azalgara, C. (1993), Structural evolution of the offshore forearc basins of Peru, including the Salaverry, Trujillo, Lima, west Pisco and east Pisco basins, PhD thesis, Rice University, Houston, Texas, UMI Bell & Howell Publishing, 300 North Zeeb Road. Ann Arbor, MI 48106-1346 USA, 178 p.

Andamayo, K. (2008), Nuevo estilo estructural y probables sistemas petrolíferos de la cuenca Lancones, Tesis Ing. Geol., Universidad Nacional Mayor de San Marcos, 129 p.

Antoine P.-O., G. Billet, R. Salas-Gismondi, J. Tejada-Lara, P. Baby, S. Brusset, and N. Espurt (2015), A new Carodnia Simpson, 1935 (Mammalia, Xenungulata) from the early Eocene of Northwestern Peru and a phylogeny of xenungulates at species level, Journal of Mammalian Evolution, 22, 129–140, doi: 10.1007/s10914-014-9278-1.

Auguy, C., G. Calvès, Y. Calderon, and S. Brusset (2017), Seismic evidence of gas hydrates, multiple BSRs and fluid flow offshore Tumbes Basin, Peru, Marine Geophysical Research, 10, 339–339, doi: 10.1007/s11001-017-9319-2.

Bailleul, J., C. Robin, F. Chanier, F. Guillocheau, B. Field, and J. Ferrière (2007), Turbidite systems in the inner forearc domain of the Hikurangi convergent margin (New Zealand): new constraints on the development of trench-slope basin, Journal of Sedimentary Research, 77, 263–283, doi: 10.2110/jsr.2007.028.

Barnes, P. M., A. Nicol, and T. Harrison (2002), Late Cenozoic evolution and earthquake potential of an active listric thrust complex above the Hikurangi subduction zone, New Zealand, Geological Society of America Bulletin, 114, 1379–1405, doi: 10.1130/0016-7606.

Benavente, C., S. Zerathe, L. Audin, S. R. Hall, X. Robert, F. Delgado, J. Carcaillet, and A. S. T. E. R. Team (2017), Active transpressional tectonics in the Andean forearc of southern Peru quantified by 10Be surface exposure dating of an active fault scarp, Tectonics, doi:10.1002/2017TC004523.

Bilek, S. L. (2010), Invited review paper: Seismicity along the South American subduction zone: Review of large earthquakes, tsunamis, and subduction zone complexity, Tectonophysics, 495(2), 2–14, doi:10.1016/j.tecto.2009.02.037.

Borrero, C., A. Pardo, C. M. Jaramillo, J. A. Osorio, A. Cardona, A. Flores, S. Echeverri, S. Rosero , J. García, and H. Castillo (2012), Tectonostratigraphy of the Cenozoic Tumaco forearc basin (Colombian Pacific) and its relationship with the northern Andes orogenic build up, Journal of South American Earth Sciences, 39, 75–92, doi:10.1016/j.jsames.2012.04.004.

Bosworth, T. O. (1922), Geology of the Tertiary and Quaternary Periods in the Northwest Part of Peru, Macmillan and Company, London, UK, 434pp.

1070 Bourgois, J., G. Pautot, M. Sosson, and P. Huchon (1989), Campagne SEAPERC: étude de la
1071 déformation le long d'une marge convergente de type andin, Colloque Tour du Monde
1072 du Jean Charcot Paris. 2–3 Mars 1989, IFREMER-INSU-ORSTOM.

1073 Bourgois, J. (2013), A Review on Tectonic Record of Strain Buildup and Stress Release
1074 across the Andean Forearc along the Gulf of Guayaquil-Tumbes Basin (GGTB) near
1075 Ecuador-Peru Border, International Journal of Geosciences, 4, 618–635.

1076 Boyer, S. E., and D. Elliott (1982), The geometry of thrust systems, The American
1077 Association of Petroleum Geologists Bulletin, 66, 1196–1230.

1078 Calahorrano, A. (2005), Structure de la marge du Golfe de Guayaquil (Equateur) et propriété
1079 physique du chenal de subduction, à partir de données de sismique marine réflexion et
1080 réfraction, Université Paris VI, Paris. Ph.d. thesis, 227 p.

1081 Calvès, G., C. Auguy, L. de Lavaissière, S. Brusset, Y. Calderon, and P. Baby (2017), Fore-
1082 arc seafloor unconformities and geology: Insight from 3-D seismic geomorphology
1083 analysis, Peru, Geochem. Geophys. Geosyst., 18, 3062–3077,
1084 doi:10.1002/2017GC007036.

1085 Carlson, W. D., R. A. Donelick, and R. A. Ketcham (1999), Variability of apatite fission-track
1086 annealing kinetics: I. Experimental results, American Mineralogist, 84, 1213–1223.

1087 Carminati, E., S. Fabbi, and M. Santantonio (2014), Slab bending, syn-subduction normal
1088 faulting, and out-of-sequence thrusting in the Central Apennines, Tectonics, 33, 530–
1089 551, doi:10.1002/2013TC003386.

1090 Carozzi, A. V., and J. R. Palomino (1993), The Talara Forearc Basin, NW Peru: Depositional
1091 Models Of Oil-Producing Cenozoic Clastic Systems, Journal of Petroleum Geology,
1092 16, 5–32. doi:10.1111/j.1747-5457.1993.tb00728.x

1093 Chanier, F., J. Ferrière, and J. Angelier (1999), Extensional deformation across an active
1094 margin, relations with subsidence, uplift and rotations: the Hikurangi subduction, New
1095 Zealand, Tectonics, 18, 862–876.

1096 Chew, D. M., and R. A. Donelick (2012), Combined apatite fission track and U-Pb dating by
1097 LA-ICP-MS and its application in apatite provenance analysis, Chapter 12, in
1098 Sylvester, P., ed., Quantitative Mineralogy and Microanalysis of Sediments and
1099 Sedimentary Rocks: Mineralogical Association of Canada Short Course 42, p. 219–
1100 247.

1101 Chlieh M., et al. (2014), Distribution of discrete seismic asperities and aseismic slip along the
1102 Ecuadorian megathrust, Earth and Planetary Science Letters, 400, 292–301.

1103 Clift, P. D., I. Pecher, N. Kukowski, and A. Hampel (2003), Tectonic erosion of the Peruvian
1104 forearc, Lima Basin, by subduction and Nazca Ridge collision, Tectonics, 22(3), 1023,
1105 doi:10.1029/2002TC001386.

1106 Clift, P. D., and P. Vannucchi (2004), Controls on tectonic accretion versus erosion in
1107 subduction zones: implications for the origin and recycling of the continental crust,
1108 Rev. Geophys., 42, RG20001, doi: 10.1029/2003RG000127.

1109 Collot, J.-Y., E. Sanclemente, J.-M. Nocquet, A. Leprêtre, A. Ribodetti, P. Jarrin, M. Chlieh,
1110 D. Graindorge, and P. Charvis (2017), Subducted oceanic relief locks the shallow
1111 megathrust in central Ecuador, J. Geophys. Res. Solid Earth, 122,
1112 doi:10.1002/2016JB013849.

1113 Collot, J.-Y., A. Ribodetti, W. Agudelo, and F. Sage (2011), The South Ecuador subduction
1114 channel: Evidence for a dynamic mega-shear zone from 2D fine-scale seismic
1115 reflection imaging and implications for material transfer, J. Geophys. Res., 116,
1116 B11102, doi:10.1029/2011JB008429.

1117 Collot, J.-Y., F., Michaud, A., Alvarado, B., Marcaillou, M., Sosson, G., Ratzov, F., Migeon,
1118 A., Calahorrano, and A., Pazmino (2009), Visión general de la morfología submarina
1119 del margen convergente de Ecuador–Sur de Colombia: implicacionese sobre la
1120 transferencia de masa y la edad de la subducción de la Cordillera de Carnegie. In:
1121 Collot, J.-Y., Sallares, V., Pazmino, N. (Eds.), Geología y Geofísica Marina y
1122 Terrestre del Ecuador: Desde La Costa Continental Hasta Las Islas Galápagos.
1123 CNDM/INOCAR/IRD, Guayaquil, pp. 47–74.

1124 Collot, J.-Y., B. Marcaillou, F. Sage, F. Michaud, W. Agudelo, P. Charvis, D. Graindorge,
1125 M.-A. Gutscher, and G. Spence (2004), Are rupture zone limits of great subduction
1126 earthquakes controlled by upper plate structures? Evidence from multichannel seismic
1127 reflection data acquired across the northern Ecuador–southwest Colombia margin,
1128 Journal of Geophysical Research, 109(B11103), doi: 10.1029/2004JB003060.

1129 Collot, J.-Y., P. Charvis, M.-A. Gutscher, and E. Operto (2002), Exploring the Ecuador-
1130 Colombia active margin and inter-plate seismogenic zone, Eos (Transactions,
1131 American Geophysical Union), 83, 189–190, doi:10.1029/2002EO000120.

1132 Dahlstrom, C. D. A. (1969), Balanced cross sections, Canadian Journal of Earth Sciences, 6,
1133 743–757.

1134 Daly, M. C. (1989), Correlations between Nazca/Farallon plate kinematics and forearc basin
1135 evolution in Ecuador, Tectonics, 8, 769–790.

1136 Darrioulat, A. (2011), Marine terraces and neotectonics in Northern Peru, Master 2
1137 Recherche, Sciences de la Terre et de l'Univers - Spécialité Terre Solide, Université
1138 Joseph Fourier – 41p.

1139 Deniaud, Y., P. Baby, C. Basile, M. Ordoñez, G. Montenegro, and G. Mascle (1999),
1140 Ouverture et évolution tectono-sédimentaire du golfe de Guayaquil: Bassin d'avant-
1141 arc néogène et quaternaire du sud des Andes équatoriennes, C. R. Acad. Sci. Ser. 2,
1142 328, 181 – 187.

1143 DeVries, T. J. (1988), The geology of late Cenozoic marine terraces (tablazos) in
1144 northwestern Peru, Journal of South American Earth Sciences, 1 (2), 121–136.

1145 Dickinson, W. R. (1995), Forearc basins, in Busby, C.J., and Ingersoll, R.V., eds., Tectonics
1146 of Sedimentary Basins: Oxford, UK, Blackwell Science, 221–261.

1147 Dickinson, W. R., and D. R. Seely (1979), Structure and stratigraphy of forearc regions,
1148 AAPG Bull., 63(1), 2–31.

1149 Encinas, A., K. L. Finger, L. A. Buatois, and D. E. Peterson (2012), Major forearc subsidence
1150 and deep-marine Miocene sedimentation in the present Coastal Cordillera and
1151 Longitudinal Depression of south-central Chile (38°30′S–41°45′S), Geological Society
1152 of America Bulletin, 124, 1262–1277; doi: 10.1130/B30567.1.

1153 Erdos, Z., R. S. Huismans, and P. van der Beek (2015), First-order control of syntectonic
1154 sedimentation on crustal-scale structure of mountain belts, Journal of geophysical
1155 research, 120, 5362–77, doi:10.1002/2014JB011408.

1156 Espurt, N., F. Funiciello, J. Martinod, B. Guillaume, V. Regard, C. Faccenna, and S. Brusset
1157 (2008), Flat subduction dynamics and deformation of the South American plate:
1158 Insights from analog modeling, Tectonics, 27, TC3011, doi:10.1029/2007TC002175.

1159 Espurt N., J. Barbarand, M. Roddaz, S. Brusset, P. Baby, M. Saillard, and W. Hermoza (2011)
1160 A scenario for Late Neogene Andean shortening transfer in the Camisea Subandean
1161 zone (Peru, 12°S): implications for growth of the northern Andean Plateau, Geological
1162 Society of America Bulletin, 123, 2050–2068, doi: 10.1130/B30165.1.

1163 Etris, E.L., N.J. Crabtree, and J. Dewar (2001), True depth conversion: more than a pretty
1164 picture. CSEG Rec. 26, 11-22.

1165 Eude, A., M. Roddaz, S. Brichau, S. Brusset, Y. Calderon, P. Baby, and J.-C. Soula (2015),
1166 Controls on timing of exhumation and deformation in the northern Peruvian eastern
1167 Andean wedge as inferred from low-temperature thermochronology and balanced
1168 cross section. Tectonics, 34, 715–730. doi: 10.1002/2014TC003641.

1169 Fernández, J., E. Martínez, Y. Calderón, W. Hermoza, and C. Galdos (2005), Tumbes and
1170 Talara basins hydrocarbon evaluation, Perupetro S.A., Basin Evaluations Group
1171 Exploration Department, 130 p, internal report available in website
1172 www.perupetro.com.pe.

1173 Fildani, A., A. M. Hessler, and S. A. Graham (2008), Trenchforearc interactions reflected in
1174 the sedimentary fill of Talara Basin, northwest Peru, Basin Research, 20(3), 305–331,
1175 doi: 10.1111 /j.1365-2117.2007.00346.x.

1176 Fildani, A., A. D. Hanson, Z. Chen, M. J. Moldowan, S. A. Graham, and P. R. Arriola (2005),
1177 Talara basin petroleum system: geochemical characteristics of oils and correlation
1178 with possible source rocks from NW Peru, Am. Assoc. Petrol. Geol. Bull., 89, 1519–
1179 1545, doi: 10.1306/06300504094.

1180 Frutos, J. (1981), Andean tectonics as a consequence of sea-floor spreading, Tectonophysics
1181 72, T21–T32.

1182 Fuller, C. W., S. D. Willett, and M. T. Brandon (2006), Formation of forearc basins and their
1183 influence on subduction zone earthquakes, Geology, 34, 65–68, doi:
1184 10.1130/G21828.1.

1185 Galbraith, R. F., and G. M. Laslett (1993), Statistical models for mixed fission track ages,
1186 Nuclear Tracks, 21, 459–470.

1187 Gallagher, K., R. Brown, and C. Johnson (1998), Fission track analysis and its applications to
1188 geological problems, Annual Review of Earth and Planetary Sciences, 26, 519–572,
1189 doi:10.1146/annurev.earth.26.1.519.

1190 Garreaud, R. D. (2009), The Andes climate and weather, Adv. Geosci., 22, 3–11.

1191 Gautheron C., N. Espurt, J. Barbarand, M. Roddaz, P. Baby, S. Brusset, L. Tassan-got, and E.
1192 Douville (2013), Direct dating of thick- and thin-skin thrusts in the Peruvian
1193 Subandean zone through apatite (U-Th)/He and fission track thermochronometry,
1194 Basin Research, 25, 1–17.

1195 Green, P. F., I. R. Duddy, G. M. Laslett, K. A. Hegarty, A. J. W. Gleadow, and J. F. Lovering
1196 (1989), Thermal annealing of fission tracks in apatite: Part 4. Quantitative modelling
1197 techniques and extension to geological timescales, Chemical Geology, 79, 155–182.

1198 Gripp, A. E., and R. G. Gordon (2002), Young tracks of hotspots and current plate velocities,
1199 Geophys. J. Int., 150, 321–361, doi:10.1046/j.1365-246X.2002.01627.x.

1200 Gutscher, M.-A., J. Malavieille, S. Lallemand, and J.-Y. Collot (1999a), Tectonic
1201 segmentation of the North Andean margin: impact of the Carnegie Ridge collision,
1202 Earth Planet.Sci. Lett., 168, 255–270.

1203 Gutscher, M.-A., J. L. Olivet, D. Aslanian, J. P. Eissen, and R. Maury (1999b), The ‘‘lost Inca
1204 Plateau’’: Cause of flat subduction beneath Peru?, Earth Planet. Sci. Lett., 171, 335–
1205 341, doi:10.1016/S0012-821X(99)00153-3.

1206 Gutscher, M.-A. (2002), Andean subduction styles and their effect on thermal structure and
1207 interplate coupling, J. South Am. Earth Sci., 15, 3–10, doi:10.1016/S0895-
1208 9811(02)00002-0.

1209 Hall, S. R., D. L. Farber, L. Audin, and R. C. Finkel, (2012), Recently active contractile
1210 deformation in the forearc of southern Peru, Earth and Planetary Science Letters, 337,
1211 85-92, doi:10.1016/j.epsl.2012.04.007.

1212 Haq, B. U., J. Hardenbol, and P. R. Vail (1987), Chronology of fluctuating sea levels since the
1213 Triassic, Science, 235, 1156–1167.

1214 Hasebe, N., J. Barbarand, K. Jarvis, A. Carter, and A. J. Hurford (2004), Apatite fission-track
1215 chronometry using laser ablation ICP-MS, Chemical Geology, 207, 135–145,
1216 doi:10.1016/j.chemgeo.2004.01.007.

1217 Hessler, A. M., and A. Fildani (2015), Andean forearc dynamics, as recorded by detrital
1218 zircon from the Eocene Talara Basin, northwest Peru, Journal of Sedimentary
1219 Research, 85, 6, 646–659, doi: 10 .2110 /jsr.2015 .45.

1220 Heuret, A., C. P. Conrad, F. Funiciello, S. Lallemand, and L. Sandri (2012), Relation between
1221 subduction megathrust earthquakes, trench sediment thickness and upper plate strain,
1222 Geophys. Res. Lett., 39, L05304, doi:10.1029/2011GL050712.

1223 Heuret, A., F. Funiciello, C. Faccenna, and S. Lallemand (2007), Plate kinematics, slab shape
1224 and back-arc stress: A comparison between laboratory models and current subduction
1225 zones, Earth Planet. Sci. Lett., 256, 473–483, doi:10.1016/j.epsl.2007.02.004.

1226 Higley, D. K. (2004), The Talara Basin Province of Northwestern Peru: Cretaceous-Tertiary
1227 Total Petroleum System. USGS Bulletin 2206-A, 20 p.

1228 Hoffmann-Rothe, A., N. Kukowski, G. Dresen, H. Echtler, O. Oncken, J. Klotz, E. Scheuber,
1229 and A., Kellner (2006), Oblique Convergence along the Chilean Margin: Partitioning,
1230 Margin-Parallel Faulting and Force Interaction at the Plate Interface, in The Andes:
1231 Active Subduction Orogeny, edited by O. Oncken et al., Chapter 6, 121–142, Springer,
1232 Berlin.

1233 Horton, B. K. (1999), Erosional control on the geometry and kinematics of thrust belt
1234 development in the central Andes, Tectonics, 18, 1292–1304,
1235 doi:10.1029/1999TC900051.

1236 Hyndman, R. D., K. Wang, and M. Yamano (1995), Thermal constraints on the seismogenic
1237 portion of the southwestern Japan subduction thrust, Journal of Geophysical Research,
1238 100, 15,373–15,392, doi: 10.1029/95JB00153.

1239 Iaffaldano, G., H.-P. Bunge, and T. H. Dixon (2006), Feedback between mountain belt growth
1240 and plate convergence, Geology, 34, 893–896, doi:10.1130/G22661.1.

1241 Ikari, M. J., D. M. Saffer, and C. Marone (2009), Frictional and hydrologic properties of a
1242 major splay fault system, Nankai subduction zone, Geophys. Res. Lett., 36, L20313.
1243 doi:10.1029/2009GL040009

1244 Jaillard, E., G. Laubacher, P. Bengtson, A. V. Dhondt, and L. G. Bulot (1999), Stratigraphy
1245 and evolution of the Cretaceous forearc Celica-Lancones basin of southwestern
1246 Ecuador, Journal of South American Earth Sciences, 12, 51–68.

1247 Jaillard, E., S. Benitez, and G. Mascle (1997), Les déformations paléogènes de la zone
1248 d'avant-arc sud-équatorienne en relation avec l'évolution géodynamique, Bulletin de
1249 la Société Géologique de France, 168, 403–412.

1250 Jaillard, E., and P. Soler (1996), Cretaceous to early Paleogene tectonic evolution of the
1251 northern Central Andes (0-18°S) and its relations to geodynamics, Tectonophysics,
1252 259, 41–53.

1253 Jaillard, E., M. Ordoñez, S. Benitez, G. Berrones, N. Jiménez, G. Montenegro, and I.
1254 Zambrano (1995), Basin development in an accretionary, oceanic-floored fore-arc
1255 setting: southern coastal Ecuador during Late Cretaceous–Late Eocene time, in A. J.
1256 Tankard, R. Suarez S., and H. J. Welsink, Petroleum Basins of South America,
1257 American Association of Petroleum Geologists Memoir, 62, 615–631.

1258 Jaillard, E., P. Soler, G. Carlier, and T. Mourier (1990), Geodynamic evolution of the northern
1259 and central Andes during early to middle Mesozoic times: A Tethyan model, Journal
1260 of Geological Society of London, 147, 1009–1022.

1261 Kastner, M., Y. Zheng, T. Laier, W. Jenkins, and T. Ito (1998), Geochemistry of fluids and
1262 flow regime in the decollement zone at the northern Barbados Ridge: Ocean Drilling
1263 Program, Scientific results, 156, 311–319.

1264 Ketcham, R. A. (2005), Forward and inverse modeling of low-temperature
1265 thermochronometry data, in Reiners, P.W., and Ehlers, T.A., eds., Lowtemperature
1266 thermochronology: Techniques, interpretations, and applications, Mineralogical
1267 Society of America Reviews in Mineralogy and Geochemistry, 58, 275–314.

1268 Laj, C., P., Mitouard, P., Roperch, C., Kissel, T., Mourier, and F., Mégard (1989),
1269 Paleomagnetic Rotations in the Coastal Areas of Ecuador and Northern Peru. In:
1270 Kissel C., Laj C. (eds) Paleomagnetic Rotations and Continental Deformation. NATO
1271 ASI Series (C: Mathematical and Physical Sciences), Springer, Dordrecht, 254, 489–
1272 511, doi: 10.1007/978-94-009-0869-7_29.

1273 Lallemand, S. E., P. Schnürle, and J. Malavieille (1994), Coulomb theory applied to
1274 accretionary and nonaccretionary wedges: Possible causes for tectonic erosion and/or
1275 frontal accretion, Journal of Geophysical Research, 99, B6, 12,033–12,055, doi:
1276 10.1029/94JB00124.

1277 Laursen, J., D. W. Scholl, and R. Von Huene (2002), Neotectonic deformation of the central
1278 Chile margin: Deepwater forearc basin formation in response to hot spot ridge and
1279 seamount subduction, Tectonics, 21(5), 1038, doi:10.1029/2001TC901023.

1280 Lebras, M., F. Mégard, C. Dupuy, and J. Dostal (1987), Geochemistry and tectonic setting of
1281 pre-collision Cretaceous and Paleogene volcanic rocks of Ecuador, Geological Society
1282 of America Bulletin, 99, 569–578.

1283 Le Pichon, X., P. Henry, and S. Lallemant (1993), Accretion and erosion in subduction zones:
1284 The role of fluids, Annual Review of Earth and Planetary Sciences, 21, 1, 307–331,
1285 doi: 10 .1146 /annurev .ea .21 .050193.001515

1286 Lonsdale, P. (2005), Creation of the Cocos and Nazca plates by fission of the Farallon plate,
1287 Tectonophysics, 404, 237– 264.

1288 Lonsdale, P., and K. D. Klitgord (1978), Structure and tectonic history of the eastern Panama
1289 Basin, Geol. Soc. Am. Bull., 89, 981–999, doi:10.1130/0016-
1290 7606(1978)89<981:SATHOT>2.0.CO;2.

1291 López, E., Collot, J.-Y., and M. Sosson (2008), Sedimentary constraints on the tectonic
1292 evolution of the paired Tumaco–Borbón and Manglares forearc basins (southern
1293 Colombia-northern Ecuador) during the Late Cenozoic, 7th International Symposium
1294 on Andean Geodynamics (ISAG 2008, Nice), Extended Abstracts, 292–294.

1295 Macharé, J., and L., Ortlieb (1994), Morfoestratigrafia de los Tablazos del Noroeste peruano:
1296 neotectonica y fluctuaciones del nivel del mar, Resumenes Extendidos del VIII
1297 Congreso Peruano, 238–241.

1298 Mannu, U., K. Ueda, S. D. Willett, T. V. Gerya, and M. Strasser (2017), Stratigraphic
1299 signatures of forearc basin formation mechanisms, Geochem. Geophys. Geosyst., 18,
1300 doi:10.1002/2017GC006810.

1301 Marrett, R., and M. R. Strecker (2000), Response of intracontinental deformation in the
1302 central Andes to late Cenozoic reorganization of South American plate motions,
1303 Tectonics, 19, 452–467, doi:10.1029/1999TC001102.

1304 Martinod, J., V. Regard, Y. Letourmy, H. Henry, R. Hassani, S. Baratchart, and S. Carretier
1305 (2016), How do subduction processes contribute to forearc Andean uplift? Insights
1306 from numerical models, Journal of Geodynamics, 96, 6–18.

1307 Martinod, J., L. Husson, P. Roperch, B. Guillaume, and N. Espurt (2010), Horizontal sub-
1308 duction zones, convergence velocity and the building of the Andes, Earth Planet.Sci.
1309 Lett., 299, 299–309.

1310 Mauduit, T., and J. P. Brun (1998), Growth fault/rollover systems: Birth, growth, and decay,
1311 J. Geophys. Res., 103, 18,119–18,136, doi:10.1029/97JB02484.

1312 McClay, K.R. (1990), Extensional fault systems in sedimentary basins: a review of analogue
1313 model studies, Marine and Petroleum Geology, 7, 206–233.

1314 Mc Neill, L. C., C. Goldfinger, L. D. Kulm, and R. S. Yeats (2000), Tectonics of the Neogene
1315 Cascadia forearc basin: Investigations of a deformed late Miocene unconformity,
1316 Geological Society of America Bulletin, 112, 1209–1224.

1317 Melnick, D., B. Bookhagen, H. P. Echtler, and M. R. Strecker (2006), Coastal deformation
1318 and great subduction earthquakes, Isla Santa María, Chile (37°S), Geological Society
1319 of America Bulletin, 118, 1463–1480; doi: 10.1130/B25865.1.

1320 Michaud, F, C. Witt, and J.-Y. Royer (2009), Influence of the subduction of the Carnegie
1321 volcanic ridge on Ecuadorian geology: Reality and fiction, in Kay, S. M., Ramos, V.
1322 A., and Dickinson, W. R., eds., Backbone of the Americas: Shallow Subduction,
1323 Plateau Uplift, and Ridge and Terrane Collision, Geological Society of America
1324 Memoir, 204, 217–228, doi: 10.1130/2009.1204(10).

1325 Mitouard, P., C. Kissel, and C. Laj (1990), Post-Oligocene rotations in southern Ecuador and
1326 northern Peru and the formation of the Huancabamba Deflection in the Andean
1327 Cordillera, Earth Planet. Sci. Lett., 98, 329–339.

1328 Moberly, R., G. L. Shepherd, and W. T. Coulbourn (1982), Forearc and other basins,
1329 continental margin of northern and southern Peru and adjacent Ecuador and Chile,
1330 Geological Society, London, Special Publications, 10, 171–189,
1331 doi:10.1144/GSL.SP.1982.010.01.11.

Moore, G. F., B. B. Boston, M. Strasser, M. B. Underwood, and R. A. Ratliff (2015), Evolution of tectono-sedimentary systems in the Kumano Basin, Nankai Trough forearc, Marine and Petroleum Geology, 67, 604–616.

Mora-Bohórquez, J. A., M. Ibánez-Mejia, O. Oncken, M. de Freitas, V. Vélez, A. Mesa, L. Serna (2017), Structure and age of the Lower Magdalena Valley basin basement, northern Colombia: New reflection-seismic and U-Pb-Hf insights into the termination of the central Andes against the Caribbean basin, Journal of South American Earth Sciences, 74, 1–26, doi:10.1016/j.jsames.2017.01.001

Mourier, T., C. Laj, F. Mégard, P. Roperch, P. Mitouard, and A. F. Medrano (1988), An accreted continental terrane in northwestern Peru, Earth and Planetary Science Letters, 88(1–2), 182–192, doi: 10 .1016 /0012-821X (88)90056 -8.

Mukti, M. M., S. C. Singh, I. Deighton, N. D. Hananto, R. Moeremans, and H. Permana (2012), Structural evolution of backthrusting in the Mentawai Fault Zone, offshore Sumatran forearc, Geochem. Geophys. Geosyst., 13, Q12006, doi:10.1029/2012GC004199.

Naeser, C. W., J.-Y. Crochet, E. Jaillard, G. Laubacher, T. Mourier, and B. Sigé (1991), Tertiary fission-track ages from the Bagua syncline (northern Peru): Stratigraphic and tectonic implications, Journal of South American Earth Sciences, 4(1/2), 61–71.

Namiki, Y., A. Tsutsumi, K. Ujiie, and J. Kameda (2014), Frictional properties of sediments entering the Costa Rica subduction zone offshore the Osa Peninsula: implications for fault slip in shallow subduction zones, Earth, Planets and Space, 66, 72, doi: 10.1186/1880-5981-66-72.

Noble, D. C., E. H. McKee, T. Mourier, and F. Mégard (1990), Cenozoic stratigraphy, magmatic activity, compressive deformation, and uplift in northern Peru, Bulletin of the Geological Society of America, 102 (8), 1105–1113.

Nocquet, J.-M., et al. (2014), Motion of continental slivers and creeping subduction in the northern Andes, Nat. Geosci., 7, 287–291, doi:10.1038/NGEO2099.

Noda, A., and A. Miyakawa (2017), Deposition and Deformation of Modern Accretionary-Type Forearc Basins: Linking Basin Formation and Accretionary Wedge Growth, Evolutionary Models of Convergent Margins - Origin of Their Diversity, Dr. Yasuto Itoh (Ed.), InTech, doi: 10.5772/67559.

Noda, A. (2016), Forearc basins: Types, geometries, and relationships to subduction zone dynamics, GSA Bulletin, 128(5/6), 879–895; doi: 10.1130/B31345.1.

Nunns, A. (1991), Structural restoration of seismic and geologic sections in extensional regimes, The American Association of Petroleum Geologists Bulletin, 75, 278–297.

Parra, M., A. Mora, C. Lopez, L. E. Rojas, and B. K. Horton (2012), Detecting earliest shortening and deformation advance in thrust belt hinterlands: Example from the Colombian Andes, Geology, 40, 175–178, doi:10.1130/G32519.1.

Pecora, L., E. Jaillard, and H. Lapierre (1999), Accrétion paléogène et décrochement dextre d'un terrain océanique dans le Nord du Pérou, Comptes Rendus de l'Académie des Sciences - Series IIA - Earth and Planetary Science, 329, 389–396.

Pedoja, K., L. Ortlieb, J. F. Dumont, M. Lamothe, B. Ghaleb, M. Auclair, and B. Labrousse (2006), Quaternary coastal uplift along the Talara Arc (Ecuador, northern Peru) from new marine terrace data, Marine Geology, 228, 73–91.

Pozo, G. (2002), Bioestratigrafia de alta resolucion y su aplicación en la identificacion de secuencias cronoestratigraficas de tercer orden en el Paleogeno del lote X–Cuenca Talara - Peru, XI Sociedad Geologica del Peru, Congreso Peruano de Geologia, 12, 2002.

Quispe Alcalá, D. R. (2010), Evaluación geológica de la formación Mogollón en el yacimiento Leones, cuenca Talara-Perú, Tesis Ing. Geol., Facultad de Ingeniería Geológica Minera y Metalurgica, Lima, 87 p.

Ramos, V. A. (2009), Anatomy and global context of the Andes: Main geologic features and the Andean orogenic cycle, in Kay, S.M., Ramos, V.A., and Dickinson, W.R., eds., Backbone of the Americas: Shallow Subduction, Plateau Uplift, and Ridge and Terrain Collision, Geological Society of America Memoir, 204, 31–65, doi: 10 .1130 /2009 .1204 (02) .

Regalla, C., D. M. Fisher, E. Kirby, and K. P. Furlong (2013), Relationship between outer forearc subsidence and plate boundary kinematics along the Northeast Japan convergent margin, Geochem. Geophys. Geosyst., 14, 5227–5243, doi:10.1002/2013GC005008.

Riel, N., J.-E. Martelat, S. Guillot, E. Jaillard, P. Monié, J. Yuquilema, G. Duclaux, and J. Mercier (2014), Fore arc tectonothermal evolution of the El Oro metamorphic province (Ecuador) during the Mesozoic, Tectonics, 33, doi:10.1002/2014TC003618.

Roddaz, M., W. Hermoza, A. Mora, P. Baby, M. Parra, F. Christophoul, S. Brusset, and N. Espurt (2010), Cenozoic sedimentary evolution of the Amazonian foreland basin system, in Hoorn, C., and Wesselingh, F.P., eds., Amazonia, Landscape and Species Evolution: Blackwell Publishing, 61–88.

Royden, L. H. (1993), Evolution of retreating subduction boundaries formed during continental collision, Tectonics, 12, 629–638, doi: 10.1029/92TC02641.

Romero, D., K. Valencia, P. Alarcón, D. Peña, and V. A. Ramos (2013), The offshore basement of Perú: Evidence for different igneous and metamorphic domains in the forearc, Journal of South American Earth Sciences, 42, 47–60.

Sage, F., J.-Y. Collot, and C. R. Ranero (2006), Interplate patchiness and subduction- erosion mechanisms: evidence from depth-migrated seismic images at the Central Ecuador convergent margin, Geology, 34, 997–1000.

Saillard, M., L. Audin, B. Rousset, J.-P. Avouac, M. Chlieh, S. R. Hall, L. Husson, and D. L. Farber (2017), From the seismic cycle to long-term deformation: linking seismic coupling and Quaternary coastal geomorphology along the Andean megathrust, Tectonics, 36, 241–256, doi:10.1002/2016TC004156.

Saillard, M., S. R. Hall, L. Audin, D. L. Farber, V. Regard, and G. Hérail (2011), Andean coastal uplift and active tectonics in southern Peru: 10Be surface exposure dating of differentially uplifted marine terrace sequences (San Juan de Marcona, ~15.4°S), Geomorphology, 128(3), 178–190, doi:10.1016/j.geomorph.2011.01.004.

Salomons, W, H. H. Kremer, and R. K. Turner (2005), The catchment to coast continuum. In: Coastal fluxes in the Anthropocene. Global Change, IGBP Series. Springer Verlag, Berlin, 145–198.

Sánchez, J., B. K. Horton, E. Tesón, A. Mora, R. A. Ketcham, and D. F. Stockli (2012), Kinematic evolution of Andean fold-thrust structures along the boundary between the

Eastern Cordillera and Middle Magdalena Valley basin, Colombia, Tectonics, 31, TC3008, doi:10.1029/2011TC003089.

Sánchez, J., O. Palacios, T. Feininger, V. Carlotto, and L. Quispesivana (2006) Puesta en evidencia de granitoides triasicos en los Amotapes-Tahuin: Deflexion de Huancabamba. XIII Congreso Peruano de Geologia, Resumenes Extendidos, Sociedad Geologica del Peru, 312–315. (Extended Abstract, non reviewed, in Spanish).

Saura, E., J. Vergés, D. Brown, P. Lukito, S. Soriano, S. Torrescusa, R. Garcia, J. R. Sanchez, C. Sosa, and R. Tenreyro (2008), Structural and tectonic evolution of western Cuba fold and thrust belt, Tectonics, 27, TC4002, doi:10.1029/2007TC002237.

Schurr, B., G. Asch, M. Rosenau, R. Wang, O. Oncken, S. Barrientos, P. Salazar, and J. P. Vilotte (2012), The 2007 M7.7 Tocopilla northern Chile earthquake sequence: Implications for along-strike and downdip rupture segmentation and megathrust frictional behavior, J. Geophys. Res., 117, B05305, doi:10.1029/2011JB009030.

Schütte, P., M. Chiaradia, and B. Beate (2010), Geodynamic controls on Tertiary arc magmatism in Ecuador: Constraints from U–Pb zircon geochronology of Oligocene–Miocene intrusions and regional age distribution trends, Tectonophysics, 489, 159–176.

Sdrolias, M., and R. D. Müller (2006), Controls on back-arc basin formation, Geochem. Geophys. Geosyst., 7, Q04016, doi:10.1029/2005GC001090.

Séranne, M. (1987), Evolution tectono-sédimentaire du bassin de Talara (nord-ouest du Pérou), Bull. Inst. Fr. Et. And., XVI, 3-4, 103–125.

Shaw, J., C. Connors, and J. Suppe (2005), Seismic interpretation of contractional fault-related folds: An American Association of Petroleum Geologists Seismic Atlas: Tulsa, Oklahoma, American Association of Petroleum Geologists, Studies in Geology, 53, 156 p.

Shepherd, G. L., and R. Moberly (1981), Coastal structure of the continental margin, NW Peru and SW Ecuador, Geol. Soc. Am. Mem., 154, 351–391

Shiki, T., and Y. Misawa (1982), Forearc geologic structure of the Japanese Islands. Trench-Forearc Geology: Sedimentation and Tectonics on Modern and Ancient Active Plate Margins, K. Leggett ed., Geological Society Special Publication, London, 10, 63–73.

Simpson, D. G. H. (2010), Formation of accretionary prisms infl uenced by sediment subduction and supplied by sediments from adjacent continents, Geology, 38, 131–134; doi: 10.1130/G30461.1

Skinner, S. M., and R. W. Clayton (2013), The lack of correlation between flat slabs and bathymetric impactors in South America, Earth and Planetary Science Letters, 371–372, 1–5.

Somoza, R., and M. E., Ghidella (2012), Late Cretaceous to recent plate motions in western South America revisited, Earth and Planetary Science Letters, 331, 152–163.

Spikings, R., M. J. Reitsma, F. Boekhout, A. Mišković, A.Ulianov, M. Chiaradia, A. Gerdes, and U. Schaltegger (2016), Characterisation of Triassic rifting in Peru and implications for the early disassembly of western Pangaea, Gondwana Research, 35, 124–143.

Spikings, R. A., P. V. Crowhurst, W. Winkler, and D. Villagomez (2010), Syn- and post-accretionary cooling history of the Ecuadorian Andes constrained by their in-situ and

1464 detrital thermochronometric record, Journal of South American Earth Sciences, 30,
1465 121–133.

1466 Spikings, R. A., W. Winkler, R. A. Hughes, and R. Handler (2005), Thermochronology of
1467 allochthonous terranes in Ecuador: unravelling the accretionary and post-accretionary
1468 history of the Northern Andes, Tectonophysics, 399, 195–220.

1469 Shepherd, G. L., and R. Moberly (1981), Coastal structure of the continental margin
1470 northwest Peru and southwest Ecuador, in Kulm, L.D., et al., eds., Nazca Plate:
1471 Crustal Formation and Andean Convergence, Geological Society of America Memoir,
1472 154, 351–391.

1473 Suppe, J. (1983), Geometry and kinematics of fault-bend folding, Am. J. Sci., 283, 684–721.

1474 Suppe, J., and D. A. Medwedeff (1990), Geometry and kinematics of fault-propagation
1475 folding, Eclogae Geol. Helv., 83(3), 409–454.

1476 Takahashi, M, S., Azuma, S. Uehara, K. Kanagawa, and A. Inoue (2013), Contrasting
1477 hydrological and mechanical properties of clayey and silty muds cored from the
1478 shallow Nankai Trough accretionary prism, Tectonophysics, 600, 63–74,
1479 doi.org/10.1016/j.tecto.2013.01.008

1480 Takano, O., Y. Itoh, and S. Kusumoto (2013), Variation in forearc basin configuration and
1481 basin-filling depositional systems as a function of trench slope break development and
1482 strike-slip movement: examples from the Cenozoic Ishikari− Sanriku-Oki and Tokai-
1483 Oki− Kumano-Nada forearc basins, Japan: Mechanism of sedimentary basin
1484 formation-multidisciplinary approach on active plate margins. InTech, Rijeka
1485 (Croatia), http://dx. doi. org/10.5772/56751

1486 Totake, Y., R. W. H. Butler, C. E. Bond (2017), Structural validation as an input into seismic
1487 depth conversion to decrease assigned structural uncertainty, Journal of structural
1488 geology, 95, 32–47, doi: 10.1016/j.jsg.2016.12.007

1489 Travis, R. B., G. Gonzales, and A. Pardo (1976), Hydrocarbon potential of coastal basins of
1490 Peru. In: M.T. Halbouty, J.C. Maher and H.M. Lian (Editors), Circum Pacific Energy
1491 and Mineral resources, The American Association Petroleum Geologist Memory, 25,
1492 331–338.

1493 Tsuji, T., J. Ashi, M. Strasser, and G. Kimura (2015), Identification of the static backstop and
1494 its influence on the evolution of the accretionary prism in the Nankai Trough, Earth
1495 and Planetary Science Letters, 431, 15–25.

1496 Valencia, K., and D. Uyen (2002), Cuenca Lancones: Interpretation geologica. INGEPET,
1497 EXPR-3-KV-18. (Extended Abstract, non peer reviewed, in Spanish).

1498 Vega, M. (2009), Architecture tectonique et stratigraphique du bassin d'avant-arc de Tumbes
1499 (Nord Pérou) : implications pour l'exploration des hydrocarbures, University of
1500 Toulouse III-Paul Sabatier. Ph.d. thesis, 191 p.

1501 Vermeesch, P. (2009), RadialPlotter: A Java application for fission track, luminescence and
1502 other radial plots, Radiation Measurements, 44, 409–410,
1503 doi:10.1016/j.radmeas.2009.05.003.

1504 Villegas-Lanza, J. C., M. Chlieh, O. Cavalié, H. Tavera, P. Baby, J. Chire-Chira, and J.-M.
1505 Nocquet (2016), Active tectonics of Peru: Heterogeneous interseismic coupling along
1506 the Nazca megathrust, rigid motion of the Peruvian Sliver, and Subandean shortening
1507 accommodation, J. Geophys. Res. Solid Earth, 121, doi:10.1002/2016JB013080.

1508 Von Huene, R., and S. Lallemand (1990), Tectonic erosion along the Japan and Peru
1509 convergent margins, Geological Society of America Bulletin, 102(6), 704–72.

1510 Von Huene, R., Ranero, C. R., and P. Vannucchi (2004), Generic model of subduction
1511 erosion, Geology, 32(10), 913–916, doi: 10.1130/G20563.1.

1512 Wallace, W. K. (2008), Yakataga fold-and-thrust belt: Structural geometry and tectonic
1513 implications of a small continental collision zone, in Active Tectonics and Seismic
1514 Potential of Alaska, edited by J.T. Freymueller et al., 237–256, AGU, Washington, D.
1515 C., doi:10.1029/179GM13.0.

1516 Winter, L. S., R. M. Tosdal, J. K. Mortensen, and J. M. Franklin (2010), Volcanic stratigraphy
1517 and geochronology of the Cretaceous Lancones Basin, northwestern Peru: Position
1518 and timing of giant VMS deposits, Economic Geology, 105(4), 713–742, doi:
1519 10.2113/gsecongeo.105.4.713.

1520 Wipf, M. A. (2006), Evolution of the Western Cordillera and Coastal Margin of Peru:
1521 Evidence from Low-Temperature Thermochronology and Geomorphology
1522 [Ph.D.Dissertation]: Zürich, Naturwissenschaften, Eidgenössische Technische
1523 Hochschule ETH Zürich, Dissertation 16383, 152 p.

1524 Witt, C., M. Rivadeneira, M. Poujol, D. Barba, D. Beida, G. Beseme, and G. Montenegro
1525 (2017), Tracking ancient magmatism and Cenozoic topographic growth within the
1526 Northern Andes forearc: Constraints from detrital U-Pb zircon ages, Geological
1527 Society of America Bulletin, 129 (3-4), 415–428, doi: 10.1130/B31530.1.

1528 Witt, C., and J. Bourgois (2010), Forearc basin formation in the tectonic wake of a collision-
1529 driven, coastwise migrating crustal block: The example of the North Andean block
1530 and the extensional Gulf of Guayaquil–Tumbes Basin (Ecuador-Peru border area),
1531 Geological Society of America Bulletin, 122(1–2), 89–108, doi: 10.1130 /B26386 .1.

1532 Witt, C., J. Bourgois, F. Michaud, M. Ordoñez, N. Jiménez, and M. Sosson (2006),
1533 Development of the Gulf of Guayaquil (Ecuador) during the Quaternary as an effect of
1534 the North Andean block tectonic escape, Tectonics, 25(3), TC3017, doi: 10 .1029
1535 /2004TC001723.

1536 Zhao, W.-L., D. M. Davis, F. A. Dahlen, and J. Suppe (1986), Origin of convex accretionary
1537 wedges: Evidence from Barbados, Journal of Geophysical Research, 91, 10,246–
1538 10,258.

1539 Zhou, J., F. Xu, T. Wang, A. Coa, and C. Yin (2006), Cenozoic deformation history of the
1540 Qaidam Basin, NW China: Results from cross-section restoration and implications for
1541 Qinghai–Tibet Plateau tectonics, Earth and Planetary Science Letters, 243, 195–210,
1542 doi:10.1016/j.epsl.2005.11.033.

Figure 1.

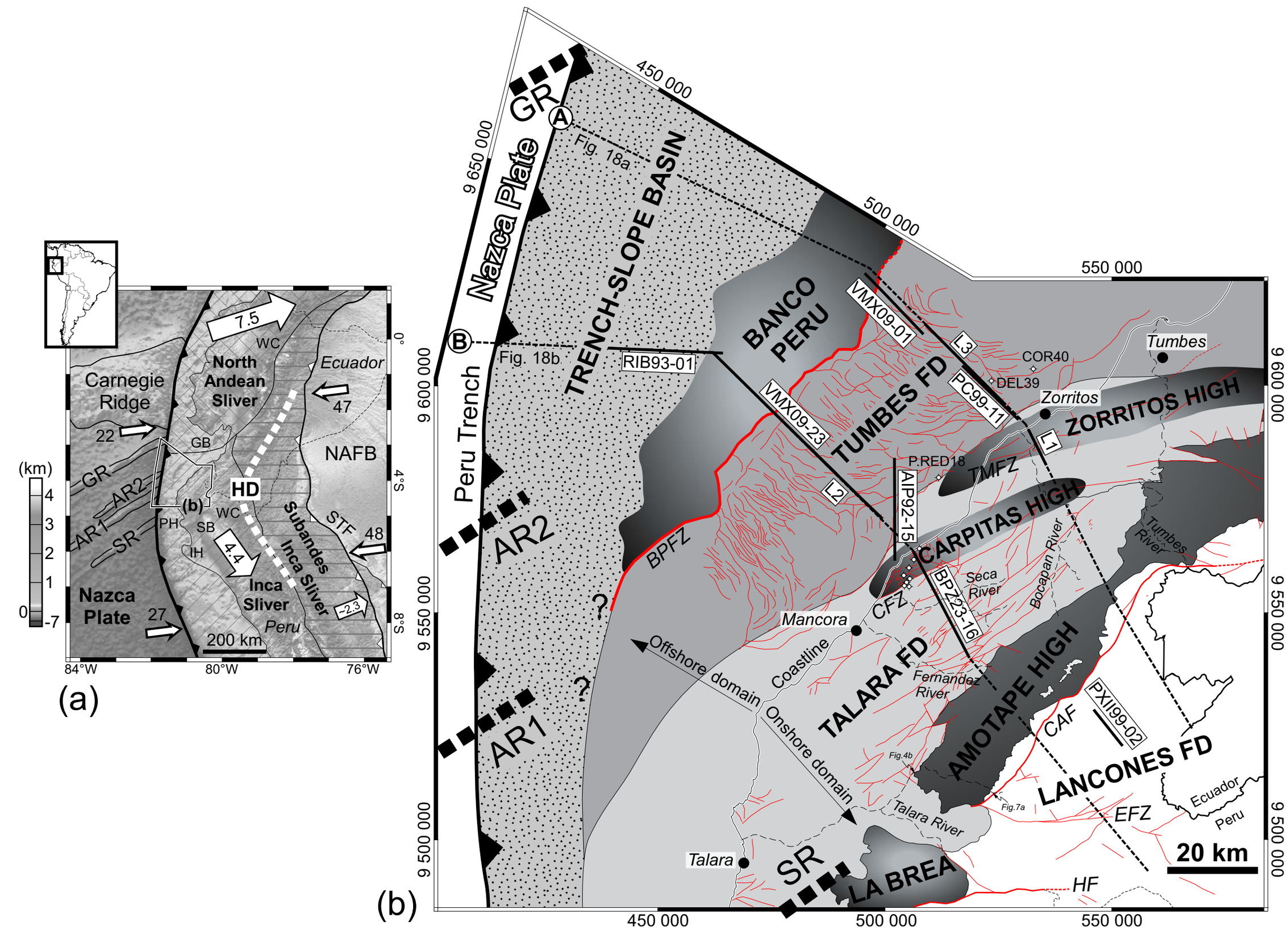
(a)
7.5
WC
North Andean Sliver
Ecuador
Carnegie Ridge
22
GB
47
NAFB
GR
AR2
AR1
SR
HD
(b)
PH
SB
WC
IH
Subandes
Inca Sliver
STF
48
4.4
Inca Sliver
Peru
Nazca Plate
27
-2.3
200 km
(km)
4
3
2
1
0
-7
84°W
80°W
76°W
0°
4°S
8°S
(b)
Nazca Plate
GR
A
Fig. 18a
9 650 000
450 000
500 000
550 000
TRENCH-SLOPE BASIN
B
Fig. 18b
RIB93-01
Peru Trench
BANCO PERU
VMX09-01
L3
COR40
DEL39
PC99-11
Tumbes
Zorritos
ZORRITOS HIGH
TUMBES FD
VMX09-23
L1
L2
P.RED18
AIP92-15
TMFZ
CARPITAS HIGH
BPFZ
AR2
AR1
SR
?
Tumbes River
Seca River
Bocapan River
BPZ23-16
CFZ
Mancora
Offshore domain
Coastline
Onshore domain
TALARA FD
Fernandez River
AMOTAPE HIGH
CAF
PXI99-02
Fig.4b
LANCONES FD
Fig.7a
EFZ
Ecuador
Peru
Talara River
Talara
LA BREA
HF
20 km
9 600 000
9 550 000
9 500 000

Figure 2.

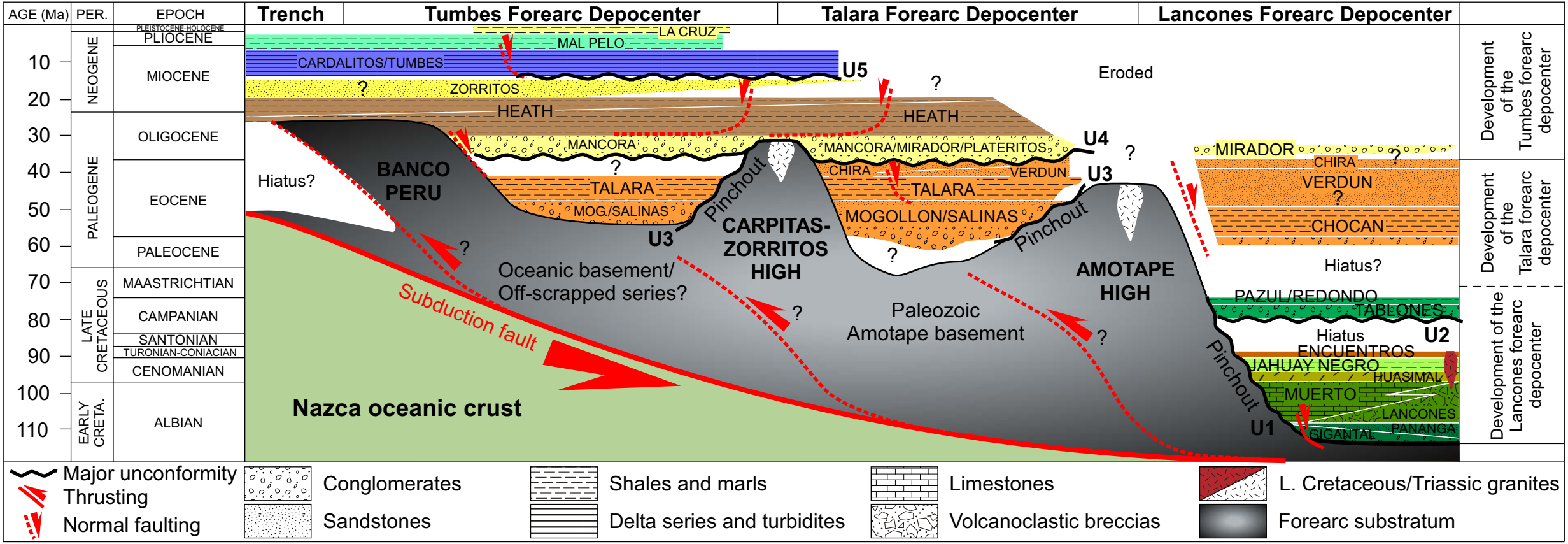
AGE (Ma)
PER.
EPOCH
Trench
Tumbes Forearc Depocenter
Talara Forearc Depocenter
Lancones Forearc Depocenter
PLEISTOCENE-HOLOCENE
PLIOCENE
MIOCENE
OLIGOCENE
EOCENE
PALEOCENE
MAASTRICHTIAN
CAMPANIAN
SANTONIAN
TURONIAN-CONIACIAN
CENOMANIAN
ALBIAN
NEOGENE
PALEOGENE
LATE CRETACEOUS
EARLY CRETA.
10
20
30
40
50
60
70
80
90
100
110
LA CRUZ
MAL PELO
CARDALITOS/TUMBES
ZORRITOS
HEATH
MANCORA
TALARA
MOG./SALINAS
U5
U4
U3
U2
U1
Eroded
MANCORA/MIRADOR/PLATERITOS
CHIRA
VERDUN
MOGOLLON/SALINAS
MIRADOR
CHOCAN
PAZUL/REDONDO
TABLONES
ENCUENTROS
JAHUAY NEGRO
HUASIMAL
MUERTO
LANCONES
PANANGA
GIGANTAL
Hiatus?
Hiatus
BANCO PERU
CARPITAS-ZORRITOS HIGH
AMOTAPE HIGH
Pinchout
Oceanic basement/
Off-scrapped series?
Paleozoic
Amotape basement
Subduction fault
Nazca oceanic crust
Development of the Tumbes forearc depocenter
Development of the Talara forearc depocenter
Development of the Lancones forearc depocenter
Major unconformity
Thrusting
Normal faulting
Conglomerates
Sandstones
Shales and marls
Delta series and turbidites
Limestones
Volcanoclastic breccias
L. Cretaceous/Triassic granites
Forearc substratum

Figure 3.

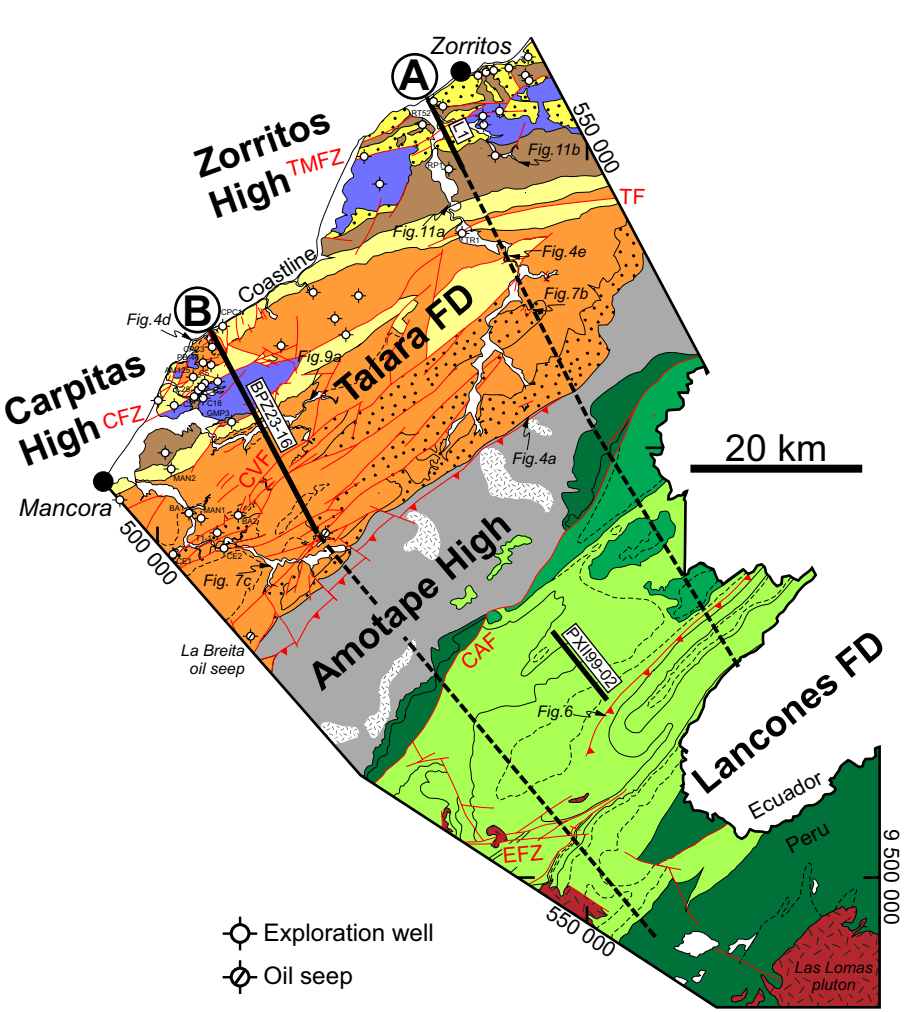
Zorritos
A
Zorritos High
TMFZ
550 000
L1
Fig.11b
TF
Fig.11a
Fig.4e
Coastline
Fig.7b
Fig.4d
B
Talara FD
Fig.9a
Carpitas High
CFZ
BP123-16
20 km
CVF
Fig.4a
Mancora
500 000
Fig. 7c
Amotape High
La Breita oil seep
CAF
PXI199-02
Fig.6
Lancones FD
Ecuador
Peru
9 500 000
EFZ
550 000
Las Lomas pluton
Exploration well
Oil seep
Alluvial (Quaternary)
Cardalitos (Middle Miocene)
Zorritos (Early Miocene)
Heath (L. Olig.-Early Miocene)
Mir./Plat./Mancora (L. Eoc.-E. Olig.)
Talara/Verdun/Chira (Mid.-L. Eoc.)
Mogollon-Salinas (Early Eocene)
Redondo/Tablones
Encuentros
Jahuay Negro
Huasimal
Intrusive
Late Cretaceous
Muerto/Lancones
Pananga/Gigantal
Early Cretaceous
Granite (Triassic)
Amotape basement (Paleozoic)

Figure 4.

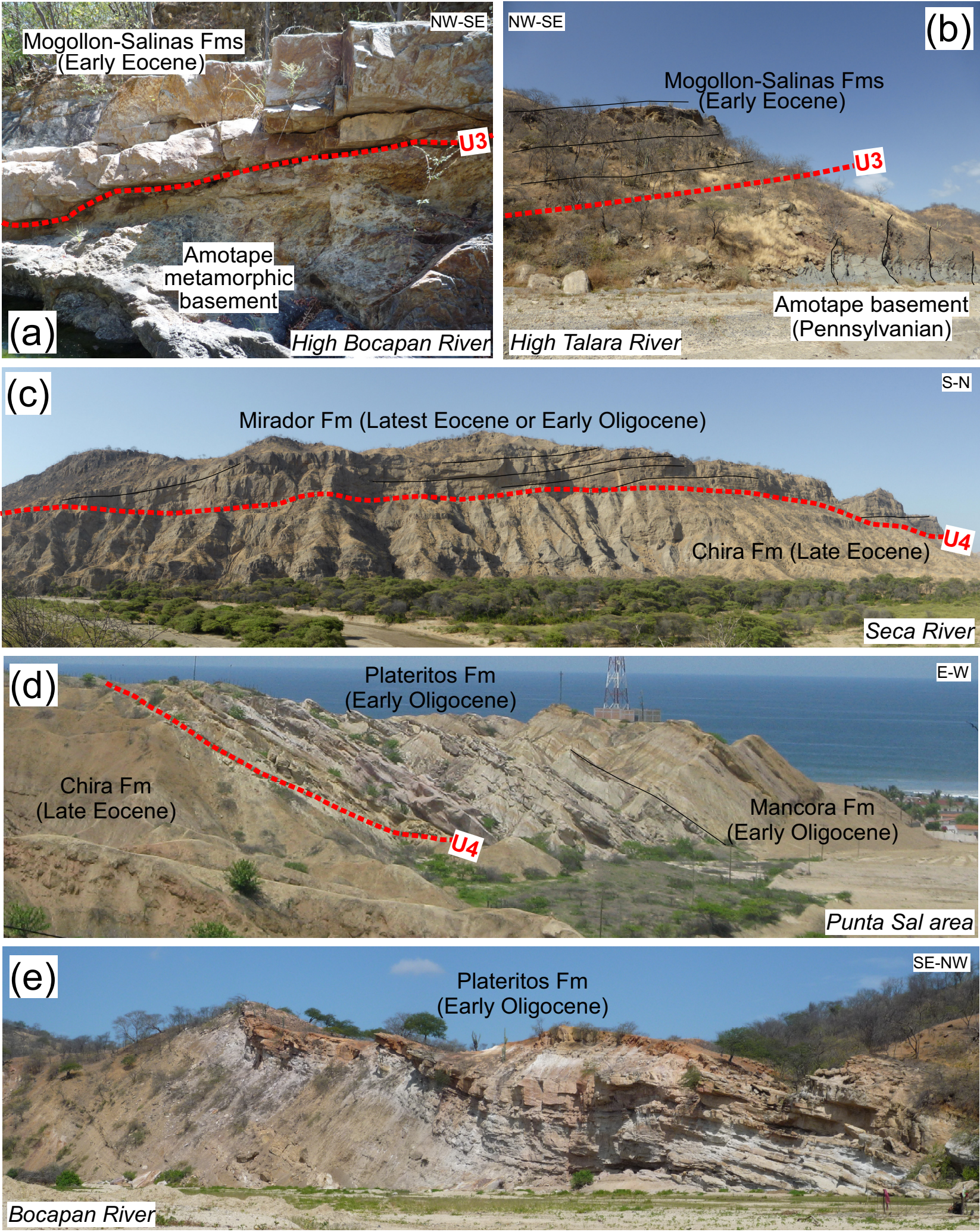
NW-SE
Mogollon-Salinas Fms
(Early Eocene)
U3
Amotape
metamorphic
basement
(a)
High Bocapan River
NW-SE
(b)
Mogollon-Salinas Fms
(Early Eocene)
U3
Amotape basement
(Pennsylvanian)
High Talara River
(c)
S-N
Mirador Fm (Latest Eocene or Early Oligocene)
Chira Fm (Late Eocene)
U4
Seca River
(d)
Plateritos Fm
(Early Oligocene)
E-W
Chira Fm
(Late Eocene)
U4
Mancora Fm
(Early Oligocene)
Punta Sal area
(e)
SE-NW
Plateritos Fm
(Early Oligocene)
Bocapan River

Figure 5.

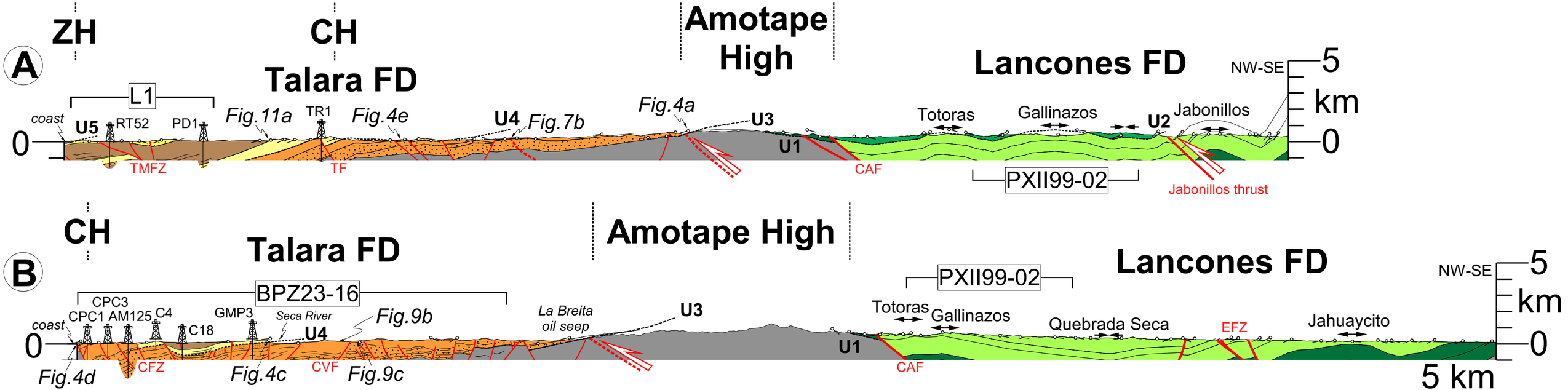
A
ZH
CH
Talara FD
Amotape High
Lancones FD
NW-SE
5
km
0
L1
coast
U5
RT52
PD1
Fig.11a
TR1
Fig.4e
U4
Fig.7b
Fig.4a
U3
U1
Totoras
Gallinazos
U2
Jabonillos
TMFZ
TF
CAF
PXII99-02
Jabonillos thrust
B
CH
Talara FD
Amotape High
Lancones FD
BPZ23-16
PXII99-02
CPC3
CPC1
AM125
C4
C18
GMP3
Seca River
U4
Fig.9b
La Breita
oil seep
U3
U1
Totoras
Gallinazos
Quebrada Seca
EFZ
Jahuaycito
NW-SE
5
km
0
coast
Fig.4d
CFZ
Fig.4c
CVF
Fig.9c
CAF
5 km
Cardalitos
(Mid. Miocene)
Heath
(L. Olig.-E. Mio.)
Tal./Verd./Chira
(Mid.-L. Eocene)
Redon./Tablones
(Late Cretaceous)
Muerto/Lancones/
Pananga/Lancones
(Early Cretaceous)
Amotape basement/Granite
(Paleoz.-Triassic)
Zorritos
(Early Miocene)
Mir./Plat./Man.
(L. Eoc.-E. Olig.)
Mog./Salinas
(Early Eocene)
Hua./J.Negro/Enc.
(Late Cretaceous)

Figure 6.

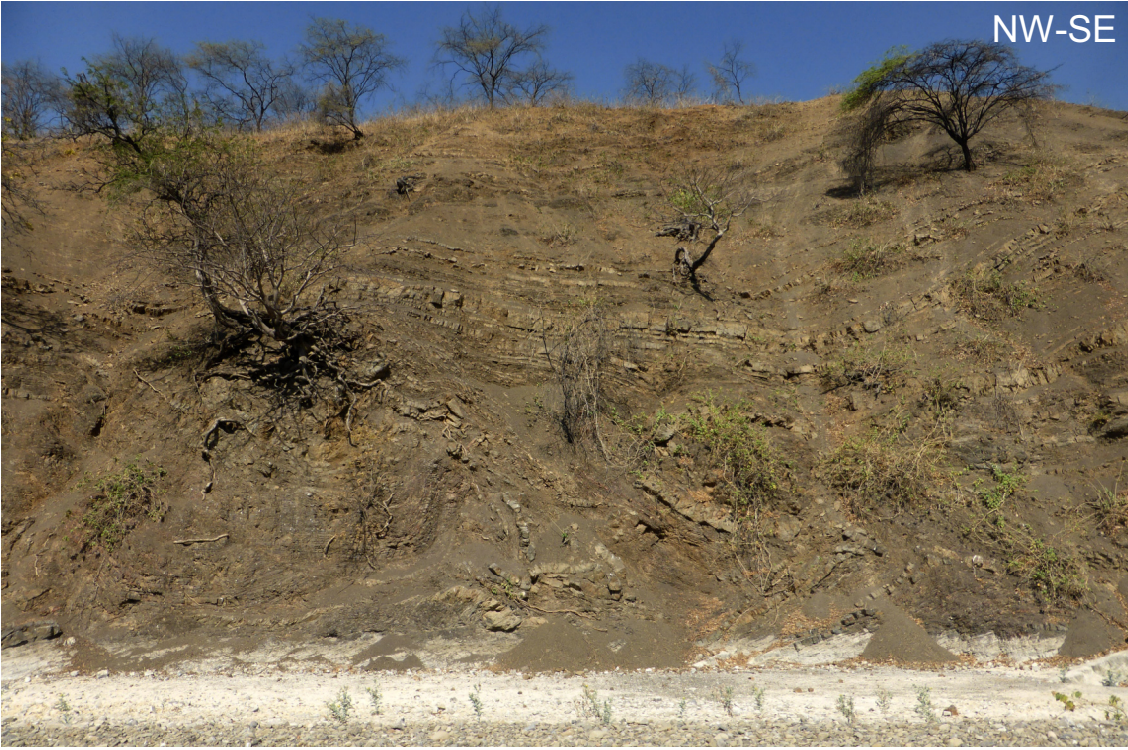
NW-SE

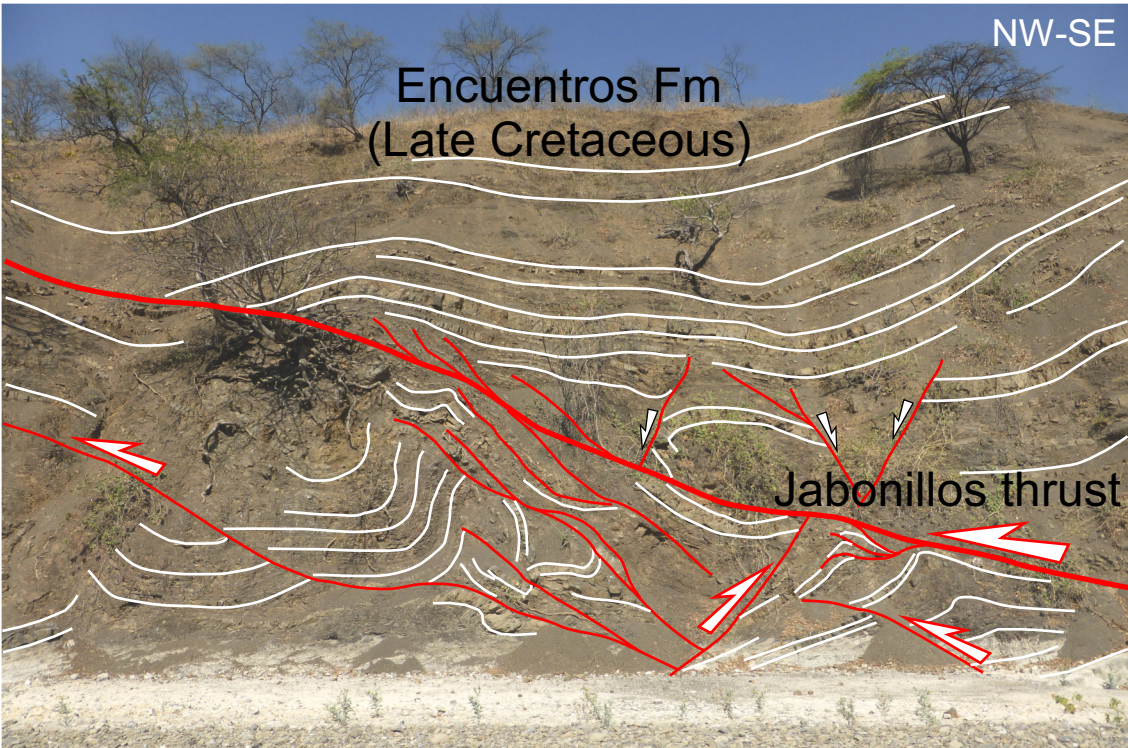
NW-SE
Encuentros Fm
(Late Cretaceous)
Jabonillos thrust

Figure 7.

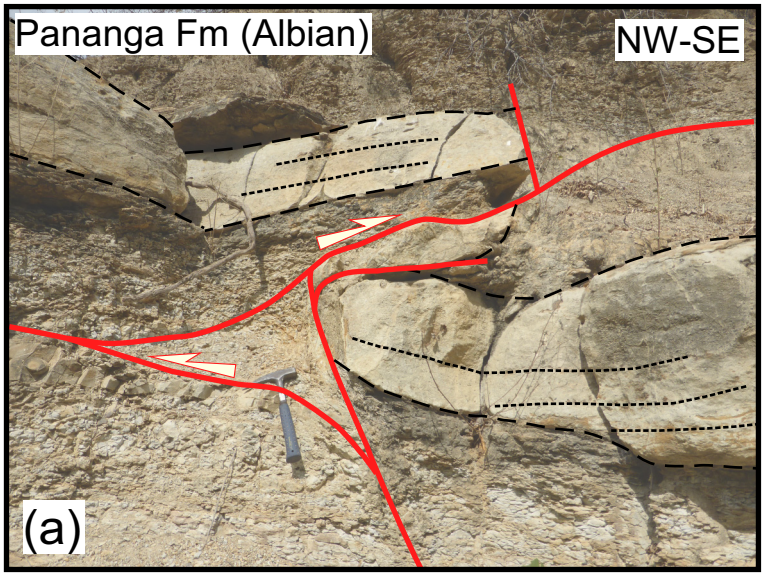
Pananga Fm (Albian)
NW-SE
(a)

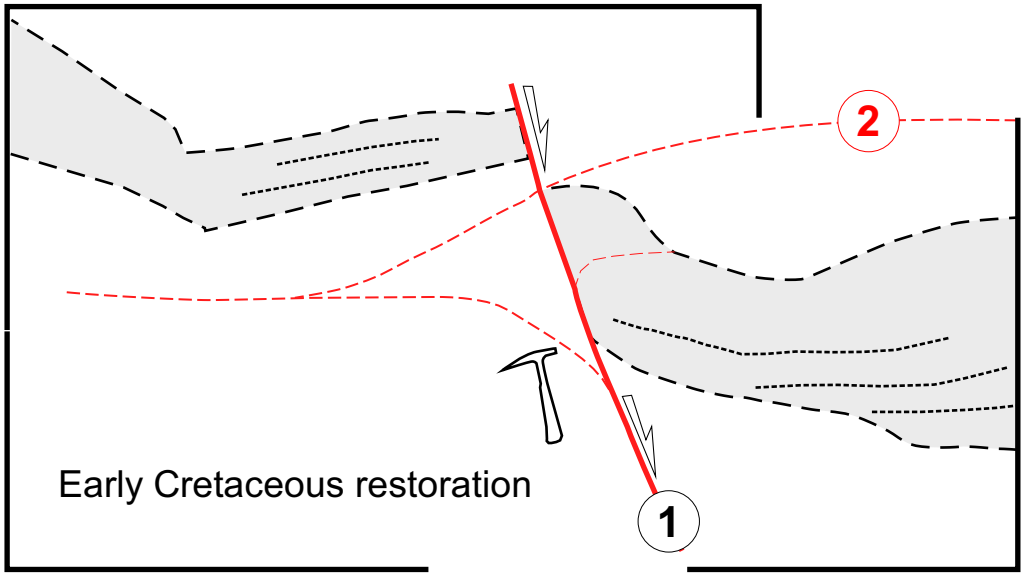
2
Early Cretaceous restoration
1

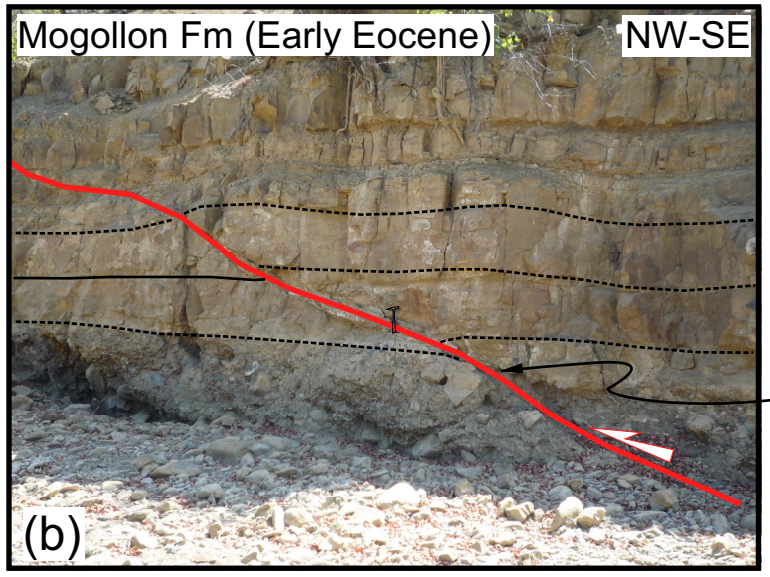
Mogollon Fm (Early Eocene)
NW-SE
(b)

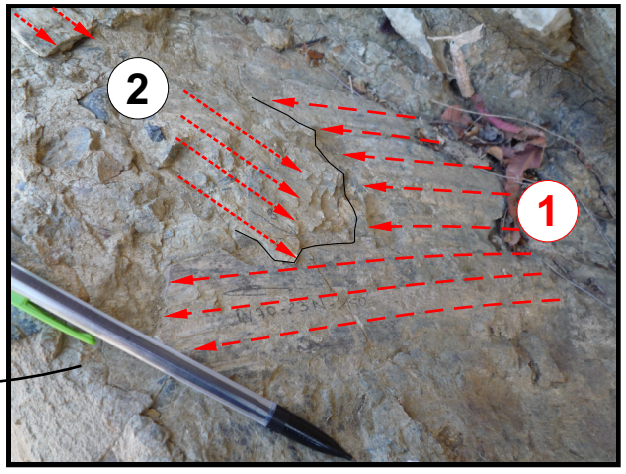
2
1

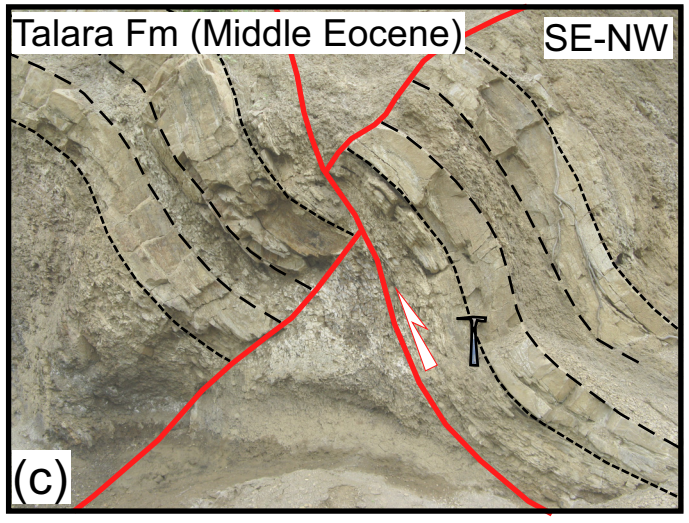
Talara Fm (Middle Eocene)
SE-NW
(c)

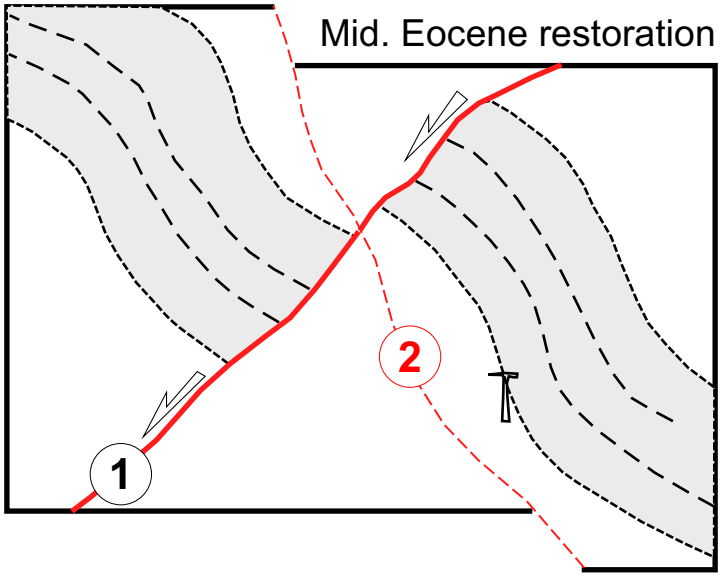
Mid. Eocene restoration
2
1

Figure 8.

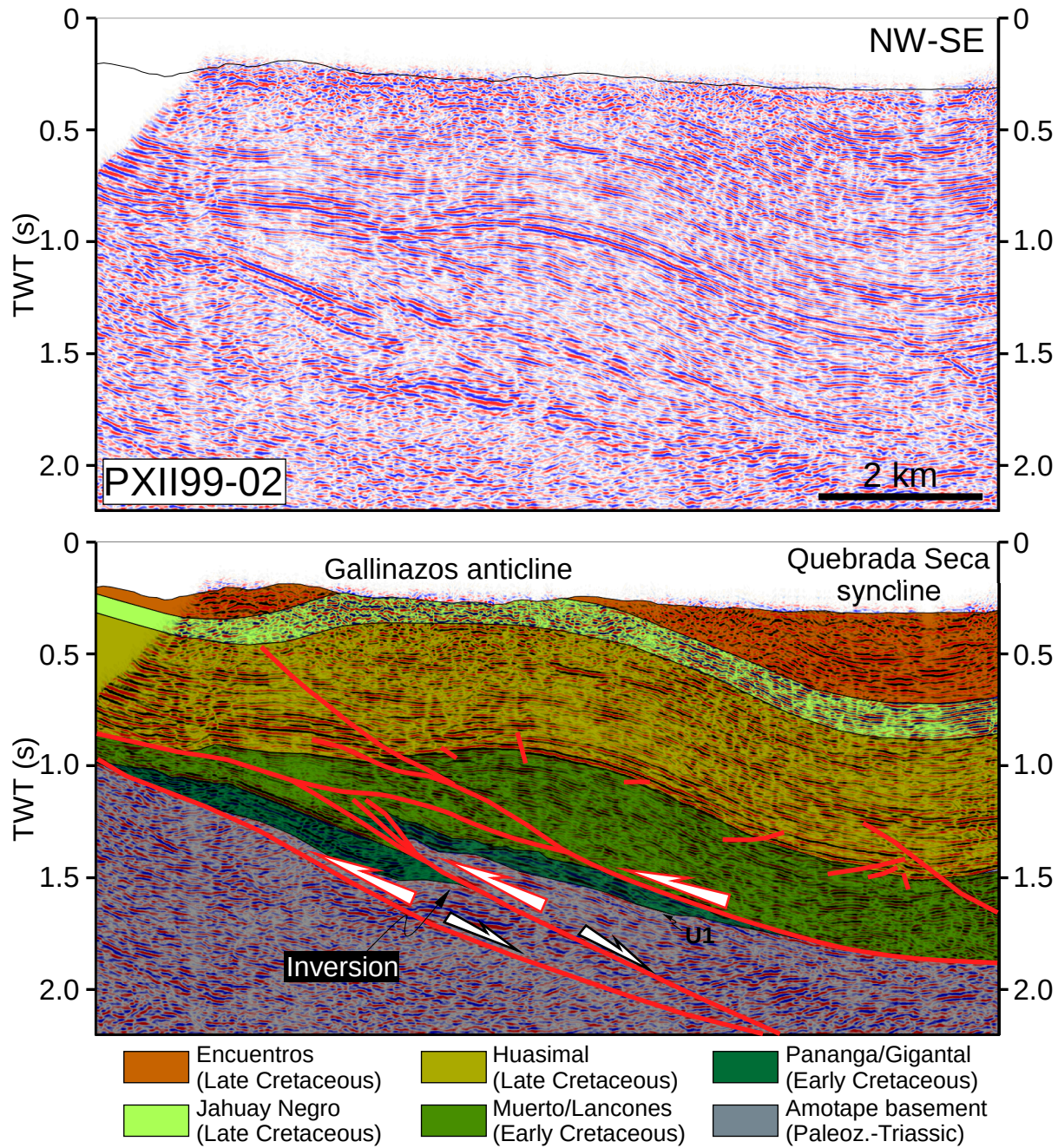
NW-SE
PXII99-02
2 km
TWT (s)
0
0.5
1.0
1.5
2.0
Gallinazos anticline
Quebrada Seca syncline
Inversion
U1
Encuentros (Late Cretaceous)
Huasimal (Late Cretaceous)
Pananga/Gigantal (Early Cretaceous)
Jahuay Negro (Late Cretaceous)
Muerto/Lancones (Early Cretaceous)
Amotape basement (Paleoz.-Triassic)

Figure 9.

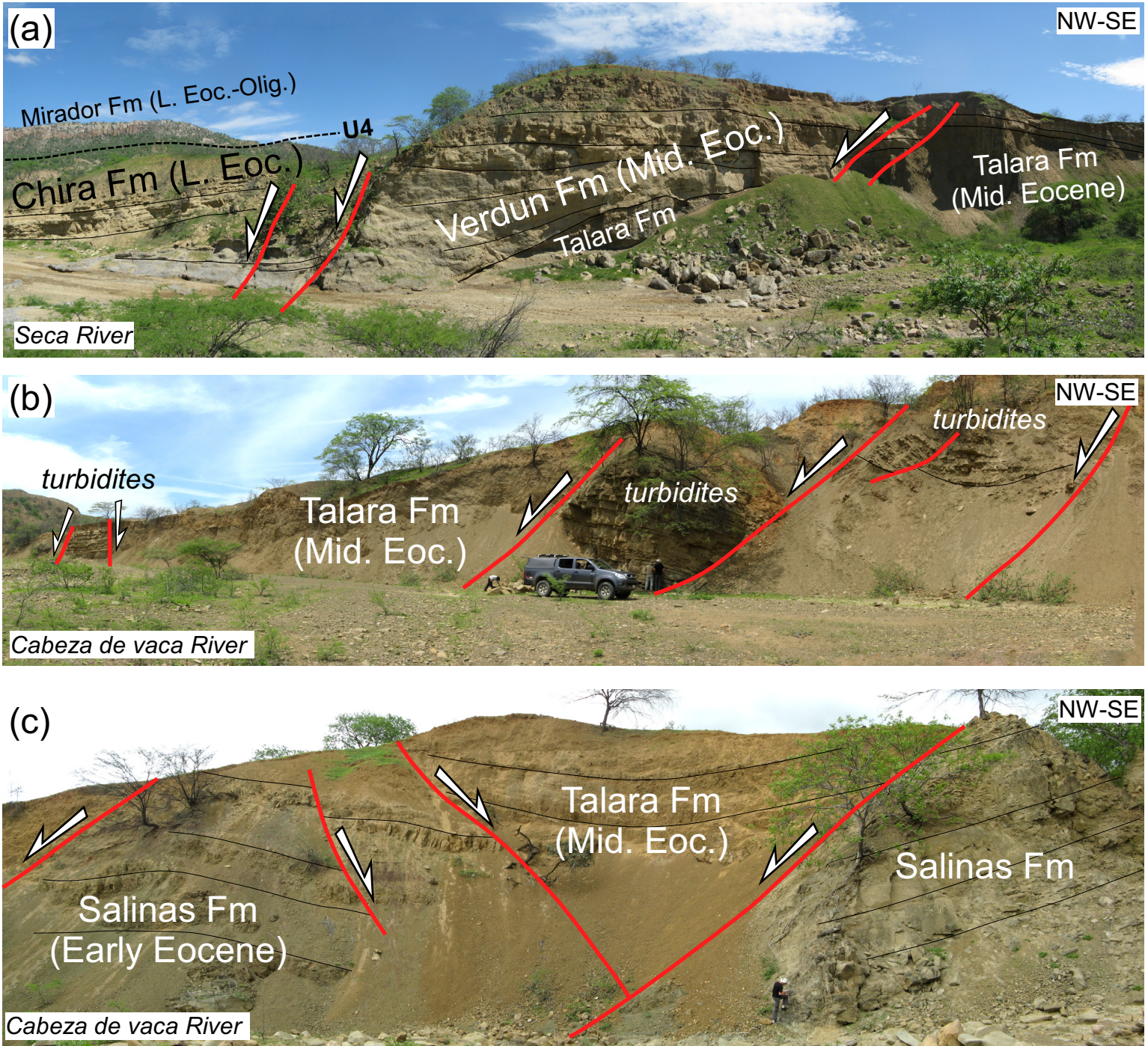
(a)
NW-SE
Mirador Fm (L. Eoc.-Olig.)
U4
Chira Fm (L. Eoc.)
Verdun Fm (Mid. Eoc.)
Talara Fm
Talara Fm
(Mid. Eocene)
Seca River
(b)
NW-SE
turbidites
turbidites
turbidites
Talara Fm
(Mid. Eoc.)
Cabeza de vaca River
(c)
NW-SE
Talara Fm
(Mid. Eoc.)
Salinas Fm
Salinas Fm
(Early Eocene)
Cabeza de vaca River

Figure 10.

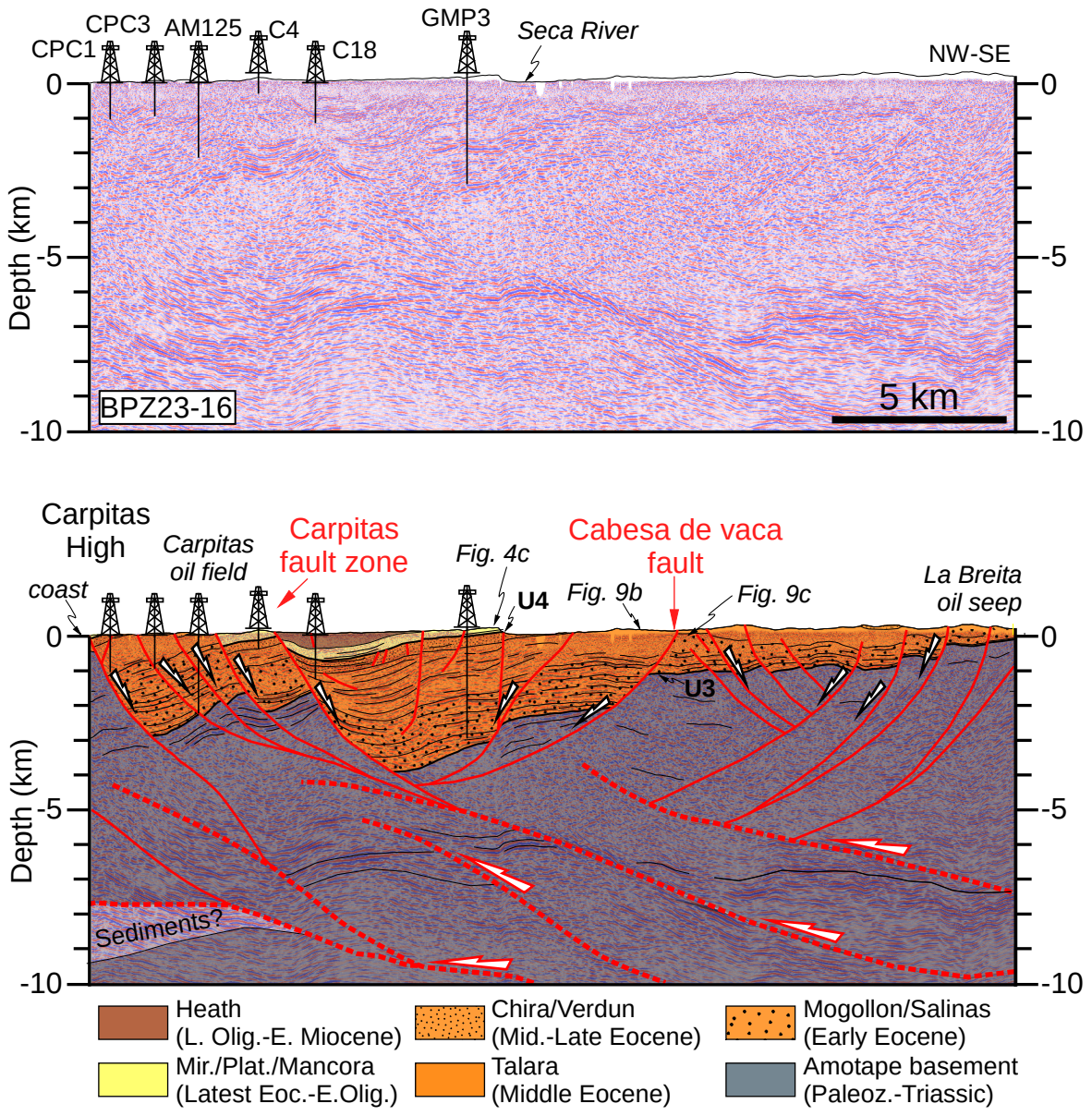
CPC1
CPC3
AM125
C4
C18
GMP3
Seca River
NW-SE
0
-5
-10
Depth (km)
BPZ23-16
5 km
Carpitas High
coast
Carpitas oil field
Carpitas fault zone
Fig. 4c
U4
Fig. 9b
Cabesa de vaca fault
Fig. 9c
La Breita oil seep
U3
Sediments?
Heath (L. Olig.-E. Miocene)
Chira/Verdun (Mid.-Late Eocene)
Mogollon/Salinas (Early Eocene)
Mir./Plat./Mancora (Latest Eoc.-E.Olig.)
Talara (Middle Eocene)
Amotape basement (Paleoz.-Triassic)

Figure 11.

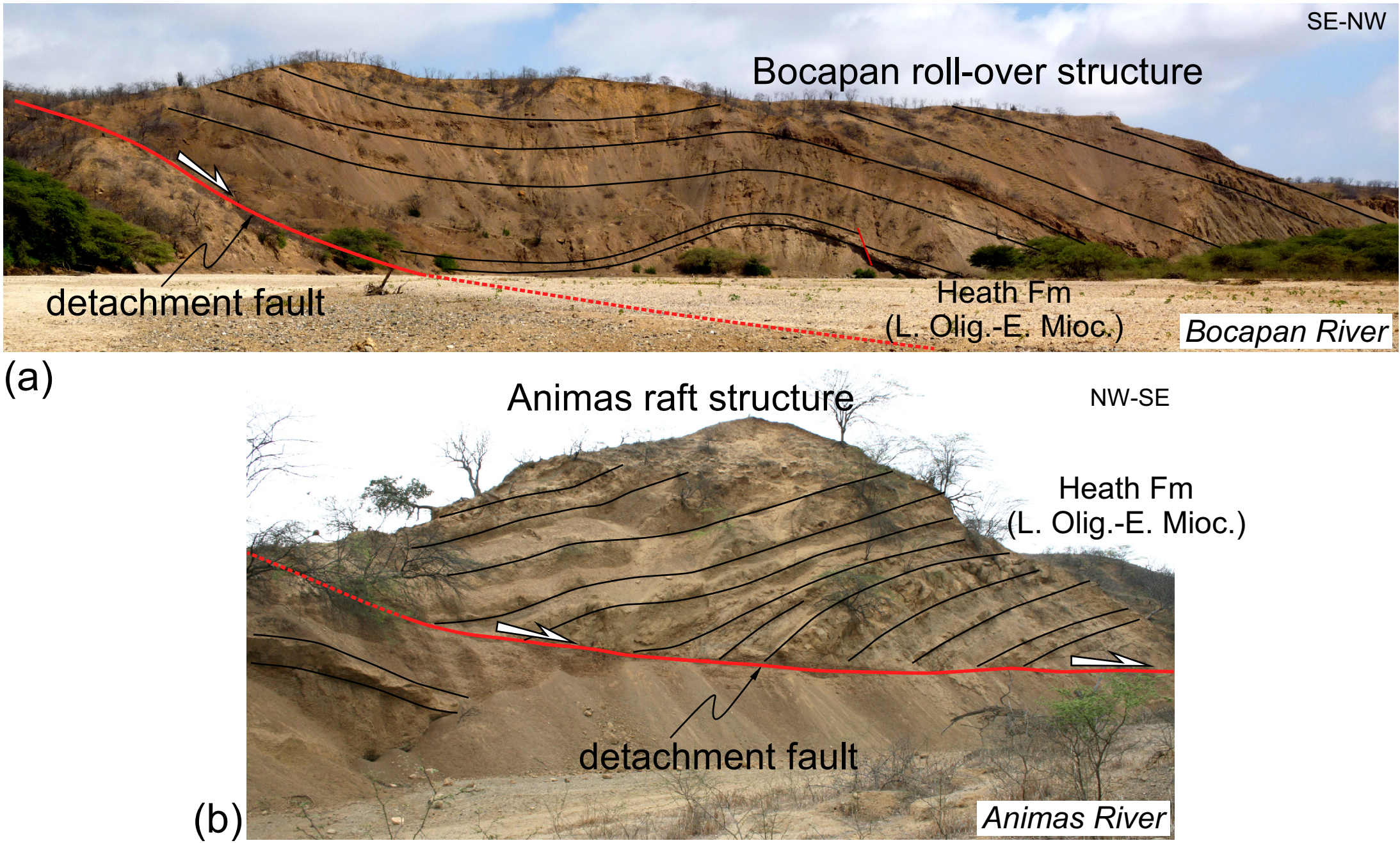
SE-NW
Bocapan roll-over structure
detachment fault
Heath Fm
(L. Olig.-E. Mioc.)
Bocapan River
(a)
Animas raft structure
NW-SE
Heath Fm
(L. Olig.-E. Mioc.)
detachment fault
Animas River
(b)

Figure 12.

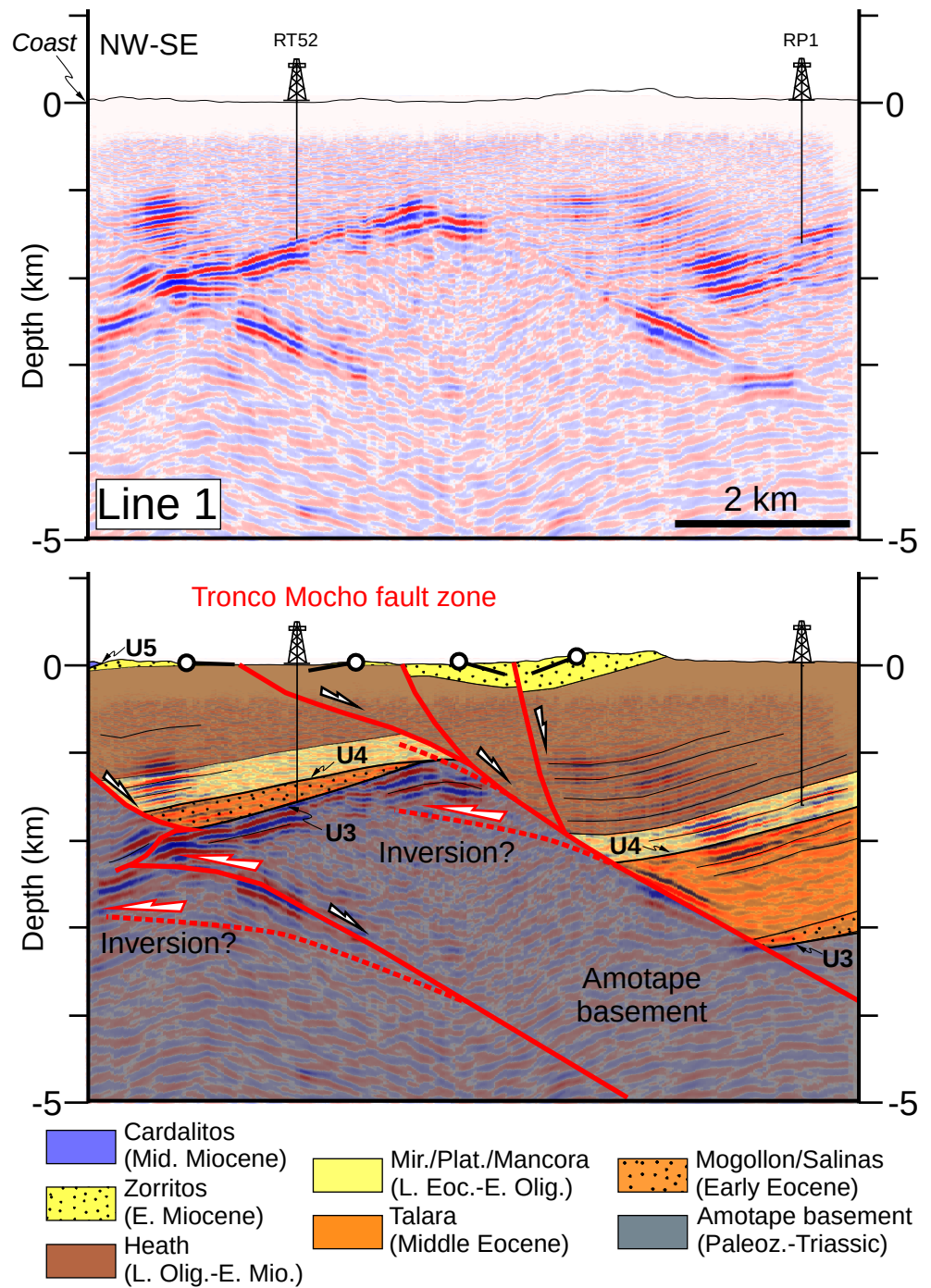
Coast
NW-SE
RT52
RP1
0
Depth (km)
-5
Line 1
2 km
Tronco Mocho fault zone
U5
U4
U3
Inversion?
Inversion?
U4
U3
Amotape
basement
Cardalitos
(Mid. Miocene)
Zorritos
(E. Miocene)
Heath
(L. Olig.-E. Mio.)
Mir./Plat./Mancora
(L. Eoc.-E. Olig.)
Talara
(Middle Eocene)
Mogollon/Salinas
(Early Eocene)
Amotape basement
(Paleoz.-Triassic)

Figure 13.

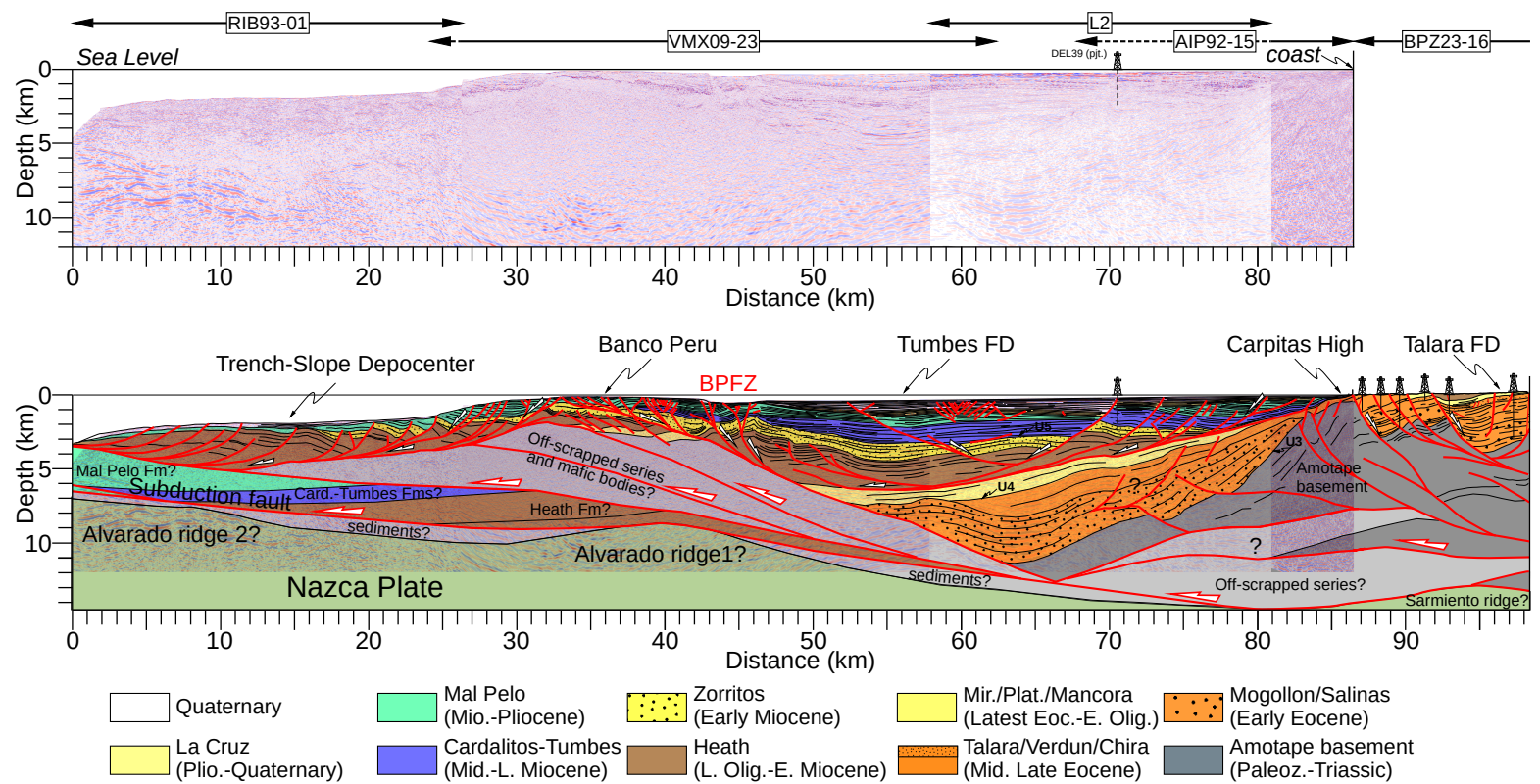
RIB93-01
VMX09-23
L2
AIP92-15
BPZ23-16
DEL39 (plt.)
Sea Level
coast
Depth (km)
Distance (km)
Trench-Slope Depocenter
Banco Peru
BPFZ
Tumbes FD
Carpitas High
Talara FD
Mal Pelo Fm?
Subduction fault
Card.-Tumbes Fms?
Heath Fm?
sediments?
Alvarado ridge 2?
Off-scrapped series and mafic bodies?
Alvarado ridge1?
Nazca Plate
U5
U4
U3
Amotape basement
Off-scrapped series?
Sarmiento ridge?
Quaternary
La Cruz (Plio.-Quaternary)
Mal Pelo (Mio.-Pliocene)
Cardalitos-Tumbes (Mid.-L. Miocene)
Zorritos (Early Miocene)
Heath (L. Olig.-E. Miocene)
Mir./Plat./Mancora (Latest Eoc.-E. Olig.)
Talara/Verdun/Chira (Mid. Late Eocene)
Mogollon/Salinas (Early Eocene)
Amotape basement (Paleoz.-Triassic)

Figure 14.

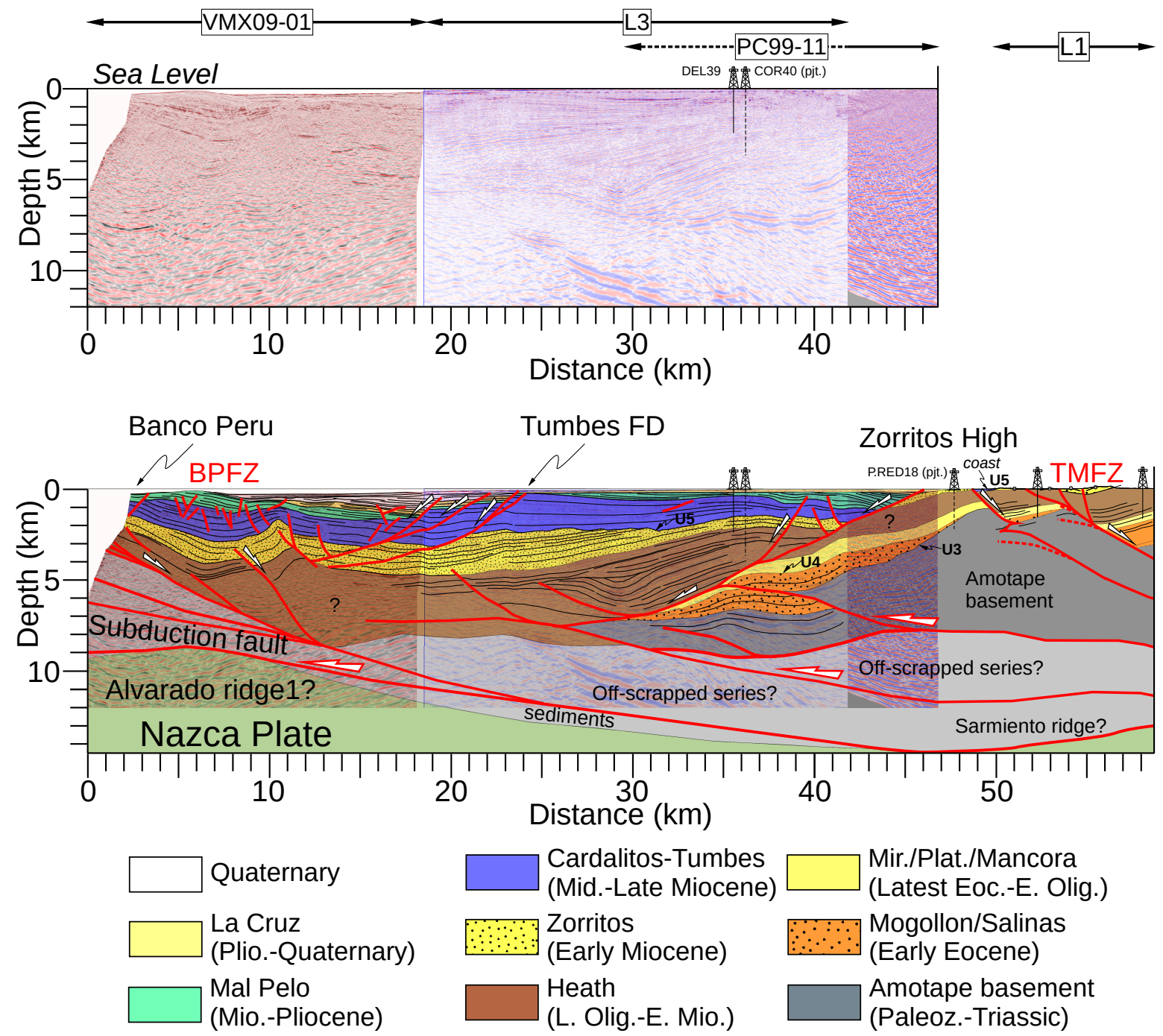
VMX09-01
L3
PC99-11
L1
Sea Level
DEL39
COR40 (pjt.)
Depth (km)
0
5
10
0
10
20
30
40
Distance (km)
Banco Peru
BPFZ
Tumbes FD
Zorritos High
P.RED18 (pjt.)
coast
U5
TMFZ
U5
U4
U3
?
?
Amotape
basement
Subduction fault
Alvarado ridge1?
Off-scrapped series?
Off-scrapped series?
sediments
Sarmiento ridge?
Nazca Plate
0
5
10
Depth (km)
0
10
20
30
40
50
Distance (km)
Quaternary
Cardalitos-Tumbes
(Mid.-Late Miocene)
Mir./Plat./Mancora
(Latest Eoc.-E. Olig.)
La Cruz
(Plio.-Quaternary)
Zorritos
(Early Miocene)
Mogollon/Salinas
(Early Eocene)
Mal Pelo
(Mio.-Pliocene)
Heath
(L. Olig.-E. Mio.)
Amotape basement
(Paleoz.-Triassic)

Figure 15.

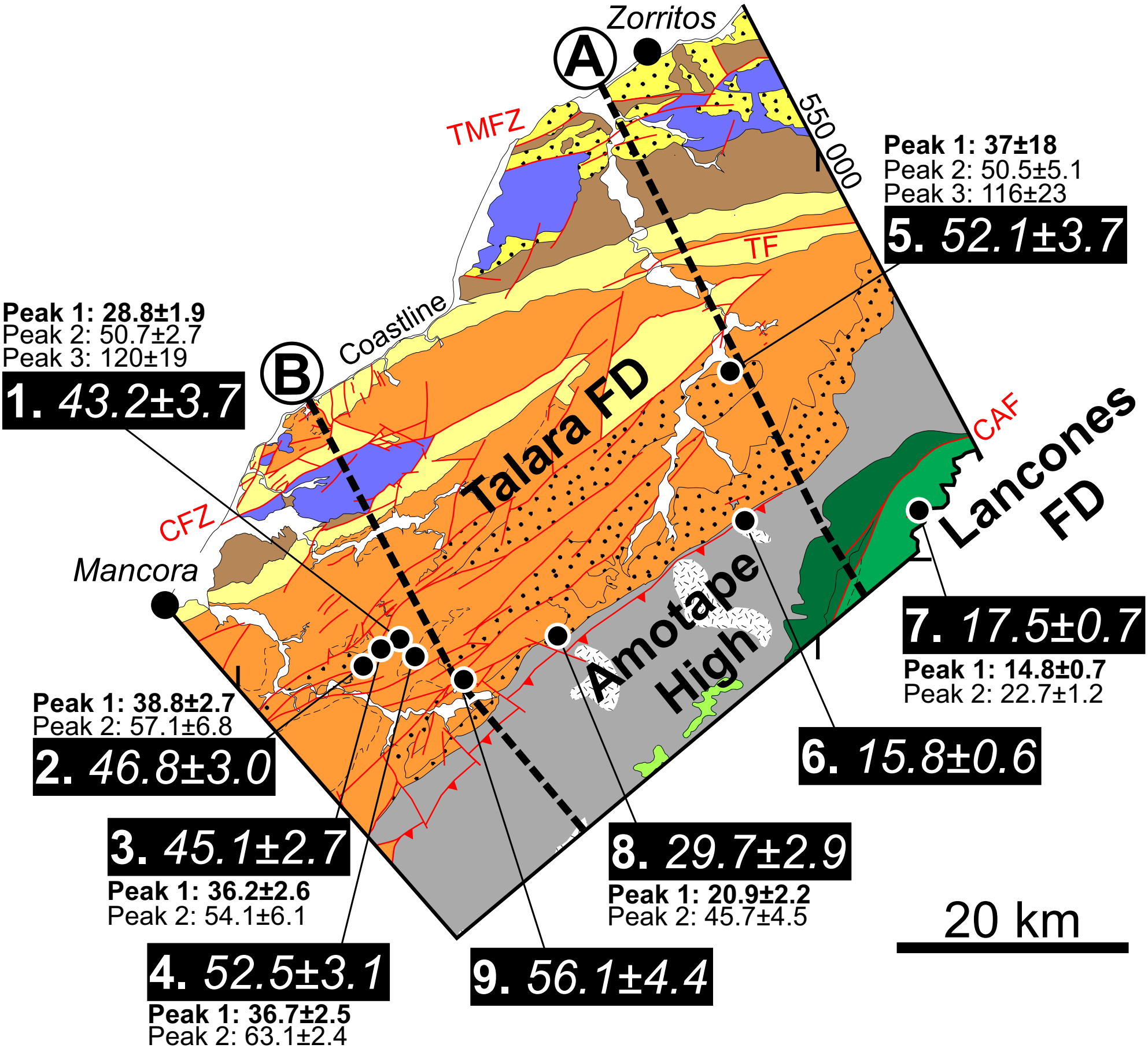
Zorritos
A
B
TMFZ
550 000
Coastline
TF
CFZ
CAF
Talara FD
Lancones FD
Amotape High
Mancora
Peak 1: 37±18
Peak 2: 50.5±5.1
Peak 3: 116±23
5. 52.1±3.7
Peak 1: 28.8±1.9
Peak 2: 50.7±2.7
Peak 3: 120±19
1. 43.2±3.7
7. 17.5±0.7
Peak 1: 14.8±0.7
Peak 2: 22.7±1.2
Peak 1: 38.8±2.7
Peak 2: 57.1±6.8
2. 46.8±3.0
6. 15.8±0.6
3. 45.1±2.7
Peak 1: 36.2±2.6
Peak 2: 54.1±6.1
8. 29.7±2.9
Peak 1: 20.9±2.2
Peak 2: 45.7±4.5
20 km
4. 52.5±3.1
Peak 1: 36.7±2.5
Peak 2: 63.1±2.4
9. 56.1±4.4

Figure 16.

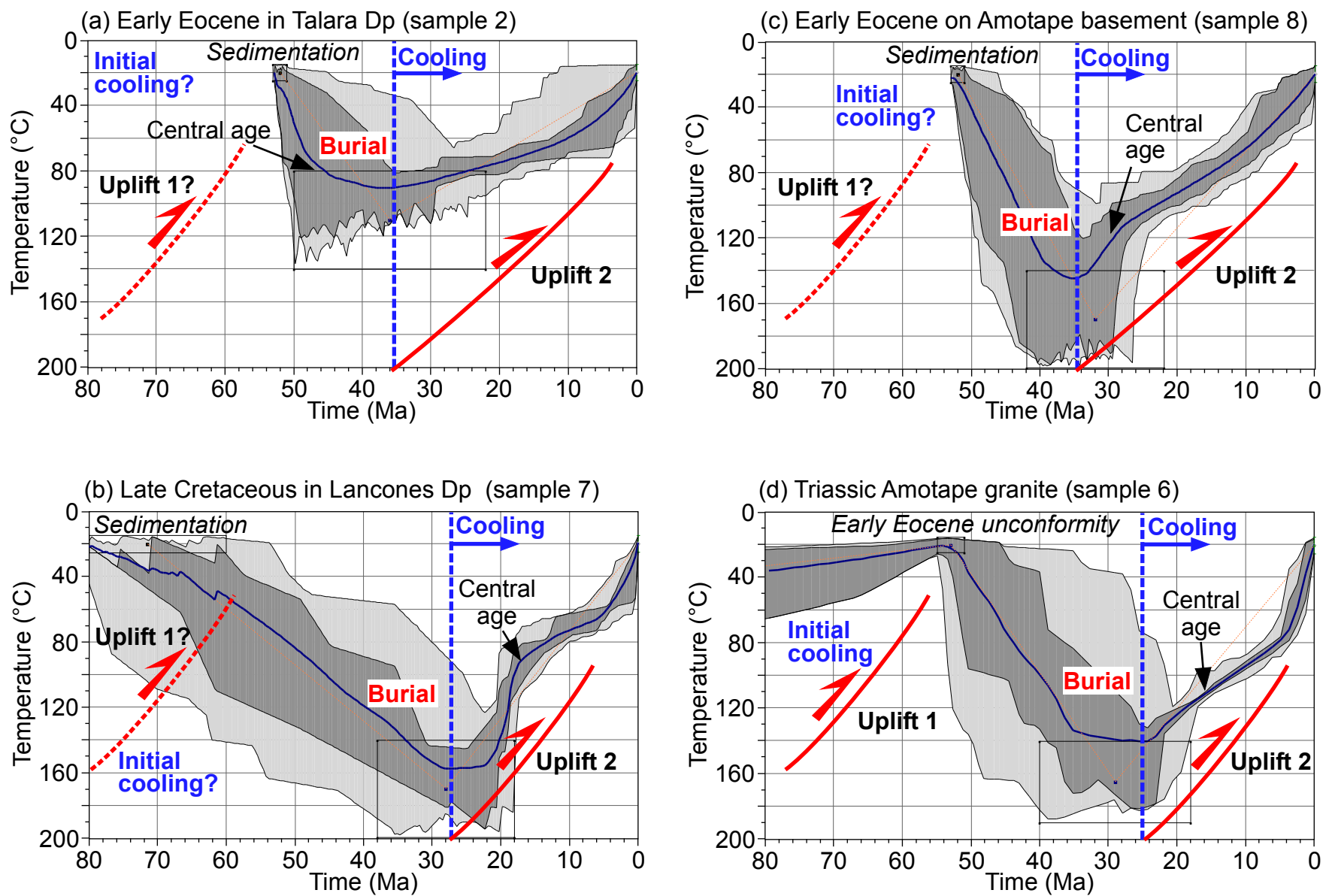
(a) Early Eocene in Talara Dp (sample 2)
Sedimentation
Cooling
Initial cooling?
Central age
Burial
Uplift 1?
Uplift 2
Temperature (°C)
Time (Ma)
(c) Early Eocene on Amotape basement (sample 8)
Sedimentation
Cooling
Initial cooling?
Central age
Uplift 1?
Burial
Uplift 2
Temperature (°C)
Time (Ma)
(b) Late Cretaceous in Lancones Dp (sample 7)
Sedimentation
Cooling
Central age
Uplift 1?
Burial
Initial cooling?
Uplift 2
Temperature (°C)
Time (Ma)
(d) Triassic Amotape granite (sample 6)
Early Eocene unconformity
Cooling
Central age
Initial cooling
Burial
Uplift 1
Uplift 2
Temperature (°C)
Time (Ma)

Figure 17.

(a) Cross section A

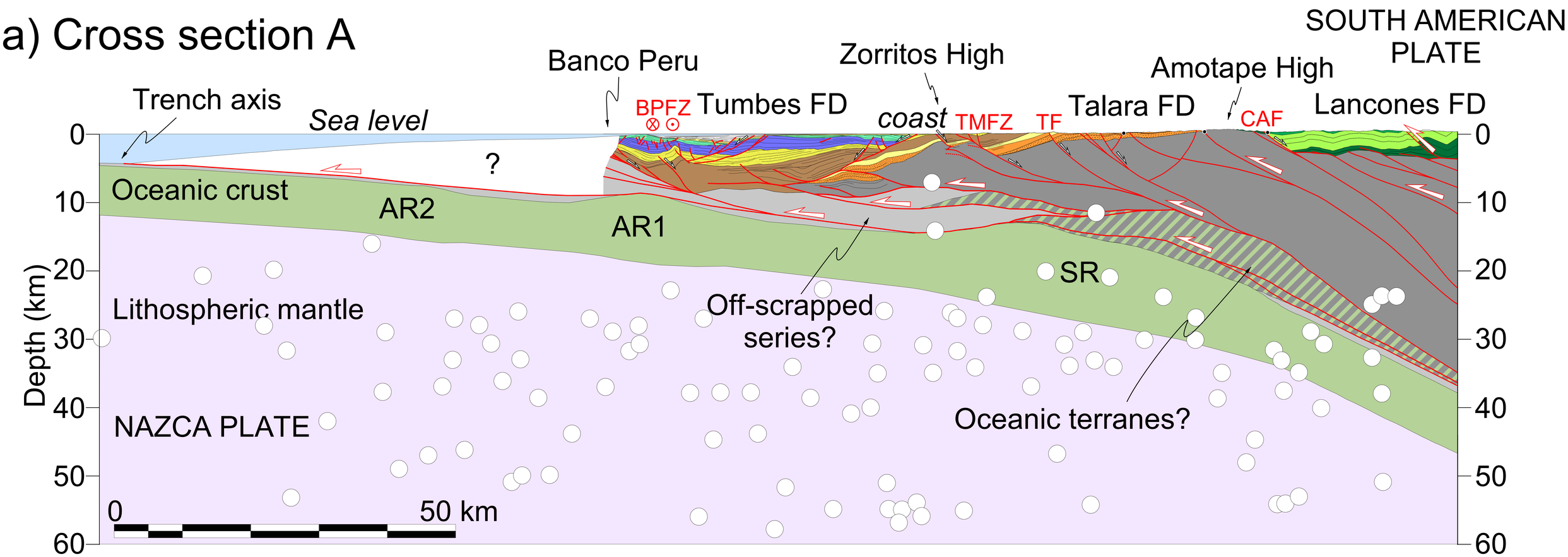

(b) Cross section B

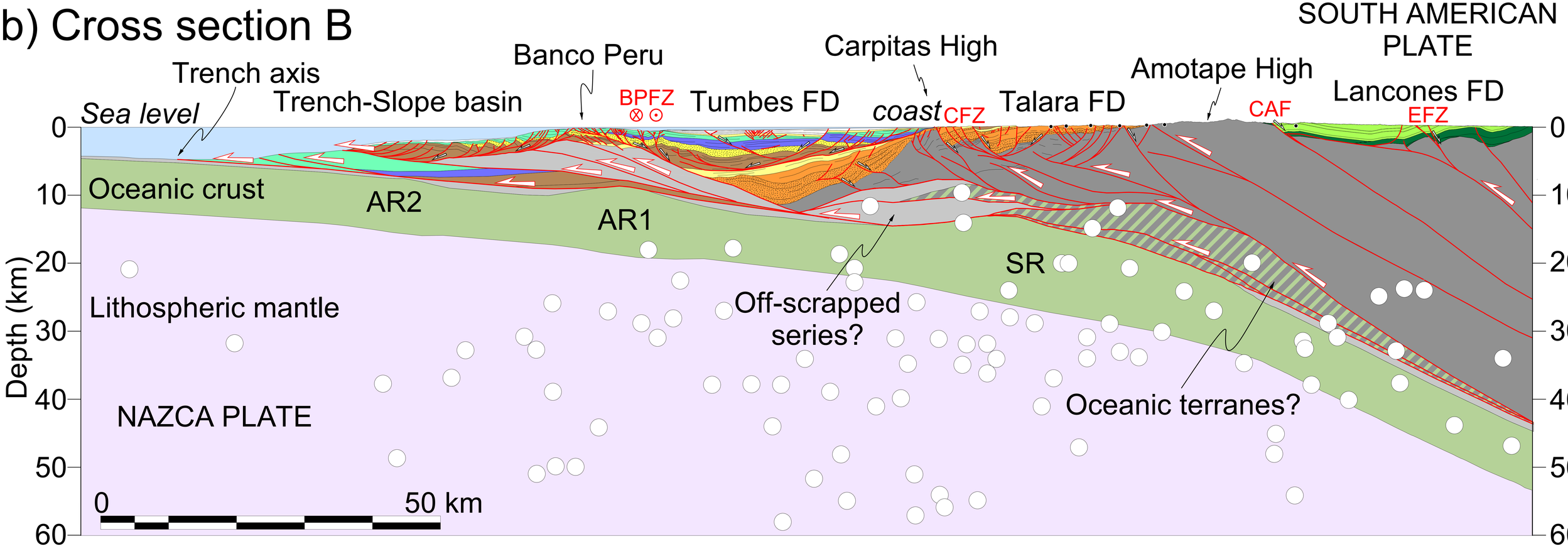

Quaternary
Mal Pelo (Mio.-Plio.)
Zorritos (Early Miocene)
Mir./Plat./Man. (L. Eoc.-E. Olig.)
Mog./Salinas (Early Eocene)
Muerto/Lancones/ Pananga/Gigantal (Early Cretaceous)
Undifferentiated oceanic series
La Cruz (Plio.-Quat.)
Cardalitos (M.-L. Mioc.)
Heath (L.Olig.-E. Mio.)
Tal./Verd./Chira (L.-Mid. Eocene)
Hua./J. Negro/Enc. (Late Cretaceous)
Amotape basement/ Granite (Paleoz.-Trias.)
Seismic events Mw>5

Figure 18.

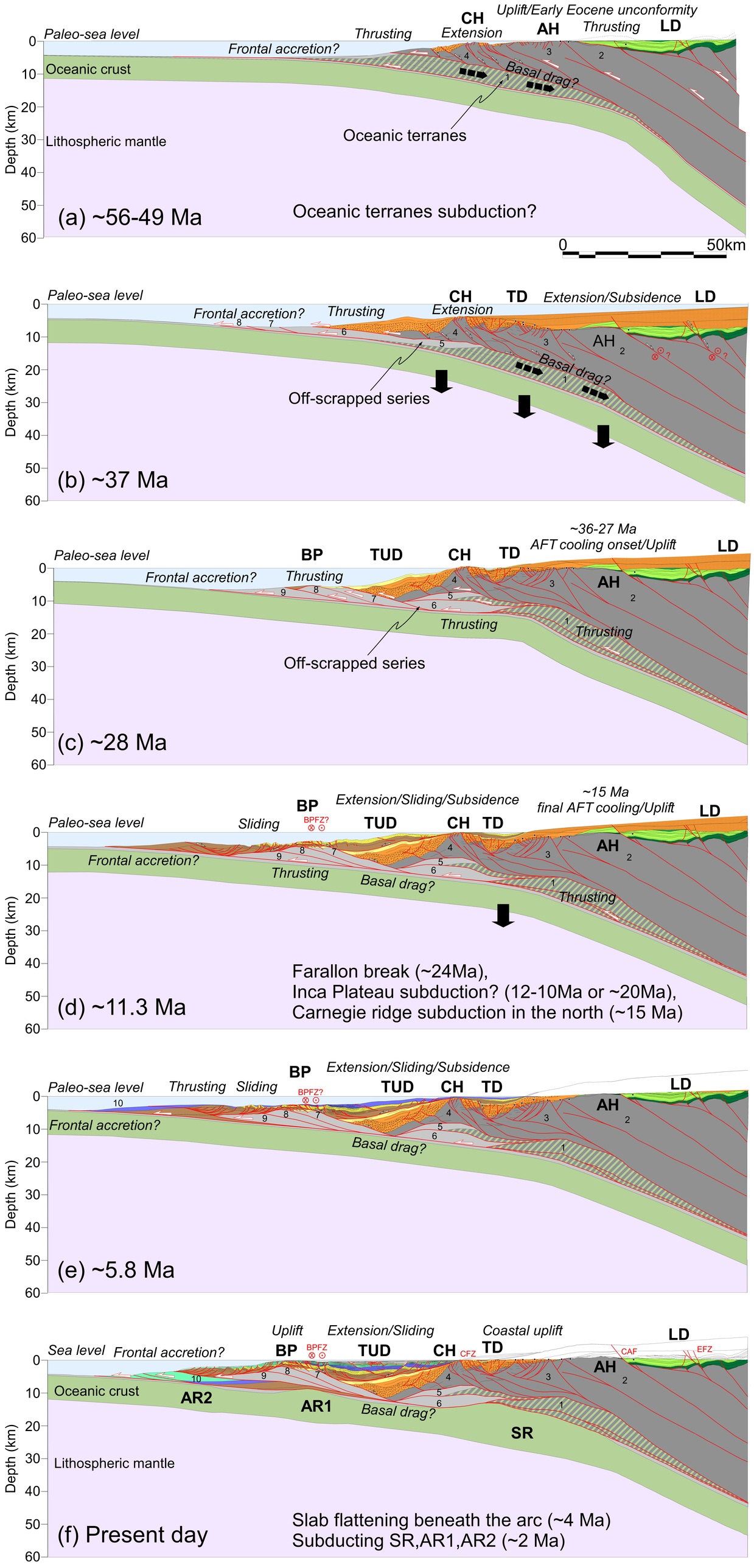
Uplift/Early Eocene unconformity
CH
AH
LD
Paleo-sea level
Thrusting
Extension
Thrusting
Frontal accretion?
Oceanic crust
Basal drag?
Lithospheric mantle
Oceanic terranes
Depth (km)
(a) ~56-49 Ma
Oceanic terranes subduction?
0
50km
Paleo-sea level
CH
TD
Extension/Subsidence
LD
Frontal accretion?
Thrusting
Extension
AH
Basal drag?
Off-scrapped series
(b) ~37 Ma
~36-27 Ma
AFT cooling onset/Uplift
Paleo-sea level
BP
TUD
CH
TD
LD
Frontal accretion?
Thrusting
AH
Thrusting
Thrusting
Off-scrapped series
(c) ~28 Ma
~15 Ma
final AFT cooling/Uplift
Extension/Sliding/Subsidence
BP
BPFZ?
Paleo-sea level
Sliding
TUD
CH
TD
LD
AH
Frontal accretion?
Thrusting
Basal drag?
Thrusting
Farallon break (~24Ma),
Inca Plateau subduction? (12-10Ma or ~20Ma),
Carnegie ridge subduction in the north (~15 Ma)
(d) ~11.3 Ma
Extension/Sliding/Subsidence
BP
Paleo-sea level
Thrusting
Sliding
BPFZ?
TUD
CH
TD
LD
AH
Frontal accretion?
Basal drag?
(e) ~5.8 Ma
Uplift
Extension/Sliding
Coastal uplift
LD
Sea level
Frontal accretion?
BP
BPFZ
TUD
CH
CFZ
TD
CAF
EFZ
AH
Oceanic crust
AR2
AR1
Basal drag?
SR
Lithospheric mantle
Slab flattening beneath the arc (~4 Ma)
Subducting SR,AR1,AR2 (~2 Ma)
(f) Present day

Figure 19.

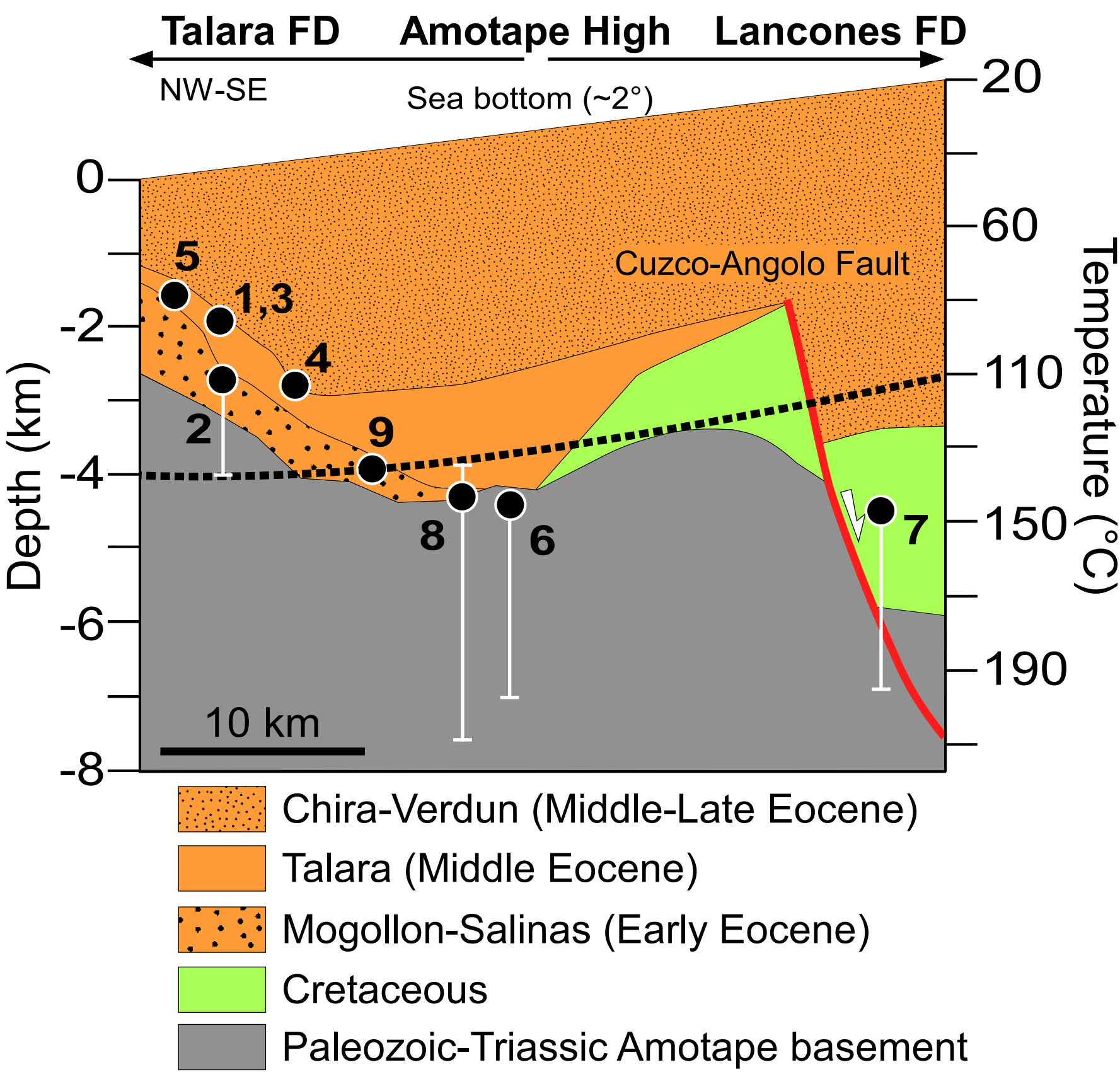
Talara FD
Amotape High
Lancones FD
NW-SE
Sea bottom (~2°)
Cuzco-Angolo Fault
5
1,3
4
2
9
8
6
7
10 km
Depth (km)
0
-2
-4
-6
-8
Temperature (°C)
20
60
110
150
190
Chira-Verdun (Middle-Late Eocene)
Talara (Middle Eocene)
Mogollon-Salinas (Early Eocene)
Cretaceous
Paleozoic-Triassic Amotape basement

Figure 20.

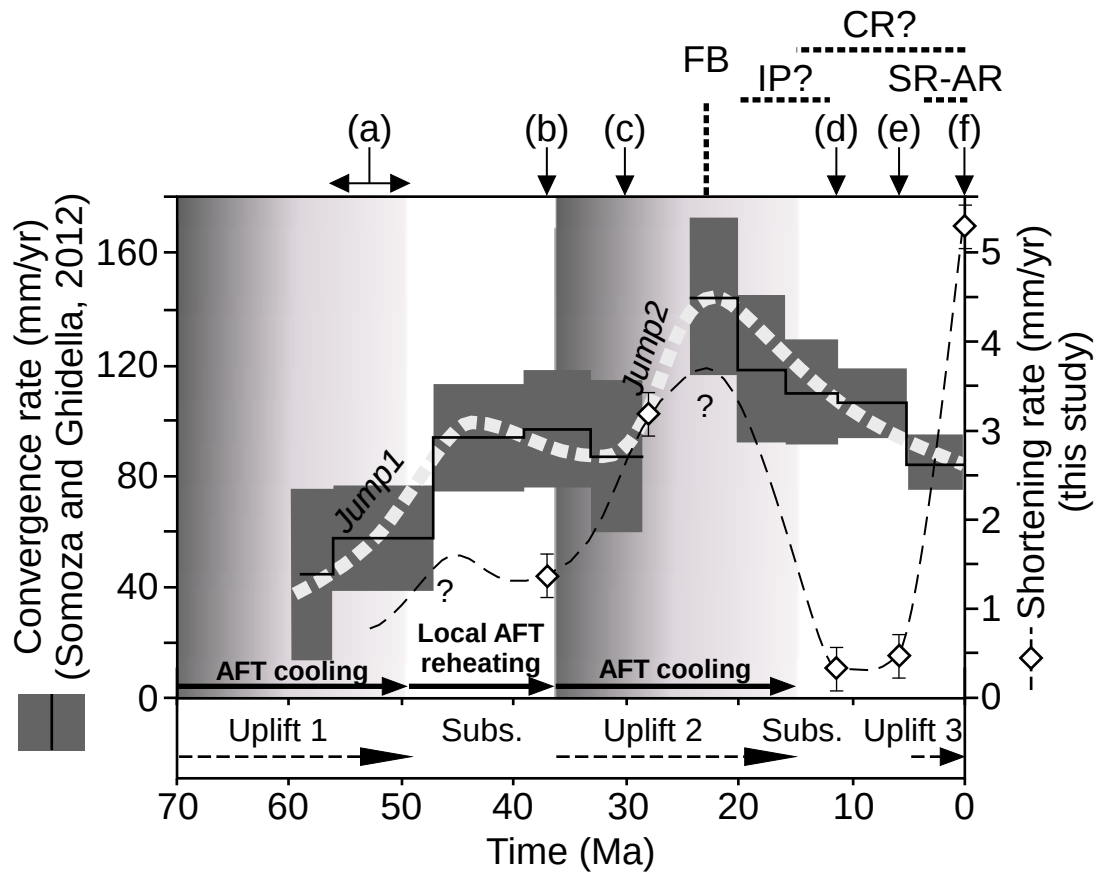
CR?
FB
IP?
SR-AR
(a)
(b)
(c)
(d)
(e)
(f)
Convergence rate (mm/yr)
(Somoza and Ghidella, 2012)
Shortening rate (mm/yr)
(this study)
Jump1
Jump2
?
?
Local AFT
reheating
AFT cooling
AFT cooling
Uplift 1
Subs.
Uplift 2
Subs.
Uplift 3
160
120
80
40
0
5
4
3
2
1
0
70
60
50
40
30
20
10
0
Time (Ma)